UNIVERSITY OF SOUTHAMPTON

Faculty of Engineering and Physical Sciences

School of Chemistry

Simulation of Lubricant Properties and their Interactions with Surfaces

by

Dimitrios Mathas

ORCID ID 0000-0003-0116-0156

Thesis for the degree of Doctor of Philosophy

November, 2022

UNIVERSITY OF SOUTHAMPTON

ABSTRACT

Faculty of Engineering and Physical Sciences

School of Chemistry

Doctor of Philosophy

Simulation of Lubricant Properties and their Interactions with Surfaces

by

Dimitrios Mathas

The behaviour of lubricants at operational conditions, such as at high temperatures and pressures, is a topic of great industrial interest. In particular, viscosity and the viscosity-pressure relation are especially important for applications and their determination by computational simulations is very desirable.

In this thesis we evaluate methods to compute these quantities based on fully atomistic molecular dynamics simulations which are computationally demanding but also have the potential to be most accurate. We tested several molecules that are used as lubricants, such as 9,10-dimethyloctadecane, main component of PAO-2 base oil, which was used as the main lubricant for our simulations. The methods used for the viscosity simulations are the Green-Kubo equilibrium molecular dynamics (EMD-GK), the direct computation of viscosity from shear during non-equilibrium MD (NEMD) and the use of confined NEMD, where the fluid is confined within explicitly defined iron oxide wall surfaces, at pressures of up to 1.0 GPa and various temperatures (40-150 degrees Celsius). We present the theory behind these methods and investigate how the simulation parameters affect the results obtained, to ensure viscosity convergence with respect to the simulation intervals and all other parameters. We show that by using each method in its regime of applicability, we can achieve good agreement between simulated and measured values. NEMD simulations at high pressures captured zero shear viscosity successfully, while at 40 degrees Celsius EMD-GK is only applicable to pressures up to 0.3 GPa, where the viscosity is lower. In NEMD, longer and multiply repeated simulations reduce the standard deviation of viscosity, which is essential at lower pressures.

Additionally, by using confined NEMD simulations, it was demonstrated that the film thickness of the fluid affects viscosity, and as we increase the number of lubricant molecules, we approach the viscosity value of the bulk fluid derived from NEMD simulations.

Another aspect of these methods is the choice of the utilised force field for the atomic interactions. This was investigated by selecting three different commonly used force fields. We have explored several methods for calculating viscosity and we obtained results of particular industrial interest.

Contents

List of Tables

List of Figures

Research Thesis: Declaration of Authorship

Print name: DIMITRIOS MATHAS

Title of thesis: Simulation of Lubricant Properties and their Interactions with Surfaces

I declare that this thesis and the work presented in it are my own and has been generated by me as the result of my own original research.
I confirm that:

1. This work was done wholly or mainly while in candidature for a research degree at this University;

2. Where any part of this thesis has previously been submitted for a degree or any other qualification at this University or any other institution, this has been clearly stated;

3. Where I have consulted the published work of others, this is always clearly attributed;

4. Where I have quoted from the work of others, the source is always given. With the exception of such quotations, this thesis is entirely my own work;

5. I have acknowledged all main sources of help;

6. Where the thesis is based on work done by myself jointly with others, I have made clear exactly what was done by others and what I have contributed myself;

7. Parts of this work have been published as:

    - Evaluation of Methods for Viscosity Simulations of Lubricants at Different Temperatures and Pressures: A Case Study on PAO-2. D. Mathas, W. Holweger, M. Wolf, C. Bohnert, V. Bakolas, J. Procelewska, L. Wang, S. Bair, and C.-K. Skylaris. *Tribol. Trans.* 64(6):1138–1148, 2021, doi: 10.1080/10402004.2021.1922790

Signature: Date: 02/11/2022

Acknowledgements

I would like to thank my academic supervisors, Professor Chris-Kriton Skylaris and Professor Ling Wang, who trusted me, and gave me the opportunity to expand my knowledge in the Computational Chemistry and Tribology field, while guiding me to develop scientific thinking that enables me to overcome research challenges.

Then, many thanks to my industrial supervisors, Professor Walter Holweger and Dr. Marcus Wolf from Schaeffler Technologies AG & Co. KG, for their support and suggestions throughout this work.

In addition, I would like to acknowledge the funding support of Schaeffler Technologies AG & Co. KG and an EPSRC Doctoral Training Centre Grant for my iPhD. studentship.

Finally, I would like to thank the Skylaris and nCATS research group, people from the NGCM CDT (especially Alex and Ed for useful discussions), Dr. James Ewen for useful discussions, my friends, Yang and my family for their support. This thesis is dedicated to my father.

Definitions and Abbreviations

ACF	Autocorrelation Function
AM1-BCC	Austin Model 1 - Bond Charge Corrections
CFD	Computational Fluid Dynamics
CPU	Central Processing Unit
CY	Carreau-Yasuda
DFT	Density Functional Theory
EMD-GK	Green-Kubo Equilibrium Molecular Dynamics
GAFF2-AA	General Amber Force Field 2 - All Atom
IK	Irving-Kirkwood
LAMMPS	Large-scale Atomic/Molecular Massively Parallel Simulator
L-OPLS-AA	Long Optimised Potential for Liquid Simulations - All Atom
MC	Monte Carlo
MD	Molecular Dynamics
MoDTP	Molybdenum Dithiophosphate
MPI	Message-Passing Interface
MTTK	Martyna-Tuckerman-Tobias-Klein
NEMD	Non-Equilibrium Molecular Dynamics
OPLS-AA	Optimised Potential for Liquid Simulations - All Atom
PAO	Polyalphaolefin
PEF	Planar Elongational Flow

PBCs	Periodic Boundary Conditions
PPPM	Particle-Particle Particle-Mesh
RMSE	Root Mean Square Error
RNEMD	Reverse Non-Equilibrium Molecular Dynamics
ZDDP	Zinc Dialkyldithiophosphate

Introduction

Lubricants are of great importance and extensively used in the industry, where there is a constant effort to increase the efficiency and lifetime of tribological systems, while combining the best possible material characteristics. Over the past thirty years, the interest in obtaining viscosity values from a simulation at various operational conditions (temperatures, pressures, shear rates) has risen sharply. This is due to the fact that computer simulations with the use of molecular dynamics and other methods can provide useful and valuable insights, in cases where measuring rheological properties can be difficult or not possible at all. There has been extensive work [1] for calculating key lubricant properties (density, viscosity) with molecular dynamics at ambient conditions, for various hydrocarbon lubricants, including linear and branched alkanes. Simulated and experimental values were very close in certain cases. Additionally, work has been done [2] on which model is most appropriate for lubricants by comparing classical force fields for molecular dynamics simulations. The results showed that the L-OPLS-AA (all-atom model for long hydrocarbons) gave better viscosity estimates, when equilibrium molecular dynamics was used for calculating the above-mentioned properties. The general tendency is that, at the cost of computation time, all-atom models, which describe each atom explicitly, perform significantly better than united atom models [3], where the nonpolar hydrogens are grouped with the carbon atoms to generate CH, CH_2 and CH_3 pseudo-atoms. Molecular dynamics simulations coupled with the pioneering Green-Kubo method [4, 5] appear to be efficient at low viscosity values and ambient conditions [6, 7]. This method uses internal equilibrium fluctuations, by evaluating integrals of autocorrelation functions, to describe transport properties such as zero shear (low shear) viscosity. However, some accuracy issues have been raised at high viscosities, and alternative methods such as non-equilibrium molecular dynamics (NEMD) [8, 9] or reverse non-equilibrium molecular dynamics (RNEMD) [10] have been proposed as the current state-of-the-art approaches. For more details, see this

comprehensive review article [3] which lists the chronological improvements of NEMD simulations.

Efforts have been made to improve the accuracy of the EMD-GK method. For example, one study [11] developed an on-the-fly implementation of the EMD-GK method for better estimation of transport coefficients such as viscosity and thermal conductivity. Another study [12] developed the time decomposition method, which minimises the uncertainty of the estimated shear viscosity by using multiple shorter EMD trajectories providing an improved approach for viscosity calculations. The EMD-GK method has been also used to calculate the viscosity of a quasi-2D dust [13] and quark gluon [14] plasma. Furthermore, it has been shown [15] that the Green-Kubo formula applies to quantum systems in a steady state, where the shear viscosity is expressed in terms of the symmetrised correlation function of its shear stress operator. Previous studies also include a variety of calculations for viscosity with EMD-GK combined with NEMD in most cases [16–19]. The systems in the literature include simple linear alkanes, cyclic [20] or long-chain hydrocarbons, and more complex structures such as squalane and 1-decene trimer (PAO-4) [21–23]. There are fewer research papers on viscosity index [24, 25] and pressure-viscosity coefficient calculations, a fact that may indicate that these properties can be difficult to simulate. At higher pressures, it becomes more difficult to capture the Newtonian regime, due to the decrease of the critical shear rate. To overcome this, studies have either employed viscosity-temperature models [26] to extrapolate zero shear viscosity at the designated pressure or, more recently [27–29], viscosity has been acquired through zero shear rate extrapolation schemes, such as Eyring theory. NEMD was applied in all cases, while it is also possible to acquire the viscosity-pressure relation from empirical models using MD-predicted material properties [30], such as pressure-volume data. NEMD has been also applied to more complicated surfaces for the description of friction in such systems [31].

Polyalphaolefins (PAOs) consist of branched, acyclic synthetic alkanes, which are used

in a variety of applications such as transmission fluids, gear, engine and hydraulic oils and in greases [32,33]. Some of their key properties include high viscosity indices, good thermal stability and low toxicity [34]. The kinematic viscosity at 100 °C is used as notation for each PAO grade. As a result, PAO-2 has a kinematic viscosity of about 2 mm^2/s (cSt) at 100 °C and consists mainly of hydrogenated 1-decene dimer isomers ($C_{20}H_{42}$), from which, 9,10-dimethyloctadecane is the most abundant [35] and is chosen for this theoretical study. For comparison with experiment, the PAO-2 sample that was used in this study contained more than 95% of hydrogenated 1-decene dimer by weight [36].

As there are relatively few studies examining the high pressure rheology of lubricants from a computational point of view, in this study, we examine the very interesting behaviour of a lubricant through molecular simulation approaches. We perform EMD-GK, bulk and confined NEMD simulations of viscosity with parameters such as temperature, pressure and shear rates that have values that can be encountered under operational conditions. This work aims to showcase the significance of the choice of method for calculating viscosity, by comparing available simulation approaches in order to find which works best when comparing to experimental data. The simulations are performed at different temperatures and pressures (up to 1.0 GPa), while investigating the shear rate dependence of viscosity. We have compared our simulation results with available experimental data of shear viscosity for each condition that was tested.

Our work aims to develop robust computational models in order to simulate various rheological properties of well-known lubricants, such as *n*-hexadecane, glycerol and 9,10-dimethyloctadecane, which are shown in Figure 1.

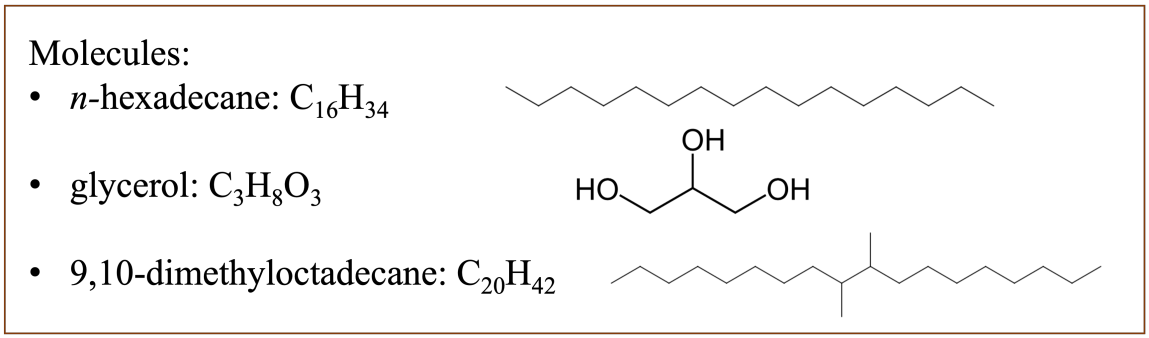

FIGURE 1: Molecules studied in this work. All of the selected molecules have wide industrial applications and their in-depth characterisation at operational conditions is highly desirable.

THESIS OUTLINE

In Chapter 1 we introduce the basic theory of molecular dynamics and describe the schemes involved in molecular simulations that are used to obtain robust results. These techniques, coupled with microscopic models of defining zero shear viscosity, are implemented in molecular simulation and the theoretical background is mentioned in Chapter 2. A key property that can be simulated with this kind of approaches, the calculation of zero shear viscosity through equilibrium molecular dynamics, is the subject of Chapter 3. Moreover, two alternative methods are presented in Chapter 4 and 5, respectively. One is the non-equilibrium molecular dynamics method through bulk liquids, while the other one includes a surface, where the liquid is confined within. Additionally, Appendices include information about programs that were used in this work, in-house codes that were developed to facilitate the calculation of viscosity and examples of simulation scripts.

Chapter 1

Theoretical background of atomistic simulations

1.1 Basic theory of molecular dynamics

The process of a molecular dynamics simulation is the evaluation of particle motion, given an inter-atomic potential. The potential energy $U(\mathbf{r})$ is linked to the time-varying force $\mathbf{F}_i(t)$, which can be integrated to give the velocity and the positions, according to Newton's second law of motion:

$$\mathbf{F}_i(t) = m_i \ddot{\mathbf{r}}_i(t) = -\frac{\partial U(\mathbf{r}^K)}{\partial \mathbf{r}_i} \tag{1.1}$$

Here, m_i is mass, $\mathbf{r}^K$ are the positions of K particles that define the potential and $\mathbf{r}_i$ is the position of each particle. Theoretically, the inter-atomic force must be calculated from the interactions of all other atoms. Unfortunately, this is very time consuming and thus a cut-off distance is employed. This distance limits the interactions to be only between the nearest neighboring atoms in the force evaluation.

In molecular dynamics, the instantaneous temperature of a system is given by:

$$T(t) = \sum_{i=1}^{K} \frac{m_i u_i^2(t)}{3K k_{\mathrm{B}}} \tag{1.2}$$

where m_i is mass of a particle, K in total, with u_i velocities and k_B is the Boltzmann constant.

1.1.1 Integration schemes

In molecular dynamics simulations, numerical integration is used to calculate the evolution of a system, given a timestep δt. The most popular integrators are the Verlet algorithm, the velocity Verlet algorithm, the Leapfrog algorithm, the predictor-corrector method and others. The velocity Verlet algorithm is superior to the Verlet algorithm due to the fact that the velocity Verlet algorithm calculates velocities at the same timesteps as positions, while the Verlet algorithm approximates the velocity. This can cause inconsistency in the calculation of temperature (eq. 1.2) and thermostating. The integration equations for the positions $\mathbf{r}$ and velocities $\mathbf{u}$ are [37] ($\boldsymbol{a}$ is acceleration):

Verlet algorithm:

$$\mathbf{r}(t+\delta t) = 2\mathbf{r}(t) - \mathbf{r}(t-\delta t) + \boldsymbol{a}(t)\delta t^2 \tag{1.3}$$

$$\mathbf{u}(t) = \frac{\mathbf{r}(t+\delta t) - \mathbf{r}(t-\delta t)}{2\delta t} \tag{1.4}$$

Velocity Verlet algorithm:

$$\mathbf{r}(t+\delta t) = \mathbf{r}(t) + \mathbf{u}(t)\delta t + \frac{1}{2}\boldsymbol{a}(t)\delta t^2 \tag{1.5}$$

$$\mathbf{u}(t+\delta t) = \mathbf{u}(t) + \frac{1}{2}[\boldsymbol{a}(t) + \boldsymbol{a}(t+\delta t)]\delta t \tag{1.6}$$

Leapfrog algorithm:

$$\mathbf{r}(t+\delta t) = \mathbf{r}(t) + \mathbf{u}(t+\frac{1}{2}\delta t)\delta t \tag{1.7}$$

$$\mathbf{u}(t+\frac{1}{2}\delta t) = \mathbf{u}(t-\frac{1}{2}\delta t) + \boldsymbol{a}(t) \tag{1.8}$$

1.1.2 The potential energy function

Another very important aspect in molecular dynamics is the potential energy function $U(\mathbf{r}^K)$ which can be expressed as:

$$U(\mathbf{r}^K) = U_{\text{bond}} + U_{\text{angle}} + U_{\text{dihedral}} + U_{\text{nonbond}} \tag{1.9}$$

where U_{bond} describes the harmonic vibrational motion between bonded atoms with respect to the equilibrium bond length, U_{angle} describes the angular vibrational motion of three atoms with respect to the equilibrium bond angle, U_{dihedral} refers to torsional rotation of four atoms with respect to a central bond and U_{nonbond} refers to non-bonded energy terms (Lenard-Jones and electrostatics). Their analytical expressions are:

$$U_{\text{bond}} = \sum_{bonds} k_i^{bond}(r_i - r_0)^2 \tag{1.10}$$

$$U_{\text{angle}} = \sum_{angles} k_i^{angle}(\theta_i - \theta_0)^2 \tag{1.11}$$

$$U_{\text{dihedral}} = \sum_{dihedrals} k_i^{dihe}[1 + \cos(n_i\phi_i - \delta_i)] \tag{1.12}$$

$$U_{\text{nonbond}} = \sum_{i<j} 4\varepsilon_{ij}\left[\left(\frac{\sigma_{ij}}{r_{ij}}\right)^{12} - \left(\frac{\sigma_{ij}}{r_{ij}}\right)^{6}\right] + \sum_{i<j}\frac{q_i q_j}{4\pi D r_{ij}} \tag{1.13}$$

where k_i^{bond}, k_i^{angle}, k_i^{dihe}, r_0, θ_0, n_i, δ_i, ε_{ij}, σ_{ij}, q_i and q_j are constants that depend on the molecular system examined and the chosen force field. The selection of appropriate values for these parameters is of great importance, in order to describe molecular interactions, and the development of force fields is an established research field. Specifically:

- k_i^{bond} is the bond stretching force constant
- k_i^{angle} is the bond angle bending force constant

- k_i^{dihe} is the dihedral force constant
- r_0 is the equilibrium bond distance
- θ_0 is the equilibrium bond angle
- n_i is the multiplicity of the function
- δ_i is the phase shift
- r_i is the interatomic distance
- θ_i is the angle between three atoms
- ϕ_i is the dihedral angle between four atoms
- ε_{ij} is the potential wall depth
- σ_{ij} is the collision diameter (the distance of two particles where the energy is zero)
- r_{ij} is the distance between two particles
- q_i and q_j are partial atomic charges
- D is the dielectric constant

In addition, in order to calculate pairwise interactions between different atoms, one possible mixing rule, the geometric rule [38], states that:

$$\varepsilon_{ij} = \sqrt{\varepsilon_i \varepsilon_j} \tag{1.14}$$

and

$$\sigma_{ij} = \sqrt{\sigma_i \sigma_j} \tag{1.15}$$

where ε_i and ε_j are the potential wall depths of atom i and j that have a collision diameter σ_i and σ_j.

1.1.3 Force fields

Force fields describe the interactions between atoms and their optimisation enhances the information that can be obtained from molecular dynamics simulations. The energy calculation depends on the used force field as shown in Figure 1.1 which summarises a simplified algorithm for performing molecular dynamics simulations.

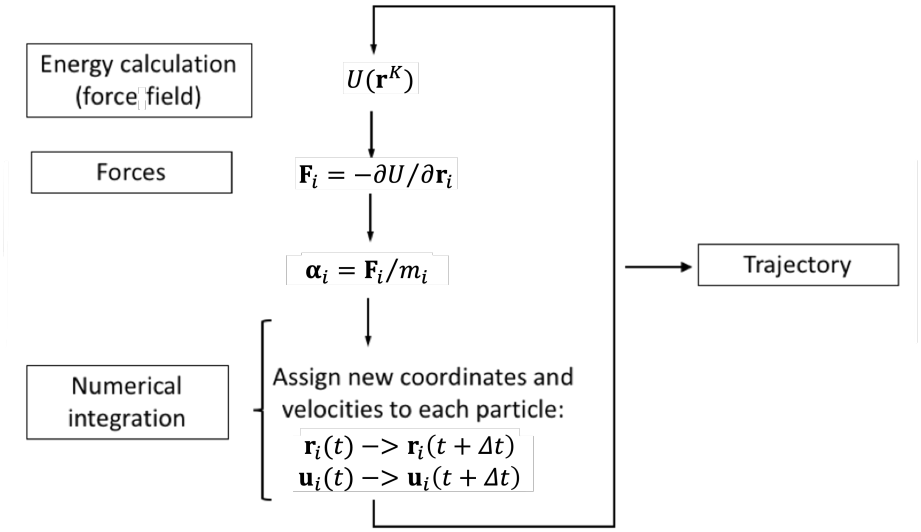

FIGURE 1.1: Molecular dynamics algorithm. The potential energy function is used to evaluate the forces which lead to the acceleration. At each timestep, the integrator updates the velocities and positions accordingly.

Among the most important force fields for liquid simulations, the OPLS-AA force field [38], an all-atom force field that treats each atom explicitly, includes values for the above-mentioned force field parameters in 1.1.2. A further improvement of torsional and non-bonded parameters for long hydrocarbons, led to the creation of the L-OPLS-AA force field [39]. In these force fields, U_{dihedral} is specified as:

$$U_{\text{dihedral}} = \frac{1}{2}K_1[1+\cos(\phi)] + \frac{1}{2}K_2[1-\cos(2\phi)] + \frac{1}{2}K_3[1+\cos(3\phi)] + \frac{1}{2}K_4[1-\cos(4\phi)] \tag{1.16}$$

Where, K_1, K_2, K_3, K_4 are the dihedral force constants equal to $2k_i^{dihe}$ and ϕ is the dihedral angle between four atoms.

Additionally, another commonly used force field, the GAFF2-AA [40], is a general purpose all-atom force field that includes parameters for almost all the organic molecules made of C, N, O, H, S, P, F, Cl, Br and I. As a complete force field, GAFF2-AA is suitable for studying a great number of molecules and has found use for pharmaceutical relevant molecules [41]. For the GAFF2-AA force field, U_{dihedral} is specified as:

$$U_{\text{dihedral}} = \sum_{i=1}^{m} k_i^{dihe}[1 + \cos(n_i\phi_i - \delta_i)] \tag{1.17}$$

where k_i^{dihe} is the dihedral force constant (m in total), n_i is the multiplicity of the function and δ_i is the phase shift.

Another very popular force field, the ReaxFF force field [42], employs a bond-order formalism in conjunction with polarisable charge descriptions to describe both reactive and non-reactive interactions between atoms. This allows ReaxFF to accurately model both covalent and electrostatic interactions for a diverse range of materials. As a result, the ReaxFF force field can be used to study chemical reactions, as bonds can form and break during a simulation, something that is not possible to happen in bonded force fields, for example, during simulations with L-OPLS-AA. The energy contributions to the ReaxFF potential are the following [42]:

$$U_{\text{system}} = U_{\text{bond}} + U_{\text{over}} + U_{\text{angle}} + U_{\text{tors}} + U_{\text{vdWaals}} + U_{\text{Coulomb}} + U_{\text{Specific}} \tag{1.18}$$

where U_{bond} is a continuous function of interatomic distance describing the energy associated with forming bonds between atoms. U_{angle} and U_{tors} are the energies associated with three-body angle strain and four-body torsional angle strain. U_{over} is an energy penalty that prevents the over coordination of atoms and is based on atomic valence rules. U_{Coulomb} and U_{vdWaals} represent the electrostatic and dispersive contributions calculated between

all atoms, regardless of connectivity and bond-order. U_{Specific} represents system specific terms that are not generally included, unless required to capture properties particular to the system of interest, such as lone-pair, conjugation, hydrogen bonding, and C_2 corrections [42]. The charge of each atom varies dynamically during the MD simulation and is calculated by using the charge equilibration (Qeq) method [43–45].

1.1.4 Statistical ensembles in molecular dynamics

The thermodynamic states of a system can be defined by a set of parameters, such as the number of atoms N, pressure P, volume V, temperature T, and energy E. These macroscopic quantities can be connected to the microscopic state of the system, with appropriate statistics. This kind of study, which connects macrocosm with microcosm, is known as statistical mechanics. The previously mentioned parameters are contained in the concept of ensembles, which are extensively used in molecular dynamics simulations. For example, a microcanonical (NVE) ensemble is commonly used when the system is isolated, and no energy exchange occurs with the surroundings. In this case, the number of particles N, and the volume V are kept constant as well. Another important ensemble is the canonical (NVT) ensemble, in which temperature T is conserved instead of the energy. Finally, a very useful ensemble for molecular dynamics is the constant temperature - constant pressure (NPT) ensemble, as it can enable the calculation of the system's density.

1.1.5 Thermostats and barostats

The ensemble averages that are obtained in conventional molecular dynamics simulations are equivalent to ensemble averages in the microcanonical (NVE) ensemble. However, in order to simulate real experimental conditions, where temperature and/or pressure are held constant, it is often desirable to perform simulations in other ensembles such as the canonical (NVT) or isothermal-isobaric (NPT) ensemble. For this reason, several thermostats have been developed, such as Andersen [46], Berendsen [47], Langevin [48],

Bussi [49], and Nosé-Hoover [50].

Andersen: The Andersen [46] thermostat works by selecting particles at random and having them "collide" with a heat bath by assigning to particles new velocities, that are sampled from the Maxwell-Boltzmann distribution. The number of particles affected, the time between "collisions", and how often it is applied to the system are possible variables of this thermostat [51].

Berendsen: The Berendsen [47] thermostat (also known as the weak coupling thermostat) functions by rescaling velocities to the selected kinetic energy, while including a relaxation term that allows the system to gradually reach the targeted value [51]. This thermostat suppresses fluctuations of the kinetic energy of the system and therefore cannot produce trajectories consistent with the canonical ensemble [52].

Langevin: The Langevin [48] thermostat introduces Brownian dynamics to the atomic motion, thus including the viscosity and random collision effects of an implicit solvent. The total force on each atom has the form:

$$F = F_{\text{interaction}} + F_{\text{friction}} + F_{\text{random}} \tag{1.19}$$

where, $F_{\text{interaction}}$ is the standard interactions calculated during the simulation, F_{friction} is the damping used to tune the "viscosity" of the implicit bath, and F_{random} effectively gives random collisions with solvent molecules. The frictional and random forces are coupled through a user-specified friction damping parameter [51].

Bussi: The Bussi [49] thermostat is similar to the Berendsen thermostat, but instead of rescaling to a single kinetic energy that corresponds to the target temperature, the rescaling is done to a kinetic energy that is stochastically chosen from the kinetic energy distri-

bution dictated by the canonical ensemble. As a result, this thermostat properly samples the canonical ensemble. As with the Berendsen thermostat, a user-specified time coupling parameter can be chosen to vary how abruptly the velocity rescaling takes place [51].

Nosé-Hoover: The Nosé-Hoover thermostat [50] abstracts away the thermal bath from the previous thermostats and condenses it into a single additional degree of freedom. This fictitious degree of freedom has a "mass" that can be changed to interact with the particles in the system in a predictable and reproducible way while maintaining the canonical ensemble. The choice of "mass" of the fictitious particle (which in many simulation packages is instead expressed as a time damping parameter) can be important as it affects the fluctuations that will be observed. For many reasonable choices of the mass, dynamics are well-preserved [53]. This is one of the most widely implemented and used thermostats. On the other hand, it should be noted that with small systems, ergodicity, which expresses the idea that over a long enough time interval the ensemble and time average of a property become equal, can be an issue [50,54]. Martyna et al. [54] brought to light that by chaining thermostats, ergodicity can be enhanced, and most implementations of this thermostat use Nosé-Hoover chains [51].

Similarly, if the pressure must be maintained during a simulation, a barostat algorithm is required in order to sample the ensemble. Barostat algorithms are used to keep pressure constant, which means that if the target ensemble is isothermal-isobaric, they must be applied with a thermostat. If a barostat is applied without a thermostat, only the number of particles (N), the pressure (P), and the enthalpy (H) of the system are held constant. This is known as the isoenthalpic-isobaric ensemble (NPH). To sample from the isothermal-isobaric ensemble (NPT), a thermostating algorithm like the ones discussed earlier must also be applied [51]. Popular barostasts include Andersen [46], Berendsen [47], Parrinello-Rahman [55] and Martyna-Tuckerman-Tobias-Klein [56, 57].

Andersen: First described by Andersen [46] in 1980, the system is coupled to a fictitious pressure bath, by adding an additional degree of freedom to the equations of motion. This behaves as if the system is being acted upon by an isotropic piston. This is similar to the Nosé-Hoover thermostat, which is also an extended system algorithm. This barostat does sample the correct ensemble. However, it is isotropic in nature and applying anisotropic pressures to parts of the system is not possible [51].

Berendsen: The Berendesen [47] weak coupling barostat is very similar to the Berendsen thermostat discussed earlier. By coupling the system to a weakly interacting pressure bath, which scales the volume periodically by a scaling factor, realisitc fluctuations in the pressure are produced as its value slowly approaches the target pressure. However, the ensemble it is sampling from is not well defined and cannot be guaranteed to be NPT or NPH. This barostat can be useful for the beginning stages of equilibration, but should not be used for production sampling [51].

Parrinello-Rahman: The Parrinello-Rahman [55] barostat is an extension to the Andersen barostat. Unlike the Andersen barostat, Parrinello-Rahman supports the anisotropic scaling of the size and shape of the simulation box. This can be quite useful in solid simulations, where phase changes can be shape changes in a crystal lattice, compared to a liquid or gas, which has no well-defined shape [51].

Martyna-Tuckerman-Tobias-Klein: The Martyna-Tuckerman-Tobias-Klein (MTTK) barostat is very similar to the Parrinello-Rahman and Andersen barostats. When Parrinello-Rahman's equations of motion were found to hold true only in the limit of large systems, the MTTK barostat introduced alternate equations of motion to correctly sample the ensemble for smaller systems as well [56, 57]. As a result, MTTK is usually seen as an

improvement over Parrinello-Rahman for such systems [51].

1.1.6 Periodic boundary conditions

Another important consideration in molecular dynamics simulations is the use of periodic boundary conditions (PBCs). These are used in order to avoid problems with boundary effects caused by finite size and to approximate a large (infinite) system by using one unit cell with defined dimensions. For example, the existence of PBCs means that any atom that leaves from the simulation box by the right boundary, will enter the simulation box by the left boundary. Figure 1.2 shows the concept of PBCs.

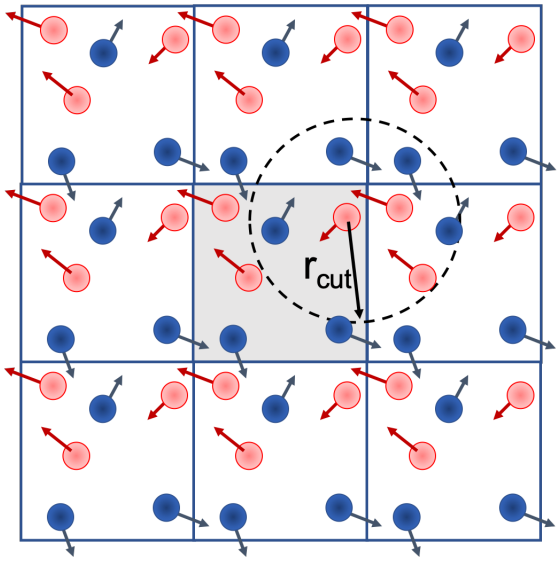

FIGURE 1.2: Schematic showing the use of periodic boundary conditions. Atoms leaving the principle cell are replaced by their image from the opposite cell. Short range interactions occur within the sphere defined by r_{cut}.

1.2 Simulation and modelling scale

With an increasing availability of high-performance computing, workstations and clusters, numerical computations have proved to be a powerful tool used in materials science and engineering. Nowadays, highly parallelised computer architecture allows scientists to

study the properties of materials by solving complex, nonlinear, many-body problems at different time and length scales with efficient algorithms as seen in Figure 1.3.

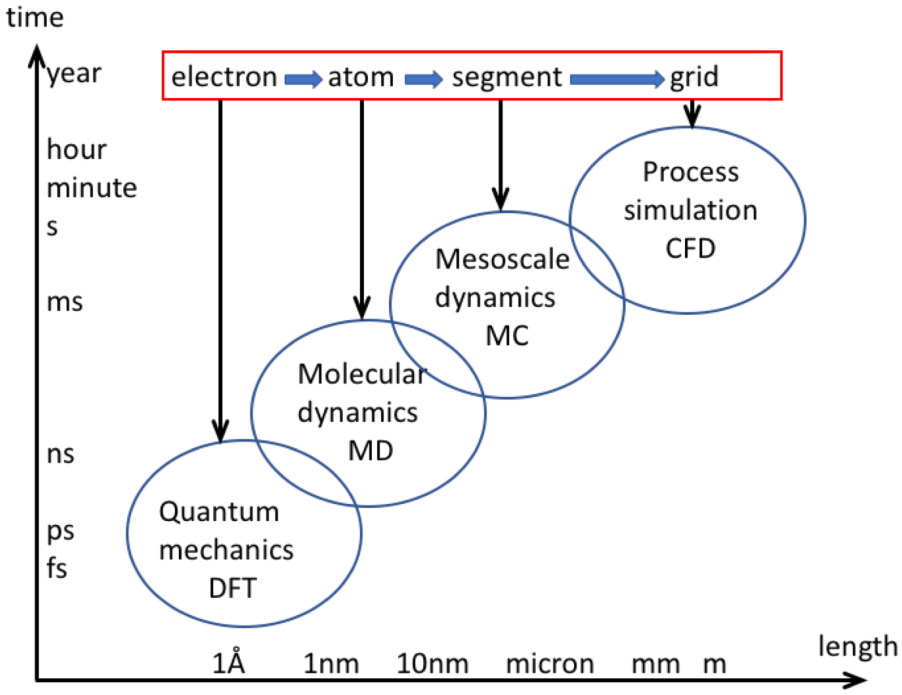

FIGURE 1.3: Computing techniques at different time and length scales. The level of theory determines the time and length scale.

For example, ab initio calculations based on quantum mechanics by using electronic structure theory, namely DFT with the Born-Oppenheimer approximation, are performed at the timescale of femto- and picosecond, and length scales of Ångströms and nanometers. Then, Molecular Dynamics and Monte Carlo (MC) simulations at the atomistic, microscopic, or even mesoscale are used to investigate a wide range of properties from thermodynamics to bulk properties of solids and fluids at the timescales of nano-, micro-, milli- and seconds, and length scales of nano-, micro- and millimeters. Finally, Computational Fluid Dynamics (CFD) simulations with continuum models perform bulk calculations to investigate the interaction of gases, liquids, and moving particles with surfaces defined by boundary conditions at the greatest time and length scales. Amine-based ad-

sorbents, including amine oligomers, have been theoretically studied from the electronic or atomic level with DFT to the grid level with CFD [58].

Chapter 2

Theoretical approaches for calculating viscosity with molecular dynamics

2.1 Equilibrium molecular dynamics

2.1.1 Autocorrelation function formalism

In this subsection, we will introduce the concept of autocorrelation given a sample of data that are collected over time. It is useful to the reader to become familiar with this statistical term, as it will be extensively mentioned in the following subsections when we define and formulate the equations for calculating zero shear viscosity with equilibrium molecular dynamics.

Autocorrelation is a mathematical representation of the degree of similarity between a given time series and a lagged version of itself over successive time intervals. It's conceptually similar to the correlation between two different time series, but autocorrelation makes use of the same time series twice: once in its original form and once lagged one or more time periods [59]. Given a signal $A(t)$, the autocorrelation function is defined by [60]:

$$C(t) = \langle A(0)A(t)\rangle = \lim_{\tau'\to\infty} \frac{1}{\tau'} \int_0^{\tau'} A(t_0)A(t_0+t)\,\mathrm{d}t_0 \tag{2.1}$$

Where τ' is time in the limit $\tau' \to \infty$, t is the time lag for comparing the signal of $A(t)$ with

itself and t_0 is a dummy variable that is only necessary to calculate the integral. By the above definition, several transport properties can be calculated, with zero shear viscosity being the main property of interest in this work. For signals that oscillate during an MD simulation, for instance, the equilibrium fluctuations of the pressure tensor, we see that the autocorrelation starts from perfect correlation (equal to one, after normalisation) and then decays to zero, as the signal is correlated with itself.

2.1.2 The pressure tensor

The pressure tensor $\sigma_{\alpha\beta}$ is a rank two tensor, as it is represented by a matrix (a 2-dimensional array), with off-diagonal elements $P_{\alpha\beta}$, which denotes the force acting along direction α on a unit surface perpendicular to the direction α, where α and β are the Cartesian directions x, y or z. The scalar pressure P is equal to the trace of the pressure tensor at rest:

$$P = \frac{1}{3}\sigma_{\alpha\alpha} \tag{2.2}$$

Then, the pressure tensor at rest is equal to:

$$\sigma_{\alpha\beta} = P\delta_{\alpha\beta} \tag{2.3}$$

While the pressure tensor in a moving fluid is equal to:

$$\sigma_{\alpha\beta} = P\delta_{\alpha\beta} + P_{\alpha\beta} \tag{2.4}$$

Where $\alpha, \beta = x, y, z$ and $\delta_{\alpha\beta}$ is the Kronecker delta. In matrix notation we have:

$$\sigma_{\alpha\beta} = \begin{bmatrix} \sigma_{xx} & 0 & 0 \\ 0 & \sigma_{yy} & 0 \\ 0 & 0 & \sigma_{zz} \end{bmatrix} + \begin{bmatrix} 0 & P_{xy} & P_{xz} \\ P_{yx} & 0 & P_{yz} \\ P_{zx} & P_{zy} & 0 \end{bmatrix} \tag{2.5}$$

Where $P_{\alpha\beta} = P_{\beta\alpha}$ due to symmetry. The value of the pressure tensor is the main parameter that is required for calculating viscosity in molecular dynamics simulations.

2.1.3 The Green-Kubo equation for zero shear viscosity

One of the main methods that allow the numerical calculation of zero shear viscosity of a liquid is Green-Kubo equilibrium molecular dynamics (EMD-GK), which is based on the fluctuation-dissipation theorem [61]. Green and Kubo proved [4, 5] that the coefficients describing the transport properties of the system can be represented as integrals of autocorrelation functions (ACFs). The zero shear viscosity coefficient η is calculated using the formula:

$$\eta_{\alpha\beta}(t) = \frac{V}{k_{\mathrm{B}}T}\int_0^t \langle P_{\alpha\beta}(0)P_{\alpha\beta}(t')\rangle \mathrm{d}t' \tag{2.6}$$

Where V is the volume of the particle system, T is temperature, k_{B} is the Boltzmann constant, $\langle ... \rangle$ is averaging over the ensemble that uses the three unique off-diagonal pressure tensor elements, namely P_{xy}, P_{yz}, P_{xz}, $\alpha\beta \equiv x, y, z$ and t' and t are time. Then, the zero shear viscosity is the average of the three viscosity components η_{xy}, η_{yz} and η_{xz}. For practical reasons in simulations, the upper limit of the above integral is set to a certain time, which is sufficiently long to ensure the noise-free decay of the ACF and convergence of viscosity [2]. Moreover, EMD-GK is known to work well for fluids with relatively low viscosity [62], typically less than 20 mPa s, which means that it is difficult to use this approach to compute viscosity at high pressures, where the viscosity of a lubricant is known to increase dramatically.

Let us define the autocorrelation function of the pressure tensor as a function of time:

$$C_{\alpha\beta}(t') = \langle P_{\alpha\beta}(0)P_{\alpha\beta}(t')\rangle \tag{2.7}$$

According to the ergodic hypothesis, the correlation of $P_{\alpha\beta}$ is obtained by an ensemble average over time [63] in the limit $t_{\max} \to \infty$ (t' is a time interval on which the correlation

function depends):

$$C_{\alpha\beta}(t') = \frac{1}{t_{\max} - t'} \int_0^{t_{\max}-t'} P_{\alpha\beta}(t'') P_{\alpha\beta}(t''+t')\,\mathrm{d}t'' \tag{2.8}$$

In the case of a molecular dynamics (MD) simulation, where we are dealing with discretised quantities, $t_{\max}$ is the total simulation time. The discretised form of eq. 2.8 is:

$$C_{\alpha\beta}(t') = \frac{1}{t_{\max} - (t' - \delta t)} \Big(\sum_{t''=0}^{t_{\max}-t'} P_{\alpha\beta,t''} P_{\alpha\beta,t''+t'} \Big) \delta t \tag{2.9}$$

The MD simulation timestep is δt (usually one femtosecond or less). As a result, we have that:

$$t' = N\delta t \tag{2.10}$$

$$t_{\max} = N_{\max}\delta t \tag{2.11}$$

where N and $N_{\max}$ are integer counters of simulation time steps. As a result, eq. 2.9 becomes:

$$C_{\alpha\beta}(N\delta t) = \frac{1}{N_{\max} - (N-1)} \sum_{t''=0}^{(N_{\max}-N)\delta t} P_{\alpha\beta,t''} P_{\alpha\beta,t''+N\delta t} \tag{2.12}$$

We can divide $N_{\max}$ into increasing time intervals by introducing an integer, k, and an autocorrelation time interval, $d\delta t$, such that $N_{\max} = k_{\max} d$ and $k = 0, 1, 2, \ldots, \frac{N_{\max}}{d}$, as we perform autocorrelation in $kd\delta t$ time intervals, up until the value of $N_{\max}$. This ensures the convergence of viscosity with time and increases the correlation time that we can sample. As a result, the ACF becomes a function of two variables, N and k:

$$C_{\alpha\beta}(N\delta t, kd\delta t) = \frac{1}{kd - (N-1)} \sum_{t''=0}^{(kd-N)\delta t} P_{\alpha\beta,t''} P_{\alpha\beta,t''+N\delta t} \tag{2.13}$$

Finally, if we define s as the sampling rate, i.e. every how many timesteps we sample pressure tensor values (for example if $s = 10$ we will sample at $0\delta t$, $10\delta t$, $20\delta t$, etc.), for

use in autocorrelation, $d = s\,p$ and eq. 2.13 becomes:

$$C_{\alpha\beta}(N\delta t, ksp\delta t) = \frac{1}{kp-(N-1)} \sum_{t''=0}^{(kp-N)\delta t} P_{\alpha\beta,t''s} P_{\alpha\beta,t''s+Ns\delta t} \tag{2.14}$$

where $N = 0, 1, 2, \ldots, (p-1)$, p terms in total, every s number of fs, the values of the pressure tensor are used, p is the number of autocorrelation terms, d is the autocorrelation time (constant number, a multiple of δt), which represents a fraction of the whole simulation where autocorrelation is performed, $C_{\alpha\beta}$ is the autocorrelation term of the pressure tensor, N is the correlation term index and k is the fraction index.

The instantaneous value of the pressure tensor at each time is given by the following equation:

$$P_{\alpha\beta}(t) = \frac{\sum_{i=1}^{K} m_i u_{i\alpha}(t) u_{i\beta}(t)}{V} + \frac{\sum_{i=1}^{K'} r_{i\alpha}(t) f_{i\beta}(t)}{V} \tag{2.15}$$

where $P_{\alpha\beta}$ is the value of pressure tensor at time t, m_i is mass, $u_{i\alpha}$ is velocity with index α, $r_{i\alpha}$ and $f_{i\beta}$ are the position and force vector components of atom i, with a total of K atoms, while K' extends the sum to include periodic image (ghost) atoms outside of the central simulation box, when periodic boundary conditions are enforced in conjunction with the minimum image convention. The use of ghost atoms is required so that all forces can be computed from each atom, within a specified cut-off distance.

Finally, eq. 2.6 is discretised with simple quadrature (trapezoidal rule) to obtain zero shear viscosity:

$$\eta_{\alpha\beta}(kd\delta t) = \frac{1}{2}\Big[C_{\alpha\beta,0}(kd\delta t) + 2\sum_{N=1}^{p-2} C_{\alpha\beta,N}(kd\delta t) + C_{\alpha\beta,p-1}(kd\delta t)\Big]\frac{V}{k_{\mathrm{B}}T} s\delta t \tag{2.16}$$

To ensure convergence, the viscosity has to be time-independent and this can be achieved by performing autocorrelation over an increasing number k of snapshot multiples during

the production run, as shown in eq. 2.16, with the same time origin (beginning of the production run).

For example, for $s = 1$ fs at any direction of $\alpha\beta$ we have (when $k = 0$: beginning of simulation):

$$C_{\alpha\beta,0}(kd) = \frac{1}{kp+1}\sum_{j=0}^{kp} P_{\alpha\beta,j}P_{\alpha\beta,j}, k \geqslant 0 \tag{2.17}$$

$$C_{\alpha\beta,1}(kd) = \frac{1}{kp}\sum_{j=0}^{kp-1} P_{\alpha\beta,j}P_{\alpha\beta,j+1}, k > 0 \tag{2.18}$$

$$C_{\alpha\beta,2}(kd) = \frac{1}{kp-1}\sum_{j=0}^{kp-2} P_{\alpha\beta,j}P_{\alpha\beta,j+2}, k > 0 \tag{2.19}$$

$$C_{\alpha\beta,p-1}(kd) = \frac{1}{kp-(p-2)}\sum_{j=0}^{kp-(p-1)} P_{\alpha\beta,j}P_{\alpha\beta,j+(p-1)}, k > 0 \tag{2.20}$$

Then, for $k = 1$, $s = 5$ fs, $p = 2$, $d = s \times p = 10$ fs at any direction of $\alpha\beta$:

$$C_0(kd) = \frac{1}{kp+1}\sum_{j=0}^{kp} P_{5j}P_{5j} \Rightarrow C_0(10) = \frac{1}{2+1}\sum_{j=0}^{2} P_{5j}P_{5j} = \frac{P_0P_0 + P_5P_5 + P_{10}P_{10}}{3} \tag{2.21}$$

and

$$C_1(kd) = \frac{1}{kp}\sum_{j=0}^{kp-1} P_{5j}P_{5j+5} \Rightarrow C_1(10) = \frac{1}{2}\sum_{j=0}^{1} P_{5j}P_{5j+5} = \frac{P_0P_5 + P_5P_{10}}{2} \tag{2.22}$$

And for $k = 2$:

$$C_0(20) = \frac{P_0P_0 + P_5P_5 + P_{10}P_{10} + P_{15}P_{15} + P_{20}P_{20}}{5} \tag{2.23}$$

and

$$C_1(20) = \frac{P_0P_5 + P_5P_{10} + P_{10}P_{15} + P_{15}P_{20}}{4} \tag{2.24}$$

Figure 2.1 summarises the above information. Every d fs the collected pressure tensor is correlated with itself, then it is shifted up to d fs in total.

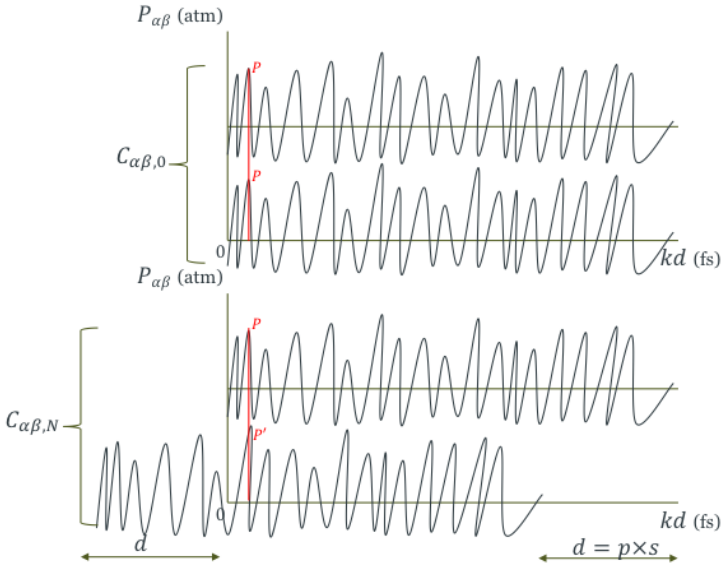

FIGURE 2.1: Autocorrelation of pressure tensor. The pressure tensor is correlated with its own image for a time duration of d fs. This process is repeated throughout the simulation.

2.2 Non-equilibrium molecular dynamics

2.2.1 Theoretical background

Although viscosity can be obtained by EMD, it is a non-equilibrium state. As a result, a method that uses this definition of viscosity is more intuitive to understand. This method, known as non-equilibrium molecular dynamics (NEMD), allows the calculation of viscosity with an applied shear rate ($\dot{\gamma}$). This is achieved by the use of perturbed equations of motion and imposing a shear field. In NEMD, in order to capture both Newtonian and shear thinning region, the suggested approach is to perform several simulations with different shear rates (velocity gradients), with the time-varying viscosity given by:

$$\eta(t) = -\frac{P_{xy}(t)}{\dot{\gamma}} \tag{2.25}$$

and

$$\dot{\gamma} = \frac{U_x}{h} \tag{2.26}$$

where η is the shear viscosity, P_{xy} is the value of the pressure tensor in the xy plane, $\dot{\gamma}$ is the shear rate, U_x is the applied velocity at the top edge of the simulation box and h is the box length in the y dimension. Figure 2.2 shows the shearing process in Couette flow of a viscous fluid, which has a linear velocity profile and is contained between two surfaces, one of which is moving, while the other remains stationary. Depending on whether or not the parallel plates are explicitly described, NEMD simulations can be bulk or confined. In bulk NEMD, the simulation cell includes the fluid's atoms only, while the shear flow involves the deformation of the simulation cell (xy plane) at a constant velocity, resulting in a linear velocity profile. On the other hand, in confined NEMD, the walls are explicitly described as atoms.

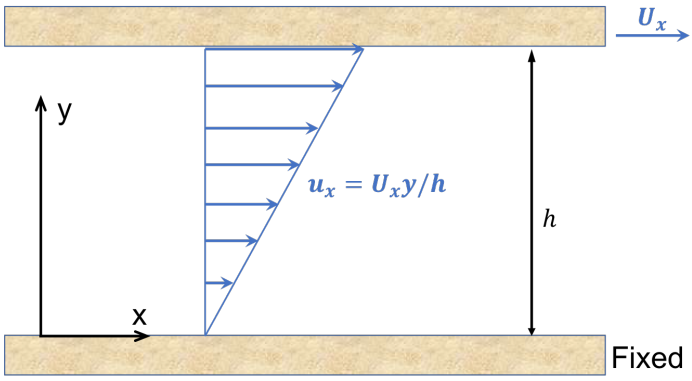

FIGURE 2.2: Schematic showing the shearing process in simple Couette flow. A shearing velocity is applied at the top edge of the simulation box, with the algorithm creating a linear velocity profile.

2.2.2 The SLLOD algorithm

An alternative method to conduct simulations of shear flow without using wall boundaries is to generate flow with a suitable implementation of periodic boundary conditions. The SLLOD algorithm [64, 65], which is compatible with Lees-Edwards "sliding-brick" boundary conditions [66] for shear flow of infinite extent, is a very efficient algorithm that

sets up a steady planar Couette flow with a velocity profile that is linear across the sample thickness. This allows the calculation of shear viscosity away from equilibrium with a constant shear rate ($\dot{\gamma}$), which is not directly applied to the sample, but is derived from the shear velocity and the sample thickness, as stated in eq. 2.26. In NEMD, in order to capture both Newtonian and shear thinning regions, it is essential to run several simulations with different shear rates. Based on the SLLOD formalism [64, 65], the equations of motion are given by:

$$\dot{\mathbf{r}}_i = \frac{\mathbf{p}_i}{m_i} + \mathbf{r}_i \cdot \nabla \mathbf{v} \tag{2.27}$$

$$\dot{\mathbf{p}}_i = \mathbf{F}_i^{\phi} - \mathbf{p}_i \cdot \nabla \mathbf{v} \tag{2.28}$$

Where $\mathbf{r}_i$ and $\mathbf{p}_i$ are the laboratory position and peculiar momentum, respectively of atom i with mass m_i, $\nabla \mathbf{v}$ is the gradient of the streaming velocity $\mathbf{v}$ and F_i^{ϕ} is the interatomic force on atom i due to all other atoms.

The main two types of homogeneous flow, consist of planar shear and planar elongational flow. For planar shear with flow in the x-direction and gradient in the y-direction, we have that [64]:

$$\nabla \mathbf{v} = \begin{bmatrix} 0 & 0 & 0 \\ \dot{\gamma} & 0 & 0 \\ 0 & 0 & 0 \end{bmatrix} \tag{2.29}$$

Where $\dot{\gamma} = \partial \mathrm{v}_x / \partial y$ is the magnitude of the velocity gradient, the shear rate. In this case $\nabla \mathbf{v} \cdot \nabla \mathbf{v} = 0$. On the other hand, for planar elongational flow (PEF), with expansion in the x-direction, contraction in the y-direction, and no field in the z-direction, the velocity gradient tensor is: [64]

$$\nabla \mathbf{v} = \begin{bmatrix} \dot{\varepsilon} & 0 & 0 \\ 0 & -\dot{\varepsilon} & 0 \\ 0 & 0 & 0 \end{bmatrix} \tag{2.30}$$

while

$$\nabla \mathbf{v} \cdot \nabla \mathbf{v} = \begin{bmatrix} \dot{\varepsilon}^2 & 0 & 0 \\ 0 & \dot{\varepsilon}^2 & 0 \\ 0 & 0 & 0 \end{bmatrix} \tag{2.31}$$

Where $\dot{\varepsilon}$ is the elongational strain rate.

It was later found [67], that the SLLOD algorithm has some instabilities when planar elongation flow is considered. To be precise, this instability led to a catastrophic non-equilibrium phase transition that destroyed the true structure of the fluid. It was identified that the source of this issue was a lack of momentum conservation, that resulted from numerical round-off errors. This led to the further development of the so-called "proper-SLLOD" algorithm or p-SLLOD [68], which addressed the issues as the exponential growth of the total linear momentum of the system in the contracting direction was no longer observed. Based on the p-SLLOD formalism, the equations of motion are now given by:

$$\dot{\mathbf{r}}_i = \frac{\mathbf{p}_i}{m_i} + \mathbf{r}_i \cdot \nabla \mathbf{v} \tag{2.32}$$

$$\dot{\mathbf{p}}_i = \mathbf{F}_i^{\phi} - \mathbf{p}_i \cdot \nabla \mathbf{v} - m_i \mathbf{r}_i \cdot \nabla \mathbf{v} \cdot \nabla \mathbf{v} \tag{2.33}$$

Note that for shear flow, which is our case and investigation in this work, $\nabla \mathbf{v} \cdot \nabla \mathbf{v} = 0$ [68] due to matrix multiplication and as a result the equations of motion become equal to the original SLLOD algorithm (eq. 2.28). This updated algorithm, the p-SLLOD method, is implemented in LAMMPS and was used in our work for the NEMD simulations of shear flow. The addition of a Nosé-Hoover thermostat in order to control temperature leads to the equations of motion taking the final form:

$$\dot{\mathbf{r}}_i = \frac{\mathbf{p}_i}{m_i} + \mathbf{r}_i \cdot \nabla \mathbf{v} \tag{2.34}$$

$$\dot{\mathbf{p}}_i = \mathbf{F}_i^{\phi} - \mathbf{p}_i \cdot \nabla \mathbf{v} - \zeta \mathbf{p}_i \tag{2.35}$$

$$\dot{\zeta} = \frac{1}{Q}\Big[\sum_{i=1}^{K} \frac{\mathbf{p}_i^2}{m_i} - N_f k_{\mathrm{B}} T\Big] \tag{2.36}$$

where ζ is the Nosé-Hoover thermostat multiplier and T is the targeted temperature which is related to the targeted kinetic energy K_0 by $T = 2K_0/N_f k_B$, where N_f is the number of degrees of freedom. Q is a parameter associated with an additional degree of freedom coupled to an external heat reservoir and should be chosen to correctly determine the average kinetic energy and its fluctuations [64]. Q represents [69, 70] the thermostat mass parameter and is given by the following equation:

$$Q = DKk_B T \tau_t^2 \tag{2.37}$$

where D, K, and τ_t refer to the system's dimension, the total number of atoms, and the thermostat relaxation time parameter, respectively.

2.2.3 Zero shear rate extrapolation models

Moreover, eq. 2.25 shows the Newtonian behaviour of a fluid, but fluids can also exhibit non-Newtonian behaviour, where viscosity depends on the applied shear rate. Different empirical and microscopic models are available [71] to characterise such behaviour of fluids out of which the Powell-Eyring model [72] is chosen in the present study, as it has been suggested that viscosity extrapolation schemes can be useful at very high pressures [27–29]. The Powell-Eyring model, although more mathematically complex, has certain advantages over other empirical models as it is based on the kinetic theory of liquids rather than empiricism:

$$\eta(\dot{\gamma}) = (\eta_0 - \eta_\infty)\frac{\sinh^{-1}(\tau\dot{\gamma})}{\tau\dot{\gamma}} + \eta_\infty \tag{2.38}$$

where η_∞ is the shear viscosity at infinite shear rate, η_0 is the shear viscosity at zero shear rate, τ is the characteristic relaxation time and $\sinh^{-1}$ denotes the inverse hyperbolic sine function. At shear rates higher than the critical shear rate $\dot{\gamma}_{cr} = 1/\tau$, the fluid transitions from Newtonian to non-Newtonian behaviour (shear thinning).

2.3 Confined non-equilibrium molecular dynamics

2.3.1 Definition of shear stress

In this subsection, we will introduce the concept of shear stress $\tau_{\alpha\beta}$ in fluids, where $\alpha\beta \equiv x, y, z$. As it will be shown in the following subsection, shear stress is very important for calculating viscosity in confined systems. We will also investigate the transition from macroscopic definitions and equations to microscopic definitions of shear stress.

First of all, a fluid is defined as a substance that deforms continuously while acted upon by any force tangential to the area on which it acts. Such a force is termed a shear force, and the ratio of the shear force to the cross-sectional area on which it acts is known as the shear stress [73]. Additionally, the physical meaning of stress is the internal resistive force to the deformation (due to strain) per unit area. By definition, we have that:

$$\tau = \frac{F}{A} \tag{2.39}$$

where τ is the shear stress, F is the applied force, and A is the area parallel to the direction of the applied force. Newton (1642–1727) postulated that, for the straight and parallel motion of a given fluid, the tangential stress between two adjoining layers is proportional to the velocity gradient in a direction perpendicular to the layers [73]. That is:

$$\tau = F/A \quad \propto \quad \partial u_x/\partial y \tag{2.40}$$

or

$$\tau = \eta \frac{\partial u}{\partial y} \tag{2.41}$$

where $\partial u/\partial y$ is the velocity gradient in the direction perpendicular to the flow and η is a constant for a particular fluid at a particular temperature. The latter coefficient is the so-called viscosity, which is a measure of a fluid's resistance to flow. Figure 2.3 illustrates the process for inducing shear stress.

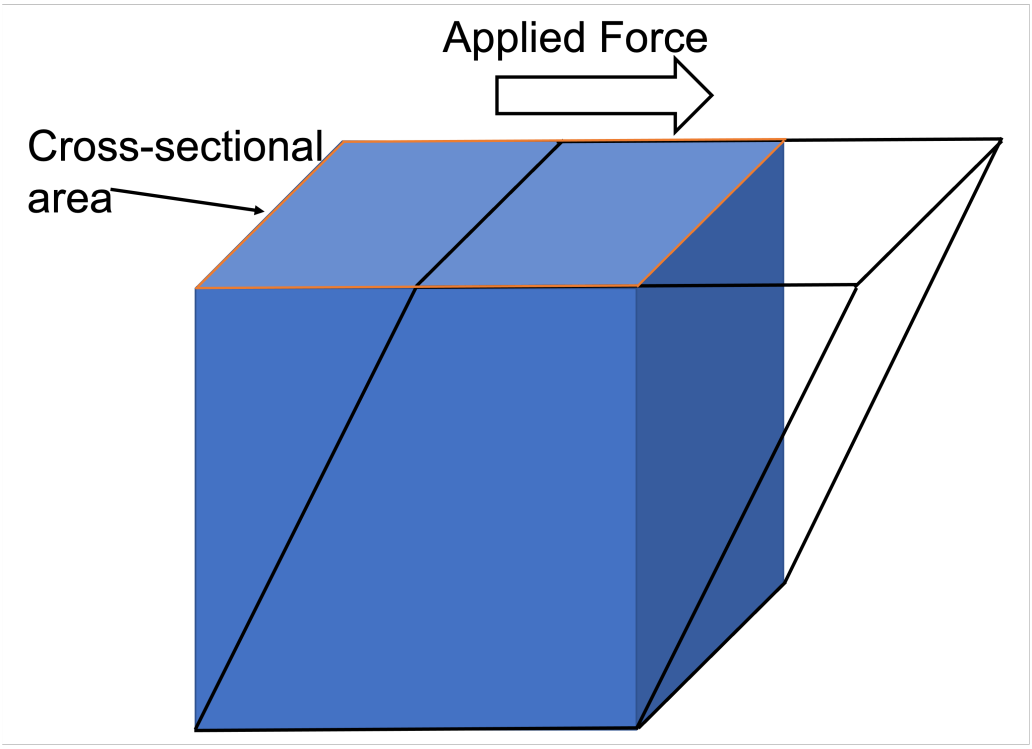

FIGURE 2.3: Physical illustration of deformation arising from an external applied force. Shear stress acts as an internal resistance to the deformation.

2.3.2 Calculation of viscosity in confined systems

As we saw in 2.3.1, if we solve eq. 2.41 for viscosity, it can be seen that we need to define microscopically and calculate the shear stress of the fluid in order to obtain shear viscosity after applying an external shear rate:

$$\eta_{\alpha\beta} = \frac{\langle \tau_{\alpha\beta} \rangle}{\dot{\gamma}} \tag{2.42}$$

where $\eta_{\alpha\beta}$ is the viscosity, $\langle \tau_{\alpha\beta} \rangle$ is the shear stress that is averaged over the ensemble, $\alpha\beta \equiv x,y,z$ and $\dot{\gamma}$ is the applied shear rate. There is a number of ways to extract shear stress in a molecular dynamics simulation. Those are:

Irving-Kirkwood method: According to the Irving-Kirkwood [74] expression (IK), the

pressure tensor at time t is equal to:

$$P(\mathbf{r},t) = \frac{1}{V}\Big[\sum_i m_i[\mathbf{v}_i(t) - \mathbf{u}(\mathbf{r}_i,t)][\mathbf{v}_i(t) - \mathbf{u}(\mathbf{r}_i,t)] + \frac{1}{2}\sum_{ij}\mathbf{r}_{ij}(t)O_{ij}(t)\mathbf{F}_{ij}(t)|_{\mathbf{r}_i(t)=\mathbf{r}}\Big] \tag{2.43}$$

where V is the volume of the system, $\mathbf{v}_i$ is the total particle velocity, $\mathbf{u}$ is the streaming velocity of the fluid, $\mathbf{F}_{ij}$ is the force on atom i due to atom j and O_{ij} is a differential operator which is equal to one when investigating the properties of fluids subject to pair interactions that have a uniform density. The $O_{ij} = 1$ approximation is called the IK1 expression [75]. The stress tensor is obtained by simply taking the negative value of the pressure tensor, i.e., $\tau(\mathbf{r},t) = -P(\mathbf{r},t)$.

Method of Planes: In the Method of Planes [75], the pressure tensor is the sum of a kinetic and a configurational component, i.e. $P_{\alpha\beta} = P^K_{\alpha y} + P^{\phi}_{\alpha y}$, which are given respectively by eq. 2.44 and eq. 2.46:

Kinetic component:

$$P^K_{\alpha y}(y,t) = \frac{1}{2A}\sum_i m_i u_{\alpha i}\frac{d}{dt}\mathrm{sgn}(y_i - y) - \rho u_\alpha u_y \tag{2.44}$$

where $P^K_{\alpha y}(y,t)$ is the kinetic part of the pressure tensor, t is time, y_i is the y-component of the position of particle i, y is the location of the plane, m_i and $u_{\alpha i}$ are the mass and velocity component of particle i, respectively, α is any of x, y or z, ρ is the mass density and sgn is the signum function:

$$\mathrm{sgn}(x) = \begin{cases} -1 & x < 0 \\ 0 & x = 0 \\ 1 & x > 0 \end{cases} \tag{2.45}$$

Configurational component:

$$P^{\phi}_{\alpha y}(y,t) = \frac{1}{2A}\sum_{ij} F^{\phi}_{\alpha ij}[\Theta(y_i - y)\Theta(y - y_j) - \Theta(y_j - y)\Theta(y - y_i)] \tag{2.46}$$

where $P^{\phi}_{\alpha y}(y,t)$ is the configurational part of the pressure tensor, $F^{\phi}_{\alpha ij}$ is the force on particle i due to particle j, α is any of x, y or z, A is the area, t is time, y_i and y_j are the y-components of the position of particle i and j, respectively, y is the location of the plane and Θ denotes the Heaviside step function:

$$\Theta(x) = \begin{cases} 0 & x \leqslant 0 \\ 1 & x > 0 \end{cases} \tag{2.47}$$

For the kinetic part, the algorithm considers that atoms have crossed the plane if their positions at times $t - dt$ and t are one on either side of the plane, and uses the velocity at time $t - dt/2$ given by the velocity-Verlet algorithm [76]. Again, the stress tensor is obtained by simply taking the negative value of the pressure tensor, i.e., $\tau(\mathbf{r},t) = -P(\mathbf{r},t)$.

Average shear force of lubricant atoms on the wall atoms, divided by the area of the walls:

One of the most frequently used expressions to calculate shear stress in MD [77] defines shear stress as the average shear force of lubricant atoms on the wall atoms, divided by the area of the walls:

$$\tau_{\alpha\beta} = \sum_{i=1}^{N_{\text{wall}}} \sum_{j=1}^{N_{\text{fluid}}} F^{ij}_{\alpha}/A \tag{2.48}$$

where $\tau_{\alpha\beta}$ is the shear stress, N_{wall} and N_{fluid} are the total number of wall and fluid atoms, respectively, $\alpha\beta \equiv x,y,z$, F^{ij}_{α} is the average shear force of lubricant atoms on the wall atoms and A is the area of the walls. This method of stress calculation has been found [77] to yield the same results as the Method of Planes [75] if the plane is chosen to be at the position of the walls. In addition, this method has been used [77] in conjunction with the previously mentioned Irving-Kirkwood [74] method, where it was found that both expres-

sions yield similar results. In order to improve the accuracy of results, both methods were used and the results were averaged.

Direct shear stress from average atom shear stress of lubricant atoms: The last method that will be discussed is the direct calculation of shear stress which is based on histograms of atomic stress. In this method, the stress tensor for atom I with mass m is given by the following equation:

$$\tau'_{\alpha\beta} = -mu_\alpha u_\beta - W_{\alpha\beta} \tag{2.49}$$

where $\alpha, \beta = x, y, z$ for generating the components of the tensor, $\tau'_{\alpha\beta}$ is the per-atom stress tensor for atom I, with velocity u_α and u_β, respectively and $W_{\alpha\beta}$ is the virial contribution which is given by the following equation:

$$\begin{aligned} W_{\alpha\beta} = & \frac{1}{2}\sum_{n=1}^{N_p}(r_{1\alpha}F_{1\beta} + r_{2\alpha}F_{2\beta}) + \frac{1}{2}\sum_{n=1}^{N_b}(r_{1\alpha}F_{1\beta} + r_{2\alpha}F_{2\beta}) \\ & + \frac{1}{3}\sum_{n=1}^{N_a}(r_{1\alpha}F_{1\beta} + r_{2\alpha}F_{2\beta} + r_{3\alpha}F_{3\beta}) + \frac{1}{4}\sum_{n=1}^{N_d}(r_{1\alpha}F_{1\beta} + r_{2\alpha}F_{2\beta} + r_{3\alpha}F_{3\beta} + r_{4\alpha}F_{4\beta}) \\ & + \frac{1}{4}\sum_{n=1}^{N_i}(r_{1\alpha}F_{1\beta} + r_{2\alpha}F_{2\beta} + r_{3\alpha}F_{3\beta} + r_{4\alpha}F_{4\beta}) + \text{Kspace}(r_{i\alpha}, F_{i\beta}) + \sum_{n=1}^{N_f} r_{i\alpha}F_{i\beta} \end{aligned} \tag{2.50}$$

The first term is a pairwise energy contribution where n loops over the N_p neighbours of atom I, r_1 and r_2 are the positions of the two atoms in the pairwise interaction, and F_1 and F_2 are the forces on the two atoms resulting from the pairwise interaction. The second term is a bond contribution of similar form for the N_b bonds which atom I is part of. There are similar terms for the N_α angle, N_d dihedral, and N_i improper interactions atom I is part of. There is also a term for the KSpace contribution from long-range Coulombic interactions, if defined. Finally, there is a term for the N_f fixes that apply internal constraint forces to atom I [78].

Note that, as defined in the formula, per-atom stress is the negative of the per-atom pressure tensor. It is also really a stress*volume formulation, meaning the computed quantity is in units of pressure*volume.

By adding the per-atom stress contributions (eq. 2.49) of the lubricant molecules and dividing by the volume of the fluid, the shear stress is calculated and has units of pressure:

$$\tau_{\alpha\beta} = \frac{\sum_{I=1}^{N''} \tau'_{\alpha\beta,I}}{V'} \tag{2.51}$$

Where $\tau_{\alpha\beta}$ is the total stress tensor of the fluid, V' is the fluid's volume, $\tau'_{\alpha\beta,I}$ is the per-atom stress of a lubricant molecule and N'' is the total number of atoms belonging to the fluid. If we take as an example, the case of shearing across the xz plane, then $V' = l_x l_y h$, where l_x and l_y are the lengths of the simulation cell in x and y direction, respectively and h is the average film thickness (z direction) of the fluid.

As the last method is more convenient, straightforward and is already among the implemented algorithms to calculate shear stress in LAMMPS, it was chosen for our study that is presented in Chapter 5. In addition, this method, that was used for calculating shear stress, was also used to define pressure in the lubricant region. The pressure was calculated by taking the negative trace of the diagonal components of the stress tensor (eq. 2.2) that were obtained from eq. 2.51. During the simulation the value of pressure was monitored in order to check that the applied pressure at the top outermost layer of iron oxide surface is equal to the pressure experienced by the confined fluid.

Chapter 3

Idealised model: zero shear viscosity with equilibrium molecular dynamics

3.1 Introduction

In this Chapter we will make use of the equations shown in section 2.1.3 for calculating viscosity at various temperatures and pressures with equilibrium molecular dynamics using the Green-Kubo equation [4, 5] (EMD-GK). This method calculates the zero shear viscosity of a liquid through integrals of the equilibrium fluctuations of the pressure tensor. In essence, these integrals are obtained by numerical quadrature of the ensemble average of the pressure tensor. The simulation box is periodic in all three dimensions. We present the advantages and discuss the limitations of using this method. We first examine the convergence of viscosity by varying the simulations parameters and we provide the computational method that was used for several molecules in order to calculate zero shear viscosity.

3.2 Computational methodology for simulation of zero shear viscosity

All molecular dynamics simulations for viscosity calculations were carried out by using the LAMMPS software [79], combined with some in-house developed scripts to perform autocorrelation and averaging of viscosity. LAMMPS is a classical molecular

dynamics open source C++ code, which includes potentials for a variety of molecular systems and its capabilities include computations with parallel architecture, coupled with accelerated performance on CPUs. The necessary files that included the coordinates of molecules, the simulation settings, such as the enforcement of periodic boundary conditions in three dimensions and the atomic charges needed for LAMMPS, were generated with Moltemplate [80]. Moltemplate is an open source software that can generate LAMMPS input scripts. The molecular system structures needed in Moltemplate were generated with Packmol [81], which reads simple .xyz file coordinates in order to fill simulation boxes of specified size with molecules that have randomised arrangement. The starting .xyz file coordinates were created with MolView [82], an intuitive, open source web application that can generate molecules by accessing online structural databases. The flowchart for building the molecular system can be seen in Figure 3.1.

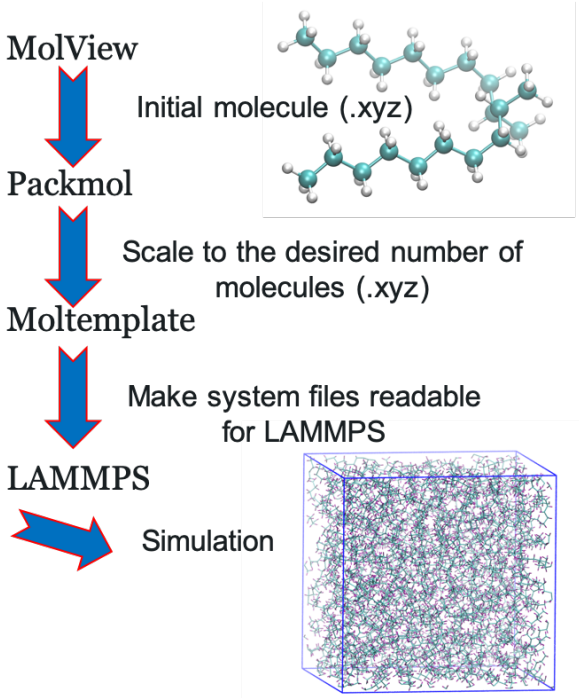

FIGURE 3.1: Step by step process for building the molecular system, starting from a single molecule. Each program takes as input the output of the previous program. For more information about the programs, see Appendix A.

3.2.1 The case of 9,10-dimethyloctadecane (PAO-2)

A box with a starting volume of $65.0 \times 65.0 \times 65.0$ Å^3, containing 170 9,10-dimethyloctadecane molecules (10,540 atoms) was generated and periodic boundary conditions were applied in all three dimensions. The atomic structure of the selected molecule prior to energy relaxation and equilibration can be seen in Figure 3.2. In this work, the L-OPLS-AA and GAFF2-AA force fields were chosen. The L-OPLS-AA [39] is a force field specifically optimised for long-chain hydrocarbons while GAFF2-AA is a general-purpose force field [40]. For both force fields, the cut-off radius for Lennard-Jones interactions was fixed at 13.0 Å [2], including a long-range Van der Waals tail correction [83] to the energy and pressure. "Unlike" Lennard-Jones interactions between different atoms (such as C and H) were evaluated using the geometric mean mixing rules [38] for calculating the potential wall depth ε_{ij} and the collision diameter σ_{ij} of pairwise interactions. For GAFF2-AA, an additional outer cut-off radius needs to be specified and was fixed at 15.0 Å, as it is typical to make the difference between the inner and outer cut-off radius about 2.0 Angstroms.

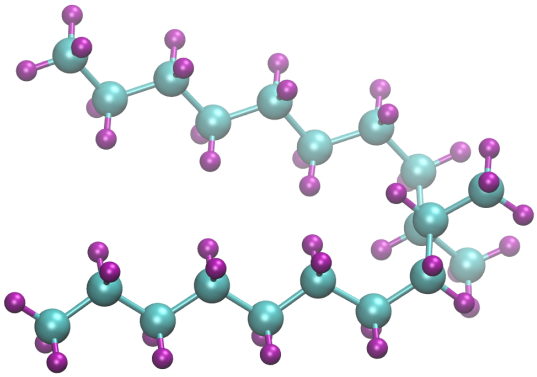

FIGURE 3.2: Molecular structure of 9,10-dimethyloctadecane, main component of PAO-2. Carbons are shown as cyan spheres and hydrogens as purple spheres. The conformation shown is prior to equilibration and therefore, has a relatively linear structure.

For L-OPLS-AA, long-range electrostatic interactions were not cut off, but were evaluated using the particle-particle particle-mesh (PPPM) method [84] with a relative force

accuracy of 10^{-4}. This method maps atomic charges to a three-dimensional mesh and uses Finite Fourier Transform to solve Poisson's equation on the mesh and then interpolates electric fields on the mesh points back to the atoms. In that way, each charge in the system interacts with charges in an infinite array of periodic images of the simulation domain. For GAFF2-AA, short-range electrostatic interactions require a cut-off radius, which was also fixed at 15.0 Å. This means that within this distance, interactions are computed directly, while interactions outside that distance are computed in conjunction with the PPPM method.

Initially, energy relaxation was achieved with the Polak-Ribiere version of the conjugate gradient (CG) algorithm. At each iteration the force gradient is combined with the previous iteration information to compute a new search direction perpendicular (conjugate) to the previous search direction. The tolerance for energy (unitless) was set to 10^{-5}, while the force tolerance was set to 10^{-7} kcal/(mol Å), with a maximum number of iterations equal to 100,000 and the max number of force/energy evaluations was 400,000.

Then, the simulation continued with a run of 2 ps in the isoenthalpic-isobaric (NPH) ensemble with a Langevin thermostat [48], in order to to allow the molecules to reorient themselves. This is not a necessary step, but it has been suggested that it can speed up density equilibration by randomising the molecules' coordinates and we have noticed that other molecules such as cyclohexane, would have a much slower density equilibration if this step is omitted. To equilibrate the density, a run of 20 ns in the isothermal-isobaric (NPT) ensemble followed, with a timestep of 1 fs, and the system's volume was allowed to vary until it reached equilibrium. To control temperature and pressure, a Nosé-Hoover thermostat and barostat [85, 86] were used at the temperature and pressure of choice with a time constant of 0.1 ps and 1 ps respectively. This was followed by a 2 ns run in the canonical (NVT) ensemble with a Nosé-Hoover thermostat. For 9,10-dimethyloctadecane, density equilibration took place at four selected temperatures, at 313, 343, 373 and 423 K (40, 70, 100 and 150 °C respectively), with pressure ranging from 0.1 MPa to 1.0 GPa (11

data points in total).

The zero shear viscosity (EMD-GK) was then calculated with the following procedure (case of L-OPLS-AA). The final state of the previous simulation, with a volume cell of equilibrated molecules, was used as the initial configuration (equilibrated density). It has been shown [6] that the use of multiple shorter independent trajectories instead of one single longer trajectory results in faster viscosity convergence. The average viscosity value of the replicas was the same as the viscosity result acquired from one single longer trajectory. In our study, in order to improve statistics, five independent trajectories were then produced by randomizing the initial configuration. This was achieved by heating and then cooling the initial configuration through separate cycles and then the pressure tensor was collected for each run. These heat-quench cycles [2] for simulations at 313 K were performed from 313 K to T = 315, 320, 325, 330, and 335 K respectively, during 1 ns runs in the NVT ensemble, after which the systems were immediately quenched back to 313 K during another 1 ns run in the NVT ensemble. Simulations at 373 K included heat-quench cycles that were from 373 K to T = 375, 380, 385, 390 K, and 395 K respectively, during 1 ns runs in the NVT ensemble, after which the systems were immediately quenched back to 373 K during another 1 ns run in the NVT ensemble. Then, the systems ran in the NVT ensemble for another 40 ns and the viscosity was calculated by the running average integral of the autocorrelation function of the pressure tensor in three dimensions as specified in the Green-Kubo method in eq. 2.16. The parameters that were used for autocorrelation were a sampling rate of s = 5 fs, with a number of autocorrelation terms p = 100,000 over a time period of $d = s\,p$ = 0.5 ns. Table 3.1 summarises the simulation setup.

Table 3.1: Description of simulation setup for 9,10-dimethyloctadecane.

Molecule	**Number of molecules**	**Number of atoms**	**Simulation box**	**Viscosity run**	**Force field**
9,10-dimethyloctadecane	170	10,540	$65.0 \times 65.0 \times 65.0$ Å^3	40 ns	L-OPLS-AA GAFF2-AA

3.2.2 Optimisation and convergence of shear viscosity calculation with *n*-hexadecane

In order to find the optimum parameters for autocorrelation of the pressure tensor, the following procedure was followed. Starting from a simulation with the equilibrated density of 130 *n*-hexadecane molecules at 300 K and 0.1 MPa, different parameters of s, p and consequently d were tested. Simulations were performed with a total run length from 5 to 42 ns on 2 and 4 nodes with the L-OPLS-AA force field. For s, the values of 1, 5 and 10 were chosen, while for p, the values were from 400 up to 1,000,000. Table 3.2 summarises the above information.

Then, the zero shear viscosity was calculated with the following procedure. For *n*-hexadecane, the density was equilibrated at 300 K (27 °C) and 0.1 MPa . The final state of the simulation, was used as the initial configuration for the zero shear. The optimised parameters extracted from the previous calculation of *n*-hexadecane's viscosity were used for the autocorrelation of the pressure tensor. These were s = 5 fs, p = 100,000 and $d = s\,p$ = 0.5 ns. For more information about the process of autocorrelation, see Appendix B, that includes our in-house C code that was developed to perform such task.

Table 3.2: Description of parameters tested for optimisation.

nodes	s **(fs)**	p	d **(fs)**	**Viscosity run**
2	1	200,000	200,000	20 ns
		300,000	300,000	15 ns
		400,000	400,000	10 ns
	5	400	2,000	5 ns
		600	3,000	5 ns
		800	4,000	5 ns
		6,000	30,000	5 ns
		8,000	40,000	5 ns
		12,000	60,000	5 ns
		20,000	100,000	5 ns
		25,000	125,000	5 ns
		30,000	150,000	5 ns
		40,000	200,000	5 ns
		50,000	250,000	5 ns
		60,000	300,000	36 ns
		100,000	500,000	5 ns
		100,000	500,000	40 ns
		200,000	1,000,000	40 ns
		300,000	1,500,000	42 ns
		400,000	2,000,000	40 ns
	10	200,000	2,000,000	40 ns
		300,000	3,000,000	42 ns
4	5	200,000	1,000,000	40 ns
		300,000	1,500,000	42 ns
		400,000	2,000,000	40 ns
		500,000	2,500,000	40 ns
		600,000	3,000,000	42 ns
		800,000	4,000,000	32 ns
		1,000,000	5,000,000	30 ns

Table 3.3: Description of simulation setup for *n*-hexadecane.

Molecule	**Number of molecules**	**Number of atoms**	**Simulation box**	**Viscosity run**	**Force field**
n-hexadecane	130	6,500	$65.0 \times 65.0 \times 65.0$ Å^3	40 ns	L-OPLS-AA

3.2.3 Determination of the pressure-viscosity coefficient of glycerol

The pressure-viscosity coefficient α of glycerol was calculated with the following procedure. Simulations for density equilibration took place at 303 K (30 °C) and the system was studied at various pressures from 0.1 MPa to 1.0 GPa (11 data points in total). All the other parameters were the same as the previous simulation for density equilibration. After equilibrating the density, the final state of each simulation was again used as the initial configuration for the viscosity calculation at elevated pressure. The parameters were again the same as the previous simulation for density equilibration except that 5 independent trajectories were produced by separate heat-quench cycles and then, the pressure tensor was collected for each run. For glycerol, the OPLS-AA force field was selected and the heat-quench cycles were from 303 K to 305, 310, 315, 320 and 325 K. This was achieved by 1 ns heat and 1 ns quench at NVT ensemble. The optimised parameters extracted from the previous calculation of the *n*-hexadecane's viscosity were used for the autocorrelation of the pressure tensor. These were s = 5 fs, p = 100,000 and $d = s\,p$ = 0.5 ns. Then, the pressure-viscosity coefficient was obtained with an exponential fit and linear *log* plots of the results, according to the Barus [87] equation:

$$\eta = \eta_0 e^{\alpha P} \Rightarrow \ln \frac{\eta}{\eta_0} = \alpha P \tag{3.1}$$

At a given temperature T, η_0 is the zero shear viscosity at ambient pressure, α is the pressure-viscosity coefficient, P is the elevated (higher) pressure and η is the zero shear viscosity at the elevated pressure.

Table 3.4: Description of glycerol's simulation setup for the calculation of pressure-viscosity coefficient.

Molecule	**Number of molecules**	**Number of atoms**	**Simulation box**	**Viscosity run**	**Force field**
glycerol	800	11,200	$65.0 \times 65.0 \times 65.0$ Å^3	40 ns	OPLS-AA

3.3 Force field parameters used in this study with EMD-GK

The following tables (Table 3.5 - 3.9) show the L-OPLS-AA parameters used in this work for *n*-hexadecane and 9,10-dimethyloctadecane simulations:

Table 3.5: Bonding parameters *n*-hexadecane and 9,10-dimethyloctadecane L-OPLS-AA.

Parameter	**Value** ($\frac{\textbf{kcal}}{\textbf{mol Å}^2}$)	**Type**	r_0 **(Å)**
k_1^{bond}	268.0	C-C	1.529
k_2^{bond}	340.0	C-H	1.090

Table 3.6: Angle parameters *n*-hexadecane and 9,10-dimethyloctadecane L-OPLS-AA.

Parameter	**Value** ($\frac{\textbf{kcal}}{\textbf{mol rad}^2}$)	**Type**	θ_0 **(deg)**
k_1^{angle}	58.35	C-Ĉ-C	112.7
k_2^{angle}	33.00	H-Ĉ-H	107.8
k_3^{angle}	37.50	C-Ĉ-H	110.7

Table 3.7: Dihedral parameters *n*-hexadecane and 9,10-dimethyloctadecane L-OPLS-AA.

C-C-C-C torsion	
Parameter	**Value (kcal/mol)**
k_1^{dihe}	0.645
k_2^{dihe}	-0.214
k_3^{dihe}	0.178
k_4^{dihe}	0.000
C-C-C-H torsion, H-C-C-H torsion	
Parameter	**Value (kcal/mol)**
k_1^{dihe}	0.000
k_2^{dihe}	0.000
k_3^{dihe}	0.300
k_4^{dihe}	0.000

Table 3.8: Dihedral parameters with CH- group for 9,10-dimethyloctadecane L-OPLS-AA.

CH-C-C-C torsion, C-C-CH-C torsion, C-CH-CH-C torsion, CH-CH-C-C torsion	
Parameter	**Value (kcal/mol)**
k_1^{dihe}	1.300
k_2^{dihe}	-0.050
k_3^{dihe}	0.200
k_4^{dihe}	0.000

Table 3.9: Non-bonded parameters *n*-hexadecane and 9,10-dimethyloctadecane L-OPLS-AA.

Atom	**Description**	ϵ **(kcal/mol)**	σ **(Å)**	q (e)
C	**C**H_3	0.066	3.50	-0.222
C	**C**H_2	0.066	3.50	-0.148
C	**C**H	0.066	3.50	-0.060
H	**H**$_3$-C	0.030	2.50	0.074
H	**H**$_2$-C	0.026	2.50	0.074
H	**H**-C	0.030	2.50	0.060

The following tables (Table 3.10 - 3.13) show the OPLS-AA parameters used in this work for glycerol simulations:

Table 3.10: Bonding parameters glycerol OPLS-AA.

Parameter	**Value** ($\frac{\textbf{kcal}}{\textbf{mol}\text{Å}^2}$)	**Type**	r_0 **(Å)**
k_1^{bond}	553.0	O-H	0.945
k_2^{bond}	320.0	O-C	1.410
k_3^{bond}	268.0	C-C	1.529
k_4^{bond}	340.0	C-H	1.090

Table 3.11: Angle parameters glycerol OPLS-AA.

Parameter	**Value** ($\frac{\textbf{kcal}}{\textbf{mol rad}^2}$)	**Type**	θ_0 **(deg)**
k_1^{angle}	55.00	H-Ô-C	108.5
k_2^{angle}	50.00	O-Ĉ-C	109.5
k_3^{angle}	58.35	C-Ĉ-C	112.7
k_4^{angle}	33.00	H-Ĉ-H	107.8
k_5^{angle}	35.00	O-Ĉ-H	109.5
k_6^{angle}	37.50	C-Ĉ-H	110.7

Table 3.12: Dihedral parameters glycerol OPLS-AA.

H-O-C-C torsion		**H-O-C-H torsion**	
Parameter	**Value (kcal/mol)**	**Parameter**	**Value (kcal/mol)**
k_1^{dihe}	-0.356	k_1^{dihe}	0.000
k_2^{dihe}	-0.174	k_2^{dihe}	0.000
k_3^{dihe}	0.492	k_3^{dihe}	0.352
k_4^{dihe}	0.000	k_4^{dihe}	0.000
O-C-C-O torsion		**O-C-C-C torsion**	
Parameter	**Value (kcal/mol)**	**Parameter**	**Value (kcal/mol)**
k_1^{dihe}	9.508	k_1^{dihe}	-1.552
k_2^{dihe}	0.000	k_2^{dihe}	0.000
k_3^{dihe}	0.000	k_3^{dihe}	0.000
k_4^{dihe}	0.000	k_4^{dihe}	0.000
O-C-C-H torsion		**C-C-C-H torsion, H-C-C-H torsion**	
Parameter	**Value (kcal/mol)**	**Parameter**	**Value (kcal/mol)**
k_1^{dihe}	0.000	k_1^{dihe}	0.000
k_2^{dihe}	0.000	k_2^{dihe}	0.000
k_3^{dihe}	0.468	k_3^{dihe}	0.300
k_4^{dihe}	0.000	k_4^{dihe}	0.000

Table 3.13: Non-bonded parameters glycerol OPLS-AA.

Atom	**Description**	ϵ **(kcal/mol)**	σ **(Å)**	q (e)
C	**C**H_2	0.066	3.50	0.145
C	**C**H	0.066	3.50	0.205
O	**O**H	0.170	3.07	-0.730
H	**H**O	0.000	0.00	0.465
H	**H**$_2$-C, **H**-C	0.030	2.50	0.060

3.4 Description of experimental viscometry

3.4.1 Experimental approaches for measuring viscosity at high pressures

A high-pressure viscometer is an instrument for the measurement of the shear viscosity at pressure significantly greater than atmospheric pressure so that the pressure dependence

may be accurately determined [88].

The operation of a viscometer at high pressure requires a pressure source. For pressures up to 200 and sometimes 400 MPa, commercial pressure generators or hand pumps are available. For greater pressures it is generally desirable to have a dedicated pressure intensifier connected to the viscometer by commercial high-pressure tubing and fittings that are available for pressures up to 1.4 GPa [88].

Falling body viscometers are simple devices that satisfy the low stress requirement. The shear stress is generated by gravity that is not attenuated by the thick walls of a pressure vessel. The only complication, therefore, is the need to measure the shear rate that is quantified indirectly by the falling velocity. The falling velocity may be observed optically through a transparent window, electromagnetically by a differential transformer, electrically by a pair of switches, or acoustically by measuring the time of flight of a sonic pulse reflected from the sinker. The falling body may be a ball or a cylinder. A ball may be in free fall but is usually allowed to roll either within an inclined tube or along an inclined plane. A falling cylinder is always contained within a cylindrical bore and is always guided toward concentricity with the bore either mechanically by a number of extending lugs at each end of the cylinder or hydrodynamically by shaping of the leading end of the cylinder. The falling cylinder configuration has the advantage over the falling ball that the shear stress of a measurement can be better defined [88].

A more recent development has been the diamond anvil viscometer. The diamond anvil cell generates extremely high pressure by squeezing a liquid, contained within a metal washer, between two diamond gems. This viscometer can operate to pressures that exceed the liquid range for ordinary liquid lubricants [88].

With a few rare exceptions, measurements of the shear dependence cannot be made with falling body viscometers. For this purpose, rotational or capillary viscometers are preferred. Rotational viscometers are of two different types, torsional and circular Couette. For example, torsional viscometers shear the sample between concentric parallel

discs. The shear stress can be determined from a measurement of torque and the shear rate obtained from the rotation rate of one of the discs, the other being stationary [88].

Sources of uncertainties in measured values during viscometer experiments, mainly include, the temperature, purity of lubricants, repeatability and the systematic error of the instrument [89]. The calculated standard uncertainty of viscosity measurements in a coaxial cylinder rheometer was found to be $\pm$ 0.0081 mPa s, in viscosity measurements of monoethanolamine and water mixture for the temperature range of 20 °C to 130 °C [89].

3.4.2 Experimental procedure for measuring viscosity at high pressures for PAO-2

The viscosity of PAO-2 (Spectrasyn 2 from ExxonMobil) was characterised experimentaly by Dr. S. Bair, in a falling cylinder viscometer [90]. The sinkers apply shear stress of less than 100 Pa so that the viscosity may be considered the limiting low shear value. Two viscometers, each employing two different sinkers, were used and the results were averaged. The uncertainty in temperature is 0.5 °C, 3 MPa in pressure and 3% in viscosity. The usual inflection in the pressure versus log viscosity curve is not present in this oil to 1 GPa at the temperatures investigated.

3.5 Analysis of results

3.5.1 Results for 9,10-dimethyloctadecane

Figure 3.3 shows a snapshot of this simulation with 9,10-dimethyloctadecane molecules after density equilibration. Carbon atoms are colored with cyan and hydrogen atoms with purple. Periodic boundary conditions are enforced in all directions. At that point, after equilibration in the NPT ensemble, the density had an average fluctuation of $\pm$ 0.005 g/mL (standard deviation, last 5 ns), which is a negligible difference of $\pm$ 0.6% and thus the system can be said to be stable.

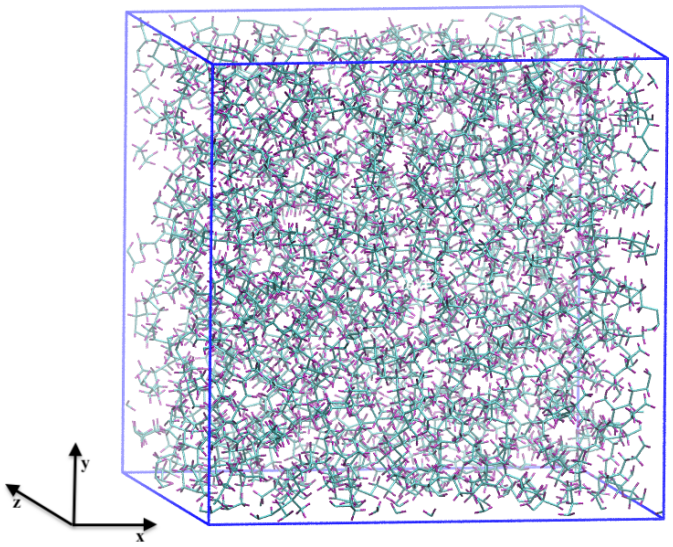

FIGURE 3.3: Equilibrated system of 9,10-dimethyloctadecane at 40 °C and 0.1 MPa using the L-OPLS-AA force field. The system was created with Moltemplate [80] and Packmol [81]. See Appendix C for example scripts for using those two programs.

The pressure–density response of hydrocarbons is commonly described using the Tait equation [91]:

$$\frac{\rho(P)-\rho_0}{\rho(P)} = C\log_{10}\left(\frac{B+P}{B+P_0}\right) \tag{3.2}$$

Where C and B are fitted parameters, ρ is the density at pressure P and ρ_0 is the density at ambient pressure P_0. The parameters that were used for the fits to the Tait equation in Figure 3.4 are given in Table 3.14. For all of the force fields and conditions studied, the Tait equation provided an excellent estimation of the density acquired from the MD simulations (average density, last 5 ns), as demonstrated by the low root mean square error (RMSE).

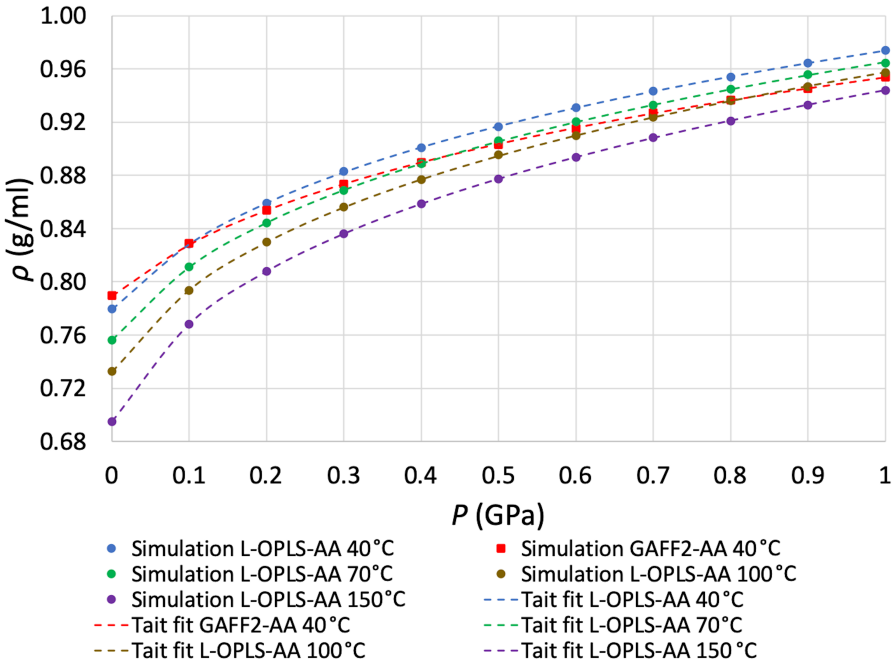

FIGURE 3.4: The dependence of density on pressure for 9,10-dimethyloctadecane at 40, 70, 100 and 150 °C. Circles indicate density results by using the L-OPLS-AA force field, while squares indicate results acquired with the GAFF2-AA force field. The dashed lines indicate Tait fits (eq. 3.2) to the MD simulation data. The parameters that were used for the fits are given in Table 3.14.

Table 3.14: Parameters with the root mean square error (RMSE) used in the Tait fits (eq. 3.2) for the MD data in Figure 3.4. The root mean square errors are between simulation data and the Tait approximations. Note that P_0 is equal to 0.1 MPa.

Force Field	ρ_0 (g/ml)	C	B (MPa)	RMSE (g/ml)	T (°C)
L-OPLS-AA	0.780 ± 0.005	0.1864	93.0	0.0003	40
GAFF2-AA	0.790 ± 0.004	0.1786	121.9	0.0004	40
L-OPLS-AA	0.756 ± 0.005	0.1912	79.5	0.0003	70
L-OPLS-AA	0.733 ± 0.005	0.1959	67.2	0.0003	100
L-OPLS-AA	0.695 ± 0.007	0.1991	49.5	0.0002	150

The choice of t for the upper limit of the EMD-GK integral (eq. 2.6) cannot be known *a priori* as it depends on the selected molecule and conditions such as temperature and pres-

sure. For this reason, it was determined by using various d time values of autocorrelation until the viscosity estimate for a given simulation replica (trajectory) converges (Figure 3.5). This behaviour shows that the autocorrelation function of the pressure tensor has successfully decayed to zero. As can be seen from the graph, performing autocorrelation for 0.5 ns, with sufficient data points of the pressure tensor, results in an accurate estimate within the region of applicability of EMD-GK. It is found that the EMD-GK method is applicable to pressures up to 0.3 GPa as at higher pressures, the method has issues with the decay of the autocorrelation function of the pressure tensor (highly viscous systems).

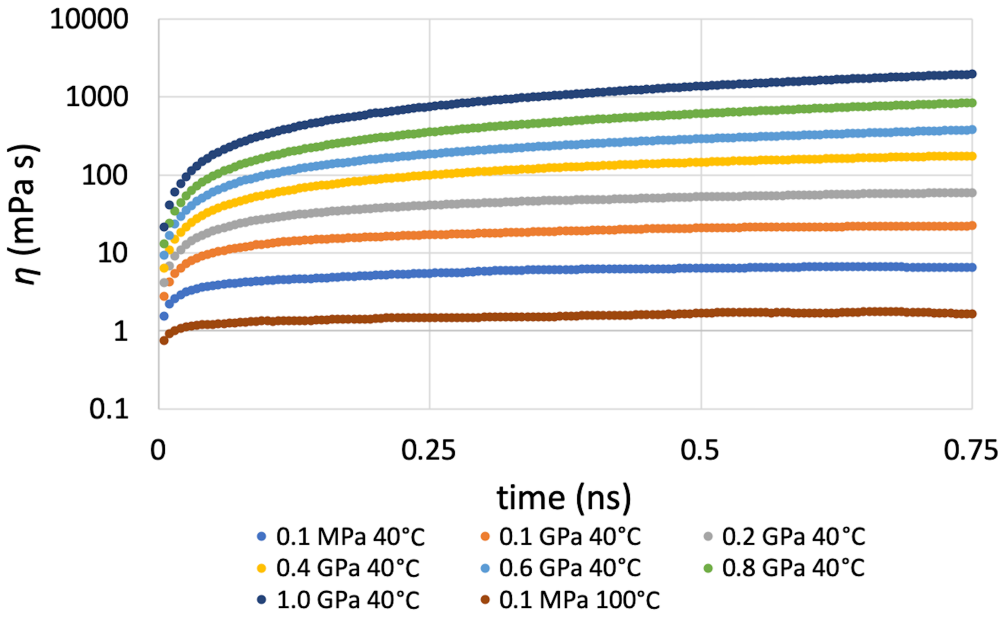

FIGURE 3.5: Convergence of viscosity for various d time values of autocorrelation for 9,10-dimethyloctadecane at 40 °C and pressures from 0.1 MPa to 1.0 GPa and 100 °C at 0.1 MPa. The pressure tensor values are used every s = 5 fs during the production run of 40 ns.

The ratio between the dynamic (low shear) viscosity and the density of a fluid is equal to the kinematic viscosity. By using the L-OPLS-AA force field, the simulated (zero shear rate, EMD method) kinematic viscosity of 9,10-dimethyloctadecane at 100 °C and 0.1 MPa was equal to 2.0 $\pm$ 0.3 mm^2/s, which is in close agreement with the experimental

value of 1.8 mm^2/s [92], as it was overestimated by just 14%. The kinematic viscosity at 40 °C was found to be 6.8 $\pm$ 0.8 mm^2/s, which yields an overestimation of 28% when compared with the experimental value of 5.3 mm^2/s [92]. Then, the running integral (equal to the zero shear viscosity) of the autocorrelation function of the pressure tensor at 40 °C and pressures from 0.1 MPa to 1.0 GPa for 9,10-dimethyloctadecane can be seen in Figure 3.6. It is necessary that simulations run for long enough, so that the viscosity result converges.

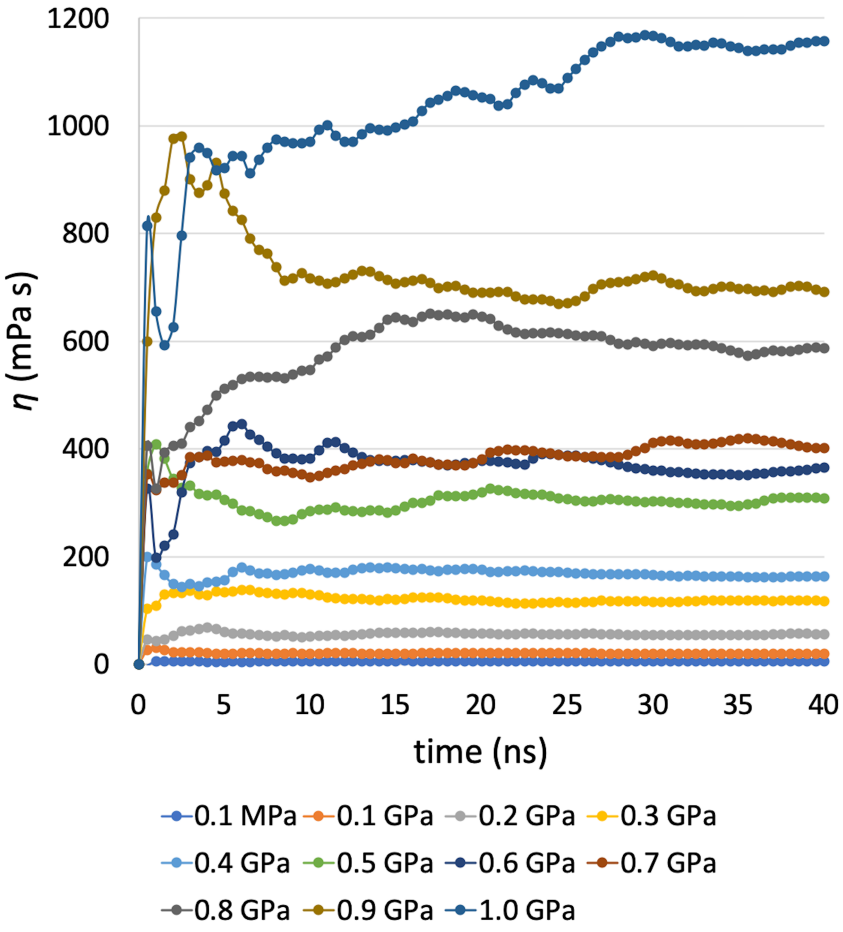

FIGURE 3.6: Convergence of viscosity with time. Running EMD-GK integral of 9,10-dimethyloctadecane zero shear viscosity at 40 °C and pressures from 0.1 MPa to 1.0 GPa using the L-OPLS-AA force field. Five trajectories are used to calculate the average value and the autocorrelation is performed by using the pressure tensor every $s = 5$ fs with a total number of $p = 100{,}000$ autocorrelation terms.

3.5.2 Results for *n*-hexadecane

As specified in 2.1.3, the p parameter is the total number of autocorrelation terms $C_{\alpha\beta,N}$, as described in the previously mentioned equation:

$$\eta_{\alpha\beta}(kd\delta t) = \frac{1}{2}\Big[C_{\alpha\beta,0}(kd\delta t) + 2\sum_{N=1}^{p-2} C_{\alpha\beta,N}(kd\delta t) + C_{\alpha\beta,p-1}(kd\delta t)\Big]\frac{V}{k_{\mathrm{B}}T}s\delta t \qquad (3.3)$$

A mathematical interpretation of this p parameter, is the total number of known points of the function that is numerically integrated (trapezoidal rule), which in our case is the autocorrelation function of the pressure tensor.

To begin with, Figure 3.7 shows the convergence plot for *n*-hexadecane's viscosity for various values of p parameter. There is a tendency for convergence at a value of around 3.1 mPa s, with the experimental value being at 2.9 mPa s. As we increase the number of autocorrelation terms, numerical integration converges. Therefore, a sufficient number of autocorrelation terms is needed in order to acquire an accurate result. Then, in Figure 3.8, different viscosity values can be seen for the same system, but for various values of s, increased simulation times and even more increased values of p. From this plot it is clear that s = 10 fs is not a good option, while s = 1 fs is the most computationally expensive choice, as it increases the number of pressure values used in autocorrelation. As a result, s = 5 fs is chosen for further investigation with the choice of parameter p. Figure 3.9, shows the final convergence plot for *n*-hexadecane. Results suggested that for $p >$ 100,000 and p $<$ 60,000 *xy*, *xz*, *yz* viscosity components diverge in respect to each other, which is the opposite that one expects for isotropic systems. As a result, the optimised value for p is set to 100,000 as it is an accurate and computationally efficient choice.

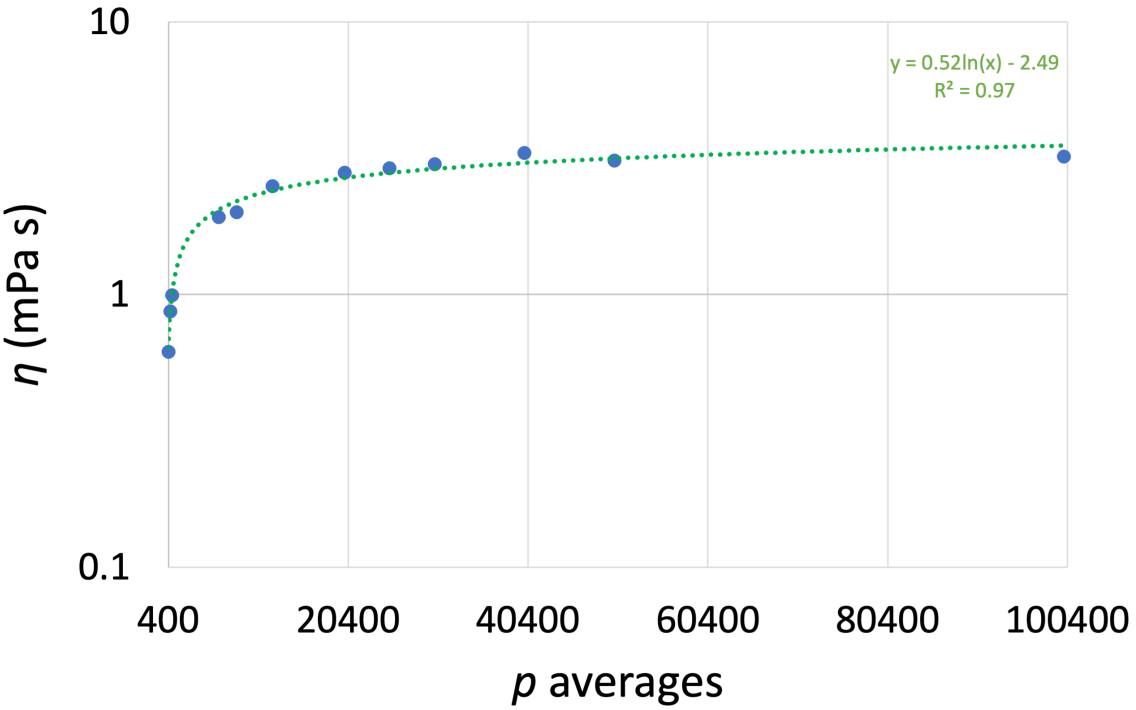

FIGURE 3.7: Convergence of viscosity by increasing the number of p correlation averages, with a single run of 5 ns with n-hexadecane at 300 K (27 °C), 0.1 MPa, with 130 molecules. The green dashed line represents a log fit to the data.

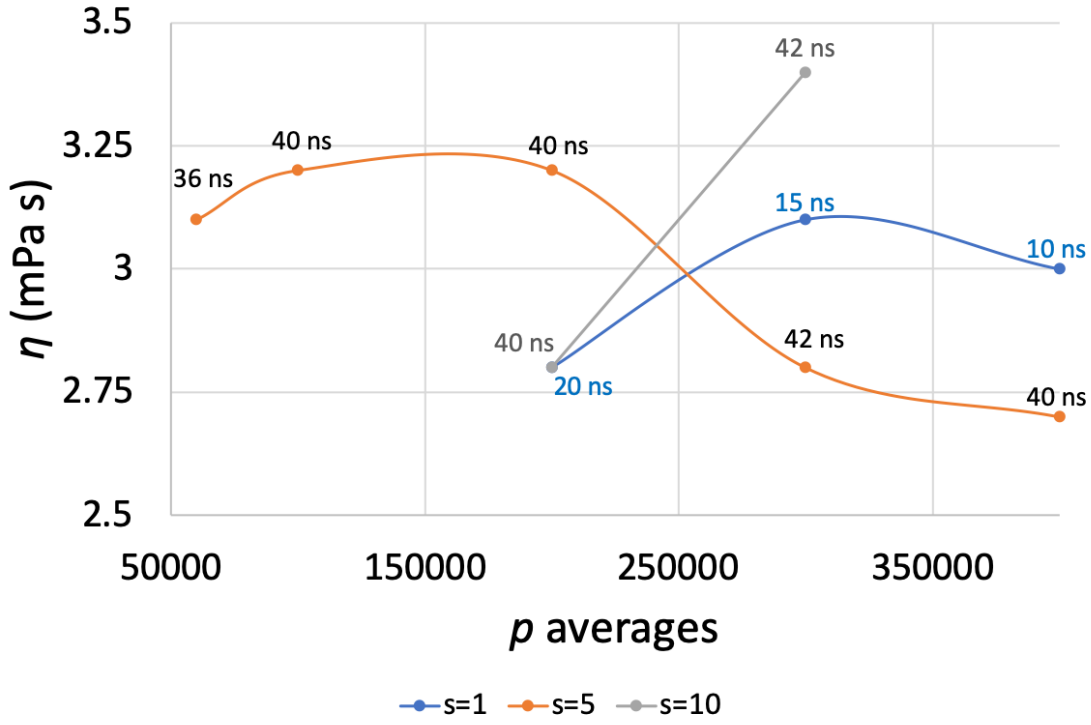

FIGURE 3.8: Viscosity as a function of the sampling rate (s fs) and the number of p correlation averages.

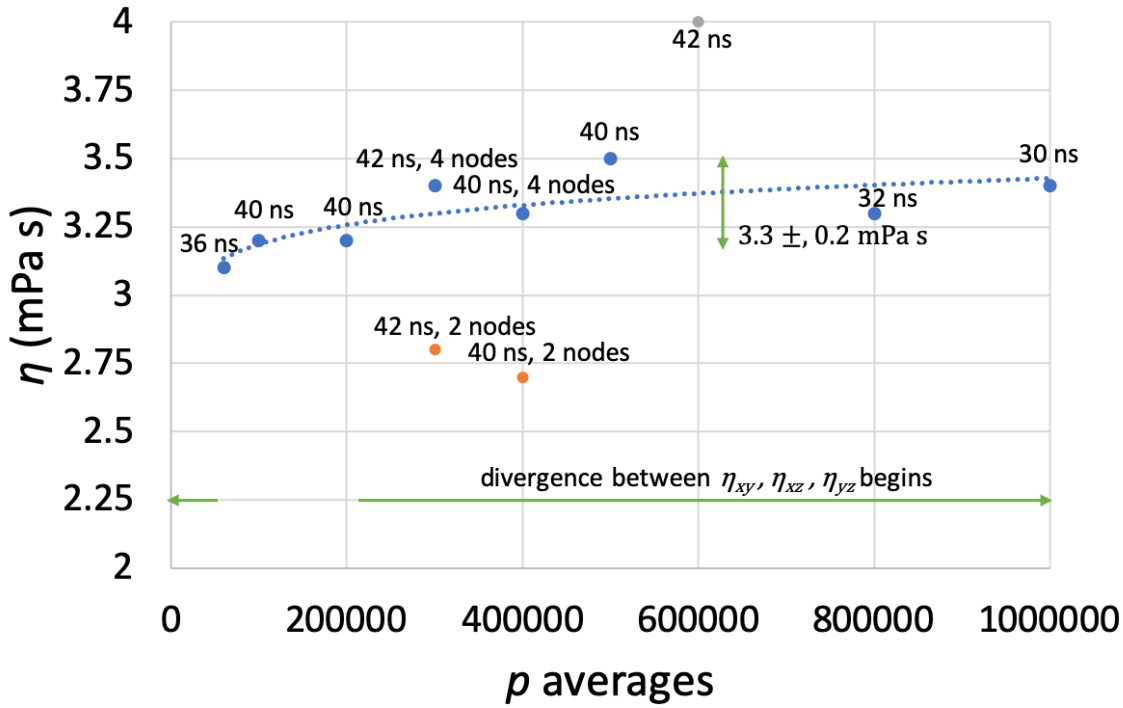

FIGURE 3.9: Final convergence of viscosity as a function of the number of p correlation averages with a sampling rate of $s = 5$ fs.

Then, the optimised autocorrelation parameters were applied for all the other systems. Density and viscosity results of EMD simulations of *n*-hexadecane can be seen in Table 3.15. It can be seen that density equilibration was quite accurate, and the EMD method is in good agreement with experiment. Figure 3.10 shows the molecular orientation of *n*-hexadecane after density equilibration. Carbon atoms are coloured with green and hydrogen atoms with grey. Periodic boundary conditions are enforced in all directions. At this point, the density fluctuated insignificantly, which means that the system is stable. The equilibrated density of *n*-hexadecane for the production run of 20 ns (in NPT) can be seen in Figure 3.11. The system reached equilibrium rapidly. Then, the running integral of the autocorrelation function of the pressure tensor for *n*-hexadecane, which is equal to the zero shear viscosity, can be seen in Figure 3.12. It is clear that one has to run long enough simulations, so that the viscosity estimate converges. This means that the output viscosity value has to be quite close to the previous one.

Table 3.15: Density and viscosity results for EMD simulations of *n*-hexadecane and comparison with literature [6]. The density was averaged during the last 5 ns of the equilibration run and the viscosity was averaged during the last 5 ns of the production run. The subscript next to the symbols denotes degrees in Celsius.

Molecule	d_{27} **(g/ml)**	d_{27} **exp. (g/ml)**	η_{27} **EMD (mPa s)**	η_{27} **exp. (mPa s)**
n-hexadecane	0.77 ± 0.005	0.76	3.2 ± 0.03	2.9

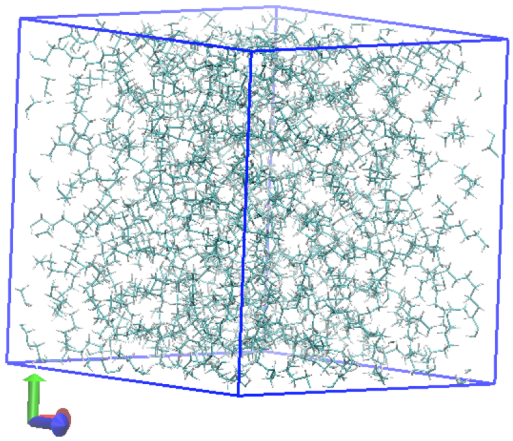

FIGURE 3.10: Equilibrated *n*-hexadecane L-OPLS-AA. PBCs are enforced in all three dimensions.

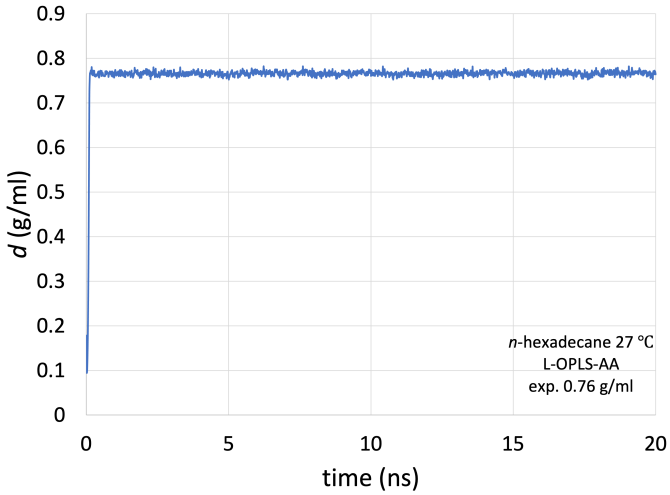

FIGURE 3.11: Density of *n*-hexadecane, at 300 K (27 °C), 0.1 MPa, with 130 molecules. The system reached equilibrium quite rapidly.

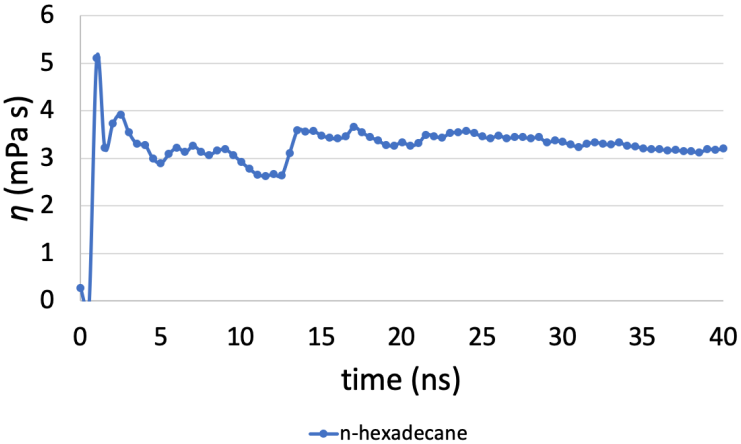

FIGURE 3.12: Running integral (single run) of *n*-hexadecane's zero shear viscosity (EMD-GK) at 300 K (27 °C), 0.1 MPa, with p =100,000 and s = 5 fs.

Finally, in Figure 3.13 and 3.14, we present the plot of the autocorrelation function of *n*-hexadecane for different time scales. The average value of the ACF oscillation is around 10^{-5} when $t \rightarrow 0.5$ ns, which means that the integrated ACF fluctuations do not contribute significantly to the viscosity estimate. This behaviour proves that performing autocorrelation for 0.5 ns, with sufficient data points of the pressure tensor, results in an accurate estimate.

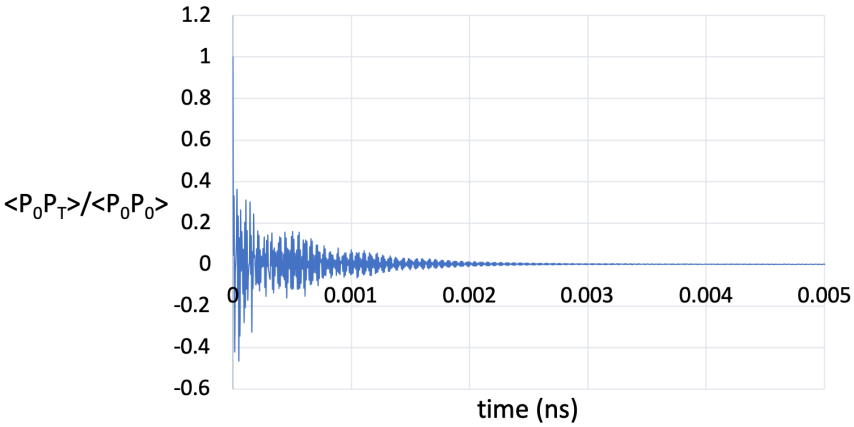

FIGURE 3.13: Autocorrelation function of *n*-hexadecane at 300 K (27 °C), 0.1 MPa.

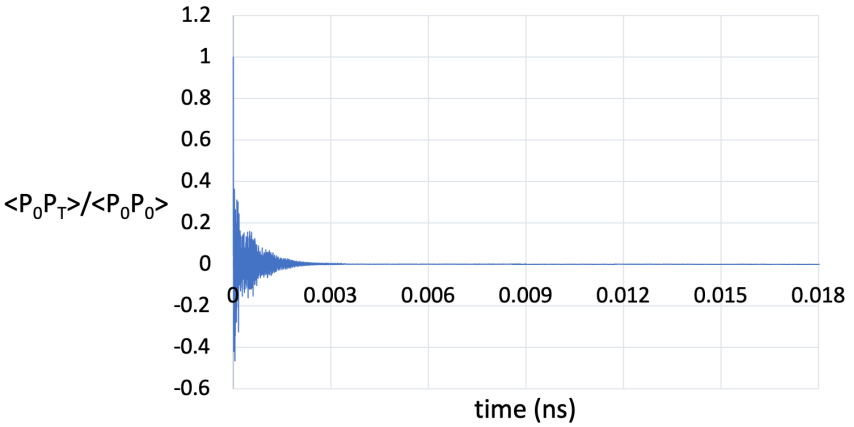

FIGURE 3.14: Autocorrelation function of *n*-hexadecane at 300 K (27 °C), 0.1 MPa, with more points (*x* values extend up to 0.5 ns).

3.5.3 Results for glycerol

Referring to the determination of viscosity-pressure behaviour of glycerol, Figure 3.15 shows the behaviour of independent glycerol trajectories and how the individual running viscosity integral contributes to the running average (Figure 3.16). In the beginning, the viscosity estimates of the five individual trajectories are quite different, but tend to converge with lower deviation as we approach the end of the simulation. Their running average viscosity converges earlier, an observation that is known in literature [6]. As a result, it is clear that using many independent trajectories, improves the statistical behaviour of viscosity. The zero shear viscosity results of glycerol can be seen in Figure 3.17. Viscosity converged for all different pressures, but simulations did not capture an exponential behaviour of viscosity at high pressures. An exponential fit shows that the Barus equation holds place up to a point but then breaks down. Table 3.16 summarises the EMD simulation results of glycerol. There is very good agreement between simulated and experimental values of density and zero shear viscosity. However, the pressure-viscosity coefficient was substantially underpredicted.

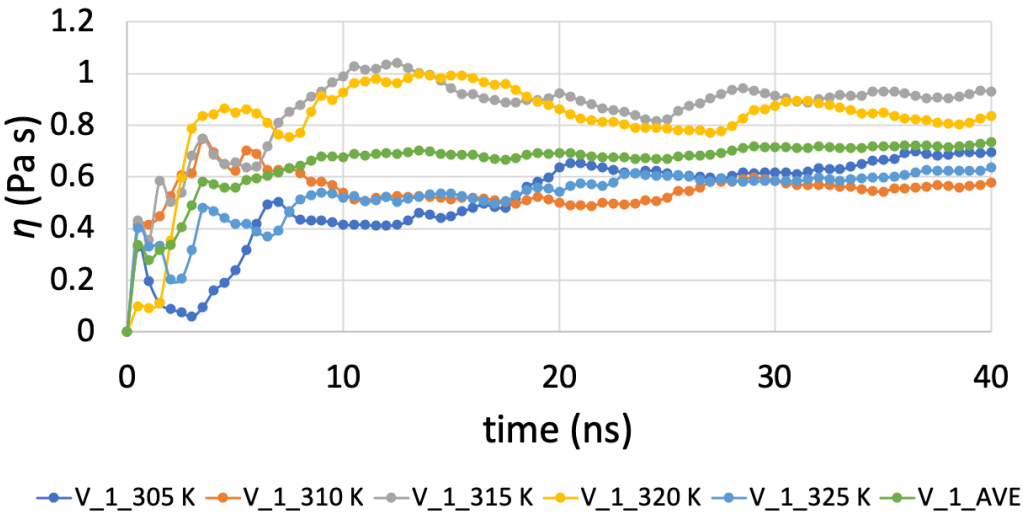

FIGURE 3.15: Running viscosity integrals of five independent trajectories of glycerol at 30 °C, 0.1 MPa, with OPLS-AA force field and 800 glycerol molecules.

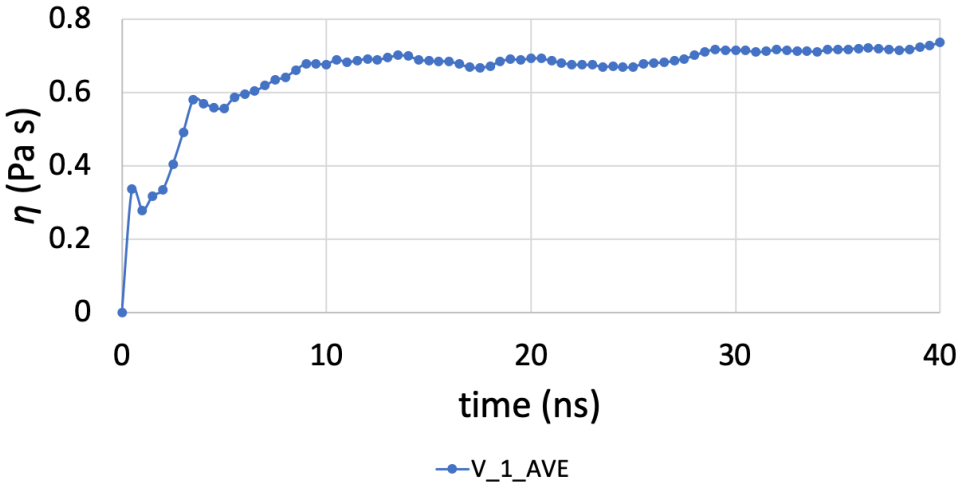

FIGURE 3.16: Running average viscosity integral of glycerol at 30 °C, 0.1 MPa, with OPLS-AA force field and 800 glycerol molecules. The average viscosity is the result of five independent trajectories.

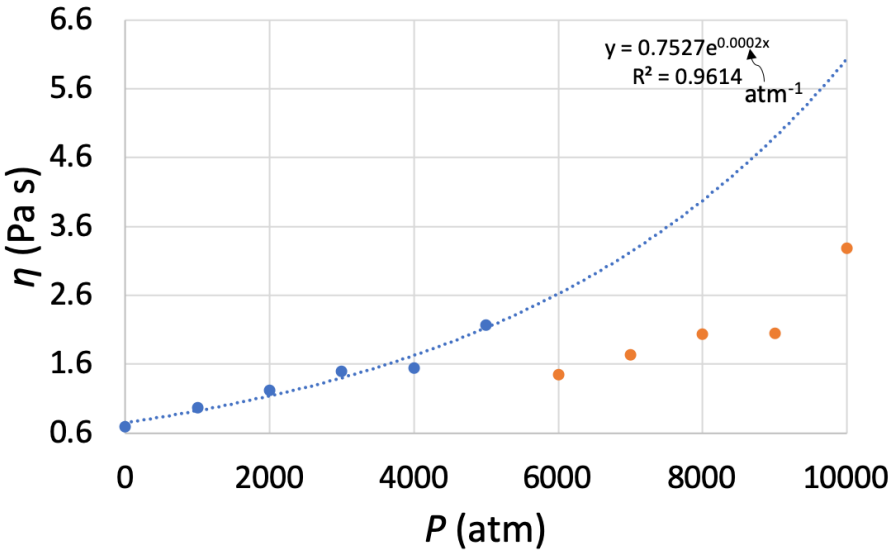

FIGURE 3.17: Viscosity pressure relationship of glycerol's EMD simulation at 30 °C at a pressure range of 1 to 10,000 atm (0.1 MPa to 1.0 GPa). The Green-Kubo method fails to capture the exponential behaviour of viscosity, due the increase of the relaxation time and viscosity of glycerol.

Table 3.16: EMD simulation results of glycerol and comparison with literature [93–95]. The density was averaged during the last 5 ns of the equilibration run and the viscosity was averaged during the last 30 ns of the production run. The subscript next to the symbols denotes degrees in Celsius.

Molecule	d_{30} **(g/ml)**	η_{30} **(Pa s)**	a_{30} **(m^2/N)**	**Force field**
glycerol	1.24 ± 0.004	0.7 ± 0.02	2.0×10^{-9}	OPLS-AA
glycerol exp.	1.26	0.6	5.9×10^{-9}	-

3.6 Summary

In this Chapter we explored the use of Green-Kubo equilibrium molecular dynamics (EMD-GK) for calculating the zero shear viscosity of several lubricants, including *n*-hexadecane, glycerol, and 9,10-dimethyloctadecane, main component of PAO-2 base oil. By varying simulation parameters for calculating the autocorrelation function (ACF) of the pressure tensor, we ensured viscosity convergence. However, it was found that at high pressures, the ACF does not converge to zero due to the increase of the rotational relaxation time of the molecule. This results in underprediction of the viscosity. We therefore showed that EMD-GK is applicable in certain regions, and these regions depend on each molecule's relaxation time, which refers to the required time for molecular chains to reach equilibrium after an external perturbation.

For the case of 9,10-dimethyloctadecane, we demonstrated that EMD simulations, which represent zero shear conditions, were accurate at predicting zero shear viscosity values up to 0.3 GPa at 40 °C. At higher pressures, where the viscosity increases by three orders of magnitude, EMD became unreliable. This matches observations of other authors [62] that EMD simulations are known to have a limited regime of applicability and should be used for liquids that have relatively low viscosity.

It is interesting to consider whether longer simulations could extend the pressure range

over which EMD-GK could be applied. In this case, running simulations for longer times (more than 40 ns, for our study) is not going to help if the autocorrelation time doesn't change (which is in essence the upper limit of the integral of the ACF). Longer autocorrelation times could extend the EMD-GK pressure range but on the condition that the computational cost is reasonable, and that precision is maintained in the long run. For example, it would require performing autocorrelation for intervals perhaps in the range of 400+ ns which is very expensive, given the fact that time-independence is also needed to prove convergence. That would mean running a simulation of multiple 400+ ns, and rounding errors and noise would accumulate in the long run. Finally, the effect of one very long trajectory or multiple replicas would further increase the computational cost, as multiple replicas would also be needed.

To summarise, high relaxation times, due to high pressures and viscosities, hinder the decay of the ACF and thus, EMD simulations cannot capture viscosity accurately. This means that the upper limit of the integral of the ACF should be chosen to be long enough to ensure convergence of the viscosity by exceeding the rotational relaxation time of the molecule.

Chapter 4

Idealised model: shear viscosity with bulk non-equilibrium molecular dynamics

4.1 Introduction

In this Chapter we will make use of the equations shown in section 2.2 for calculating viscosity at various operational conditions, by varying pressure, temperature and the applied shear rate. This method, known as non-equilibrium molecular dynamics (NEMD), calculates shear viscosity by its definition and is more intuitive to understand. Again, the simulation box is periodic in all three dimensions, as this was also the case for equilibrium molecular dynamics (Chapter 3). We present the advantages and discuss the limitations of this method, while comparing it with EMD-GK results. We provide the computational method that was used in order to acquire shear viscosity and how to extrapolate to zero shear rate so that a comparison can be made possible with EMD-GK.

4.2 Computational methodology for simulation of shear viscosity

4.2.1 The case of 9,10-dimethyloctadecane (PAO-2)

The non-equilibrium shear viscosity of 9,10-dimethyloctadecane was calculated with the following procedure at four selected temperatures, at 313, 343, 373 and 423 K (40, 70,

100 and 150 °C respectively), with pressure ranging from 0.1 MPa to 1.0 GPa (11 data points in total).

The final state of the previous simulation, with a volume cell of equilibrated molecules, was used as the initial configuration (equilibrated density). To improve statistics, five independent trajectories were then produced by randomizing the initial configuration. This was achieved by heating and then cooling the initial configuration through separate cycles. These heat-quench cycles [2] for simulations at 313 K were performed from 313 K to T = 315, 320, 325, 330, and 335 K respectively, during 1 ns runs in the NVT ensemble, after which the systems were immediately quenched back to 313 K during another 1 ns run in the NVT ensemble. Simulations at 373 K included heat-quench cycles that were from 373 K to T = 375, 380, 385, 390 K, and 395 K respectively, during 1 ns runs in the NVT ensemble, after which the systems were immediately quenched back to 373 K during another 1 ns run in the NVT ensemble. For the remaining two temperatures (343 and 423 K case), the heat-quench cycles were the following. Simulations at 343 K included heat-quench cycles that were from 343 K to T = 345, 350, 355, 360 K, and 365 K respectively, during 1 ns runs in the NVT ensemble, after which the systems were immediately quenched back to 343 K during another 1 ns run in the NVT ensemble. Simulations at 423 K included heat-quench cycles that were from 423 K to T = 425, 430, 435, 440 K, and 445 K respectively, during 1 ns runs in the NVT ensemble, after which the systems were immediately quenched back to 423 K during another 1 ns run in the NVT ensemble. The simulation settings were the same as the EMD case (zero shear) of 9,10-dimethyloctadecane. Then, for five different values of applied shear rate (from $10^{6.5}$ up to $10^{8.5}$ s^{-1}), the p-SLLOD algorithm was used and the simulation box was deformed across the xy plane, achieving simple Couette flow. The system was sheared for 20 ns to ensure a steady state, followed by a production run of 40 ns, and the non-equilibrium viscosity was calculated for each shear rate and trajectory. The whole simulation ran in the NVT ensemble with a Nosé-Hoover thermostat and a time constant of 0.01 ps. The same procedure was repeated for

all different pressure values.

4.2.2 The case of *n*-hexadecane

The non-equilibrium shear viscosity of *n*-hexadecane was calculated with the following procedure. Starting again from the state of equilibrated density (after a 20 ns run in the NPT ensemble), five independent trajectories were produced by separate heat-quench cycles. These were from 300 K to T = 305, 310, 315, 320 and 325 K, respectively, during 1 ns runs in the NVT ensemble, after which the systems were immediately quenched back to 300 K during another 1 ns run in the NVT ensemble. The simulation settings were the same as the NEMD case of 9,10-dimethyloctadecane that was described in 4.2.1. Then, for a variety of shear rates, as can be seen in Table 4.1, the *p*-SLLOD algorithm was performed and the simulation box was deformed across the *xy* plane, achieving simple Couette flow. The system was sheared for 20 ns to ensure a steady state, followed by a production run of 40 ns, and the non-equilibrium viscosity was calculated for each shear rate and trajectory. The whole simulation ran in the NVT ensemble with a thermostat time constant of 0.01 ps. For more information about the averaging of shear viscosity in NEMD see Appendix B that includes our in-house C code that was developed to perform such task.

Table 4.1: Shear rates of *n*-hexadecane NEMD simulations.

Shear rate $\dot{\gamma}$ **(s^{-1})**	$\log(\dot{\gamma}[\mathrm{s}^{-1}])$
1.000E+08	8.00
1.259E+08	8.10
1.585E+08	8.20
1.995E+08	8.30
2.512E+08	8.40
3.162E+08	8.50
3.981E+08	8.60
5.012E+08	8.70
6.310E+08	8.80
7.943E+08	8.90
1.000E+09	9.00
1.259E+09	9.10
1.585E+09	9.20
1.995E+09	9.30
2.512E+09	9.40
3.162E+09	9.50
5.623E+09	9.75
1.000E+10	10.00
1.778E+10	10.25
3.162E+10	10.50
1.000E+11	11.00
3.162E+11	11.50
1.000E+12	12.00
3.162E+12	12.50

The zero shear viscosity was then calculated by zero shear extrapolation using the Carreau-Yasuda model [96] for viscosity of a non-Newtonian fluid:

$$\eta(\dot{\gamma}) = \eta_\infty + (\eta_0 - \eta_\infty)\Big[1 + (\dot{\gamma}\tau)^a\Big]^{\frac{n-1}{a}} \tag{4.1}$$

Where $\dot{\gamma}$ is the applied shear rate (s^{-1}), η_∞ is shear viscosity at infinite shear rate (mPa s), η_0 is shear viscosity at zero shear rate (mPa s), τ is the characteristic relaxation time (s), a and n are power indexes. Then, $1/\tau$ is the critical shear rate at which viscosity begins

to decrease. The power-law slope is (n-1) and the parameter a represents the width of the transition region between η_0 and the power-law region. The best line of fit is determined by finding parameters such that the sum of squared errors is minimised.

4.3 Force field parameters used in this study with NEMD

For the case of L-OPLS-AA, the force field parameters that were used for the simulations with 9,10-dimethyloctadecane are mentioned in 3.3.

The following tables (Table 4.2 - 4.5) show the GAFF2-AA parameters used in this work:

Table 4.2: Bonding parameters 9,10-dimethyloctadecane GAFF2-AA.

Parameter	**Value** ($\frac{\textbf{kcal}}{\textbf{mol}\text{Å}^2$)	**Type**	r_0 **(Å)**
k_1^{bond}	232.52	C-C	1.538
k_2^{bond}	375.92	C-H	1.097

Table 4.3: Angle parameters 9,10-dimethyloctadecane GAFF2-AA.

Parameter	**Value** ($\frac{\textbf{kcal}}{\textbf{mol rad}^2}$)	**Type**	θ_0 **(deg)**
k_1^{angle}	64.888	C-Ĉ-C	111.51
k_2^{angle}	38.960	H-Ĉ-H	107.58
k_3^{angle}	46.816	C-Ĉ-H	109.80

Table 4.4: Dihedral parameters 9,10-dimethyloctadecane GAFF2-AA.

C-C-C-C torsion, m=3					
Parameter	**Value (kcal/mol)**	**Parameter**	**Value**	**Parameter**	**Value (deg)**
k_1^{dihe}	0.13	n_1	3	δ_1	0.0
k_2^{dihe}	0.29	n_2	2	δ_2	180.0
k_3^{dihe}	0.11	n_3	1	δ_3	0.0
C-C-C-H torsion, m=1					
Parameter	**Value (kcal/mol)**	**Parameter**	**Value**	**Parameter**	**Value (deg)**
k_1^{dihe}	0.08	n_1	3	δ_1	0.0
H-C-C-H torsion, m=1					
Parameter	**Value (kcal/mol)**	**Parameter**	**Value**	**Parameter**	**Value (deg)**
k_1^{dihe}	0.12	n_1	3	δ_1	0.0

Table 4.5: Non-bonded parameters 9,10-dimethyloctadecane GAFF2-AA.

Atom	**ϵ (kcal/mol)**	**σ (Å)**
C	0.1078	3.39770953124
H	0.0208	2.60017699876

For GAFF2-AA the atomic charges were calculated with the semi-empirical Austin Model 1 - Bond Charge Corrections (AM1-BCC) model [97]. The following table (Table 4.6) shows the charges of the 9,10-dimethyloctadecane molecule.

Table 4.6: Atomic charges of 9,10-dimethyloctadecane with GAFF2-AA.

Atom	q (e)	**Atom**	q (e)
C_1	-0.0607	H_{12}	0.033033
C_2	-0.0607	H_{13}	0.033033
C_3	-0.0744	H_{14}	0.033033
C_4	-0.0744	H_{15}	0.033033
C_5	-0.0774	H_{16}	0.033033
C_6	-0.0774	H_{17}	0.0412
C_7	-0.0901	H_{18}	0.0412
C_8	-0.0901	H_{19}	0.0412
C_9	-0.0814	H_{20}	0.0412
C_{10}	-0.0814	H_{21}	0.0387
C_{11}	-0.0794	H_{22}	0.0387
C_{12}	-0.0794	H_{23}	0.0387
C_{13}	-0.0804	H_{24}	0.0387
C_{14}	-0.0804	H_{25}	0.0397
C_{15}	-0.0794	H_{26}	0.0397
C_{16}	-0.0794	H_{27}	0.0397
C_{17}	-0.0804	H_{28}	0.0397
C_{18}	-0.0804	H_{29}	0.0397
C_{19}	-0.0921	H_{30}	0.0397
C_{20}	-0.0921	H_{31}	0.0397
H_1	0.0477	H_{32}	0.0397
H_2	0.0477	H_{33}	0.0382
H_3	0.0387	H_{34}	0.0382
H_4	0.0387	H_{35}	0.0382
H_5	0.0387	H_{36}	0.0382
H_6	0.0387	H_{37}	0.0327
H_7	0.0387	H_{38}	0.0327
H_8	0.0387	H_{39}	0.0327
H_9	0.0387	H_{40}	0.0327
H_{10}	0.0387	H_{41}	0.0327
H_{11}	0.033033	H_{42}	0.0327

The above atoms form the following bonds: C_1-C_2, C_1-C_3, C_1-C_7, C_2-C_4, C_2-C_8, C_4-C_6, C_6-C_{10}, C_{10}-C_{12}, C_{12}-C_{14}, C_{14}-C_{16}, C_{16}-C_{18}, C_{18}-C_{20}, C_3-C_5, C_5-C_9, C_9-C_{11}, C_{11}-C_{13}, C_{13}-C_{15}, C_{15}-C_{17}, C_{17}-C_{19}, C_1-H_1, C_3-H_3, C_3-H_4, C_5-H_7, C_5-H_8, C_9-H_{17}, C_9-

H_{18}, C_{11}-H_{21}, C_{11}-H_{22}, C_{13}-H_{25}, C_{13}-H_{26}, C_{15}-H_{29}, C_{15}-H_{30}, C_{17}-H_{33}, C_{17}-H_{34}, C_{19}-H_{37}, C_{19}-H_{38}, C_{19}-H_{39}, C_7-H_{11}, C_7-H_{12}, C_7-H_{13}, C_2-H_2, C_8-H_{14}, C_8-H_{15}, C_8-H_{16}, C_4-H_5, C_4-H_6, C_6-H_9, C_6-H_{10}, C_{10}-H_{19}, C_{10}-H_{20}, C_{12}-H_{23}, C_{12}-H_{24}, C_{14}-H_{27}, C_{14}-H_{28}, C_{16}-H_{31}, C_{16}-H_{32}, C_{18}-H_{35}, C_{18}-H_{36}, C_{20}-H_{40}, C_{20}-H_{41} and C_{20}-H_{42}.

4.4 Analysis of results and comparison of NEMD with EMD-GK

4.4.1 Results for 9,10-dimethyloctadecane

For the NEMD case, viscosity was acquired successfully for pressures up to 1.0 GPa and the applied shear rates varied from $10^{6.5}$ up to $10^{8.5}$ s^{-1}. The selected shear rates in this work can be directly linked to the accessible shear rates in tribological experiments of rolling-sliding contact, where the shear rate is typically 10^5 to 10^7 s^{-1} [98], while high-performance engine components can extend up to 10^8 s^{-1} [99]. Figure 4.1 shows the viscosity obtained from the simulations as a function of the applied shear rate over the pressure range of 0.1 MPa to 1.0 GPa at 40 °C, illustrating how the critical shear rate (onset of shear thinning [100], which has been similarly observed for an ionic liquid [101]) changes with pressure. For example, at 0.8 GPa (with L-OPLS-AA), shear thinning behaviour was observed at higher shear rates ($\dot{\gamma} > 10^7$ s^{-1}) and the Newtonian regime was captured at $\dot{\gamma} < 10^7$ s^{-1}. It was found that the simulated low shear viscosity, which was calculated with eq. 2.25, was very close with the experimental value at the specified pressure, but simulation data were also fitted to the Powell-Eyring equation (black dashed line, eq. 2.38) and the zero shear viscosity was acquired with zero shear rate extrapolation. For pressures up to 0.7 GPa, the simulated shear rates were low enough to reach the Newtonian regime at shear rates ($\dot{\gamma}$) ranging from 10^7 s^{-1} up to $10^{8.5}$ s^{-1}. For these pressures, viscosity was obtained directly from an average over points in the Newtonian plateau, a procedure that has been also used in similar studies [27, 28]. For the remaining high pressure NEMD simulations (up to 1.0 GPa), viscosity was obtained by zero shear

rate extrapolation of Powell-Eyring fits (eq. 2.38) to simulation data. The parameters that were used for the fits to the Powell-Eyring equation in Figure 4.1 (40 °C case) and the other three tested temperatures are given in Table 4.7. The Powell-Eyring equation fitted very well the high pressure viscosity data acquired from MD simulations, as demonstrated by the low root mean square error (RMSE). Another observation was that the standard deviation of the NEMD viscosity results increases as shear rate decreases. For example, at 0.4 GPa and 40 °C the standard deviation of viscosity (five independent trajectories) with L-OPLS-AA at shear rates of 10^8, $10^{7.5}$ and 10^7 s^{-1} was equal to $\pm$ 5.1, $\pm$ 37.1 and $\pm$ 76.7 mPa s respectively. This is a typical behaviour in NEMD simulations as at lower shear rates, the systematic non-equilibrium response becomes comparable to the equilibrium fluctuations. This leads to a lower signal-to-noise ratio and an increase of viscosity variability [3].

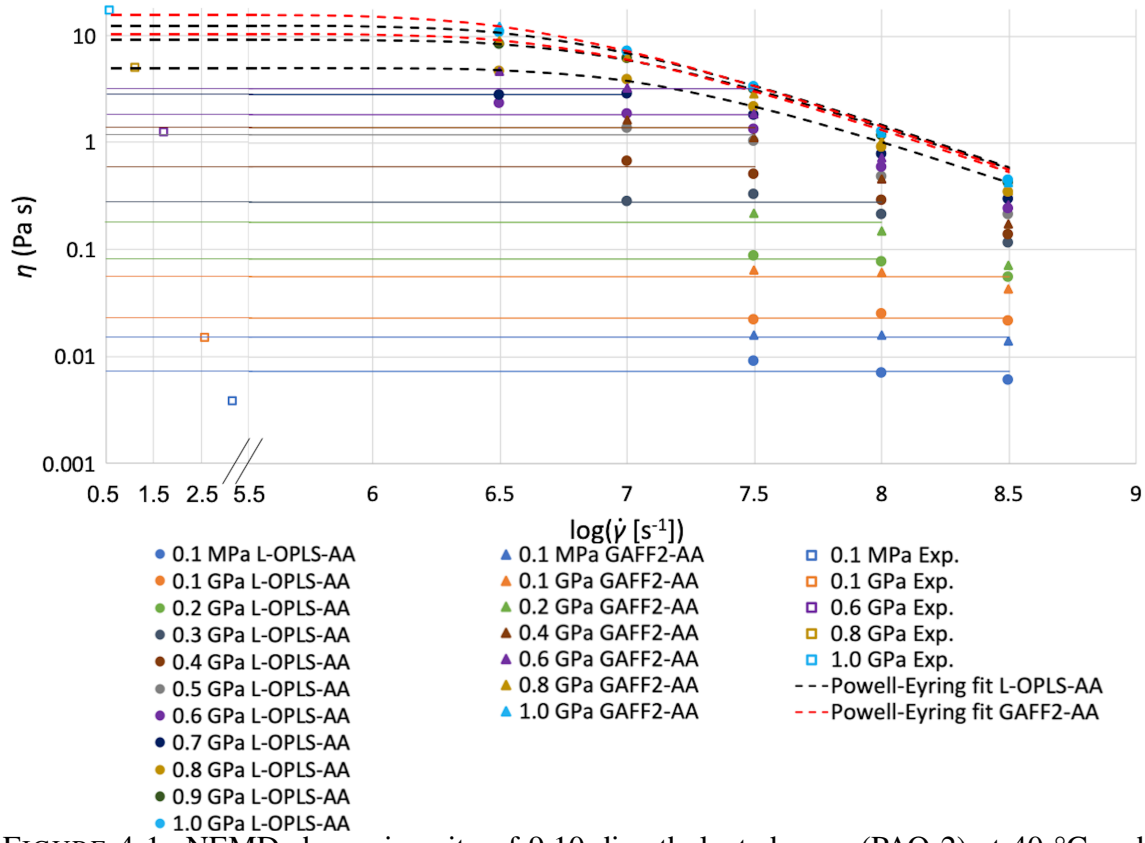

FIGURE 4.1: NEMD shear viscosity of 9,10-dimethyloctadecane (PAO-2) at 40 °C and pressures from 0.1 MPa to 1.0 GPa. Experimental data were acquired by averaging viscosity measurements from two different viscometers. One of the viscosity data set used in the averaging has been previously published [102]. Each simulation data point represents the average viscosity value of five independent simulations, at each shear rate. Circles indicate viscosity results by using the L-OPLS-AA force field, while triangles indicate results acquired with the GAFF2-AA force field. Squares indicate experimental viscosity values. Horizontal solid lines indicate the average viscosity obtained for pressures where the applied shear rates had reached the Newtonian regime. The dashed lines indicate Powell-Eyring fits (eq. 2.38) to MD simulation data, that extrapolate to zero shear rate (Newtonian limit). The black dashed line corresponds to the L-OPLS-AA force field and the red dashed line corresponds to the GAFF2-AA force field. The parameters that were used for the fits are given in Table 4.7.

Table 4.7: Parameters with the root mean square error (RMSE) used in the Powell-Eyring fits (eq. 2.38) for the MD data in Figure 4.1 (40 °C case) and the other three tested temperatures. The root mean square errors are between simulation data and the Powell-Eyring approximations.

Force Field	P (GPa)	η_N (Pa s)	τ (s)	η_∞ (Pa s)	RMSE (Pa s)	T (°C)
L-OPLS-AA	0.8	4.99	1.74×10^{-7}	0	0.10	40
L-OPLS-AA	0.9	9.36	2.63×10^{-7}	0	0.14	40
L-OPLS-AA	1.0	12.59	3.61×10^{-7}	0	0.14	40
GAFF2-AA	0.8	10.46	3.35×10^{-7}	0	0.21	40
GAFF2-AA	1.0	15.71	5.01×10^{-7}	0	0.12	40
L-OPLS-AA	0.8	1.94	8.77×10^{-8}	0	0.04	70
L-OPLS-AA	0.9	3.58	1.38×10^{-7}	0	0.04	70
L-OPLS-AA	1.0	4.09	1.42×10^{-7}	0	0.09	70
L-OPLS-AA	0.8	0.61	3.58×10^{-8}	0	0.001	100
L-OPLS-AA	0.9	1.05	5.21×10^{-8}	0	0.01	100
L-OPLS-AA	1.0	1.80	6.97×10^{-8}	0	0.05	100
L-OPLS-AA	0.8	0.12	6.67×10^{-9}	0	0.01	150
L-OPLS-AA	0.9	0.17	9.36×10^{-9}	0	0.01	150
L-OPLS-AA	1.0	0.26	1.47×10^{-8}	0.01	0.01	150

Figure 4.2 shows the zero shear viscosity-pressure relation of 9,10-dimethyloctadecane, in which we are comparing two methods (EMD and NEMD) and two force fields (L-OPLS-AA and GAFF2-AA) with experimental data for the pressure range of 0.1 MPa up to 1.0 GPa at 40 °C, where viscosity has a huge variation. For EMD simulations, we observed good agreement for viscosity values up to 0.3 GPa. Simulations started to diverge from experiment at higher pressures where EMD is no longer suitable, due to the exponential increase of viscosity and the very long rotational relaxation times of the less flexible molecules of larger size [103]. The rotational relaxation time refers to the required time for molecular chains to reach equilibrium after an external perturbation. In the Green-Kubo method, errors accumulate at long times (due to statistical noise) and as result, this is not something that can be remedied simply by using longer trajectories [12, 103]. The time

decomposition method [12] may help to some degree, as recently demonstrated for 2,2,4-trimethylhexane up to viscosities of 20 mPa s [104] and for a binary mixture of methylcyclohexane and 1-methylnaphthalene up to viscosities of 50 mPa s [20]. However, at higher viscosites, NEMD with extrapolation back to the Newtonian viscosity (using the Eyring equation) seems to be the only reliable method (this study and [27–29]). An important observation is that the region where EMD fails to predict the exponential increase of viscosity (compared to the experiment at $P > 0.3$ GPa) in this study, corresponds to literature suggestions [62] that NEMD is preferable to EMD for viscosity calculations of high-viscosity materials (above 20-50 mPa s). On the other hand, NEMD simulations performed much better and were able to capture high pressure viscosity successfully, although they tended to slightly overestimate viscosity at low pressures, where EMD performed slightly better. As can also be seen from the graph, the L-OPLS-AA force field was more accurate than the GAFF2-AA force field, with the L-OPLS-AA force field overestimating viscosity by only 2% at a pressure of 0.8 GPa. This could be due to the fact that GAFF2-AA is a general-purpose force field, while L-OPLS-AA is specifically designed for long-chain hydrocarbons.

Figure 4.3 shows the effect of temperature on the viscosity-pressure relation of 9,10-dimethyloctadecane, in which we are comparing viscosity results acquired from NEMD simulations (using the L-OPLS-AA force field) and experimental data for the pressure range of 0.1 MPa up to 1.0 GPa. The general tendency is that viscosity is slightly overestimated by NEMD simulations, nonetheless, simulations successfully capture the pressure-viscosity slope, which is equal to the reciprocal asymptotic isoviscous pressure coefficient. We need to note that the experimental PAO-2 sample was not pure 9,10-dimethyloctadecane as used in the simulations, though it contained more than 95% of hydrogenated 1-decene dimer by weight [36]. This may be a source of some of the deviations between simulations and experiment.

The pressure–viscosity response of lubricants is commonly represented using the McEwen

equation [105]:

$$\eta(P) = \eta_0 \left(1 + \frac{\alpha^* P}{q-1}\right)^q \tag{4.2}$$

Where η_0 is the low-shear viscosity at reference (ambient) pressure, α^* is the reciprocal asymptotic isoviscous pressure coefficient and q is the McEwen exponent. This is equivalent to the Tait pressure–viscosity equation [106] for low (ambient [102]) reference pressures. The parameters that were used for the fits to the McEwen equation in Figure 4.2 and 4.3 are given in Table 4.8.

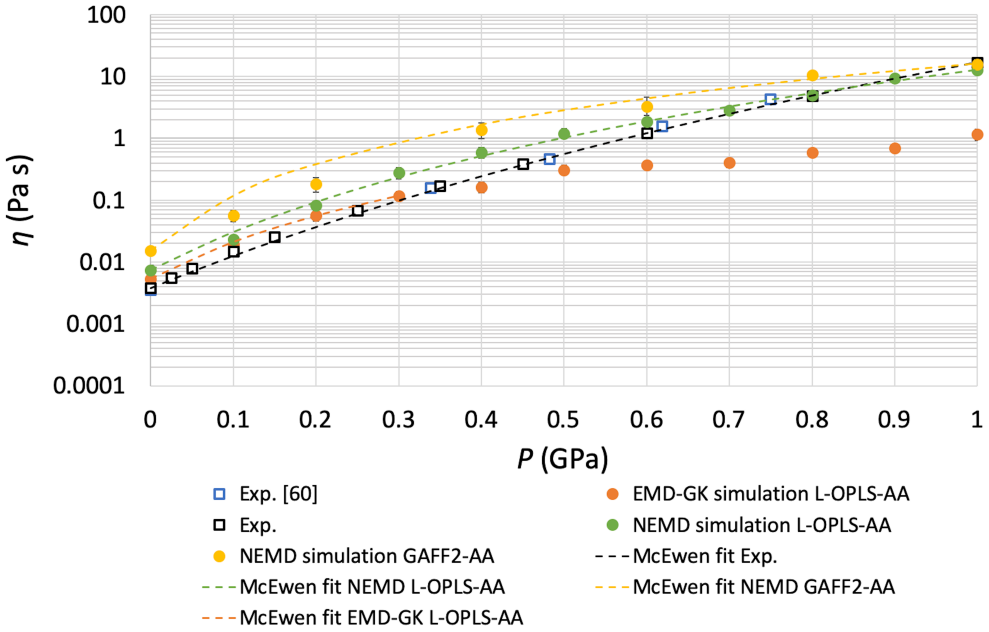

FIGURE 4.2: Zero shear viscosity simulation of 9,10-dimethyloctadecane (PAO-2) at 40 °C, with pressures ranging from 0.1 MPa to 1.0 GPa. Experimental data were acquired by averaging viscosity measurements from two different viscometers. One of the viscosity data set used in the averaging has been previously published [102] and experimental data are also provided by [92]. Squares indicate experimental viscosity values and circles indicate viscosity results from MD simulations. Statistical error bars are shown when they are larger than the symbol size. For $P \leqslant 0.7$ GPa simulations reached the Newtonian limit without extrapolation, while for $P \geqslant 0.8$ GPa, zero shear viscosity was extrapolated by Powell-Eyring fits (eq. 2.38) to simulation data. The dashed lines indicate McEwen fits (eq. 4.2) to the experimental and MD simulation data. The parameters that were used for the fits are given in Table 4.8.

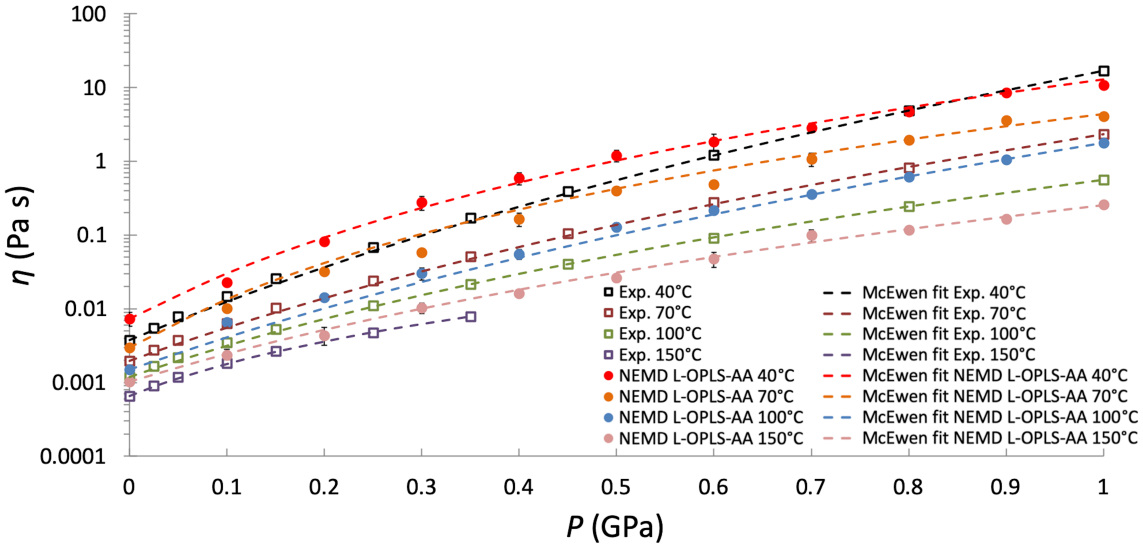

FIGURE 4.3: Zero shear viscosity simulation of 9,10-dimethyloctadecane (PAO-2) at 40, 70, 100 and 150 °C, with pressures ranging from 0.1 MPa to 1.0 GPa. Squares indicate experimental viscosity values that were acquired by averaging viscosity measurements from two different viscometers. Circles indicate viscosity results by using the L-OPLS-AA force field. Statistical error bars are shown when they are larger than the symbol size. For $P \leqslant 0.7$ GPa simulations reached the Newtonian limit without extrapolation, while for $P \geqslant 0.8$ GPa, zero shear viscosity was extrapolated by Powell-Eyring fits (eq. 2.38) to simulation data. The dashed lines indicate McEwen fits (eq. 4.2) to the experimental and MD simulation data. The parameters that were used for the fits are given in Table 4.8.

In their region of applicability, which was up to 0.3 GPa for EMD-GK and up to 1.0 GPa for NEMD, the values of α^* for both EMD-GK and NEMD methods were in reasonable agreement with experiment when the L-OPLS-AA force field was used. For example, at 40 °C the value of α^* was overestimated by 15% with NEMD and by only 3% with EMD-GK when comparing to experiment. At higher temperatures (100 and 150 °C) NEMD was in good agreement with experiment as the overestimation was only 7% and 6% respectively. At the medium temperature of 70 °C NEMD overestimated the value of α^* by 44%.

Table 4.8: Parameters with the root mean square error (RMSE) used in the McEwen fits (eq. 4.2) for the MD and experimental data in Figure 4.2 and 4.3. The root mean square errors are between simulation/experimental data and the McEwen approximations.

Method	η_0 (mPa s)	α^* (GPa^{-1})	q	RMSE (mPa s)	T (°C)
Exp.	3.80	11.49	10.95	11.10	40
NEMD L-OPLS-AA	7.38	13.17	5.38	334	40
NEMD GAFF2-AA	15.21	19.31	2.87	713	40
EMD-GK L-OPLS-AA	5.32	11.88	3.39	0.85	40
Exp.	1.98	9.70	8.56	6.94	70
NEMD L-OPLS-AA	2.99	13.95	4.60	222	70
Exp.	1.20	8.83	6.19	0.40	100
NEMD L-OPLS-AA	1.51	9.45	9.33	13.95	100
Exp.	0.66	7.26	2.43	0.04	150
NEMD L-OPLS-AA	1.03	7.71	5.62	7.38	150

Figure 4.4 shows the velocity profile of a NEMD simulation, at a chosen shear rate of 10^8 s^{-1} for 9,10-dimethyloctadecane at ambient (0.1 MPa) and elevated pressures (0.5 and 1.0 GPa). The simulation box (across y) is divided into twenty equally spaced regions. Then, the velocity vector component (x-dimension) of atoms that exist in each region at a particular timestep is averaged, and then averaged again over different time intervals every 5 ps, to improve statistics during the 40 ns production run. The resulting velocity profile is linear, as described in simple Couette flow. To maintain the same shear rate in simulations at different pressures, the applied velocity at the top edge of the simulation box has to be adjusted accordingly, so as to take into account the volume change arising from each applied pressure. This difference can be seen near the top edge (relative gap thickness = 1), where the lowest pressure (0.1 MPa) results in the largest simulation box, thus requiring a slightly higher velocity. Additionally, instead of equally spaced regions but in terms of actual distances, where the centre of the simulation box is taken as reference point, the behaviour is similar and can be seen in Figure 4.5.

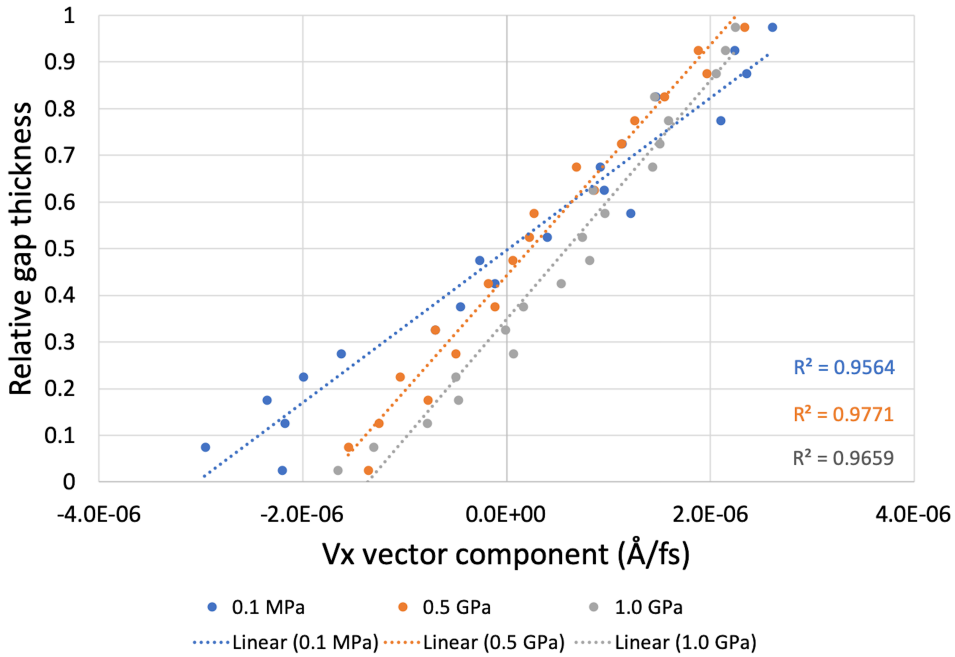

FIGURE 4.4: Velocity profile example of 9,10-dimethyloctadecane at 40 °C, with $\dot{\gamma}$ equal to 10^8 s^{-1}, at three different pressure values, 0.1 MPa, 0.5 GPa and 1.0 GPa.

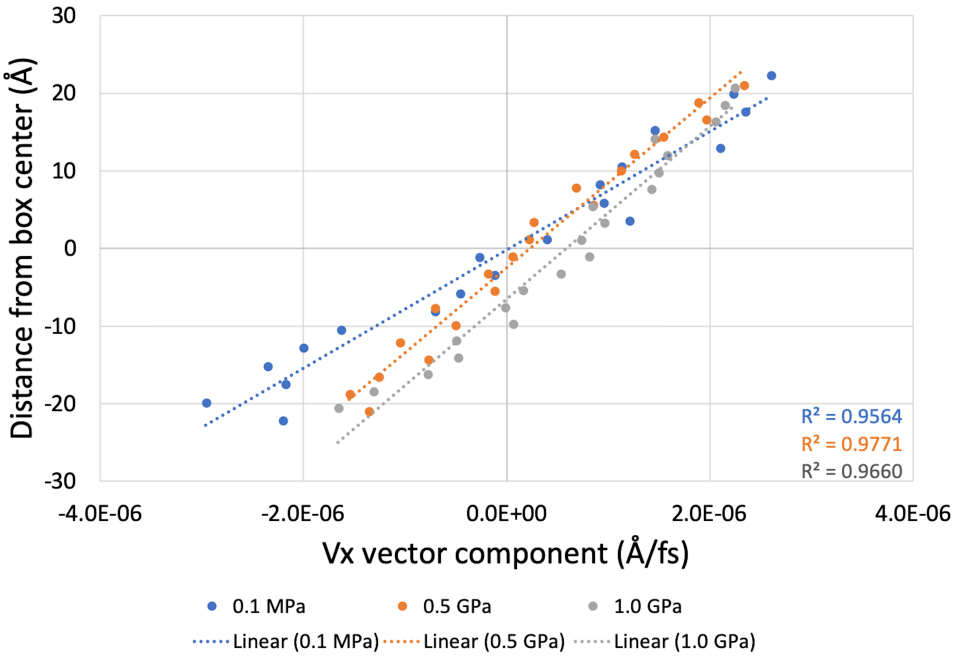

FIGURE 4.5: Velocity profile example of 9,10-dimethyloctadecane at 40 °C, with $\dot{\gamma}$ equal to 10^8 s^{-1}, at three different pressure values, 0.1 MPa, 0.5 GPa and 1.0 GPa. At each pressure, the centre of the simulation box is taken as reference point.

To give an estimate of the computational cost of this work, considering the case of 0.5 GPa at 40 °C and an applied shear rate of 10^8 s^{-1} (for the NEMD case), the following results are representative. The density equilibration and viscosity calculation with EMD-GK (62 ns simulation time in total) required 6117 Core Hours (CPU-h) for one independent trajectory. On the other side, the density equilibration and viscosity calculation with NEMD (82 ns simulation time in total) required 7938 Core Hours (CPU-h) for one independent trajectory.

4.4.2 Results for *n*-hexadecane

For the case of *n*-hexadecane, the non-equilibrium viscosity average for various shear rates can be seen in Figure 4.6, with standard deviation error bars at each data point. Figure 4.7 shows the same results in a logarithmic scale for viscosity, with a Carreau-Yasuda (CY) model fit. Extrapolation to zero shear rate leaded to a result, very close to the zero shear viscosity calculated by EMD, as the CY fit overpredicted viscosity by only 2% when compared to EMD . From these figures, the following can be said. The lower the shear rate, the greater the standard deviation. Then, running simulations for longer time, results in a better viscosity estimate due to better averaging of $\langle P_{xy} \rangle$. Also, for lower shear rates, viscosity estimates converge slower compared to viscosities at higher shear rates. Finally, the NEMD simulation captured a Newtonian plateau for viscosity, followed by a shear thinning region.

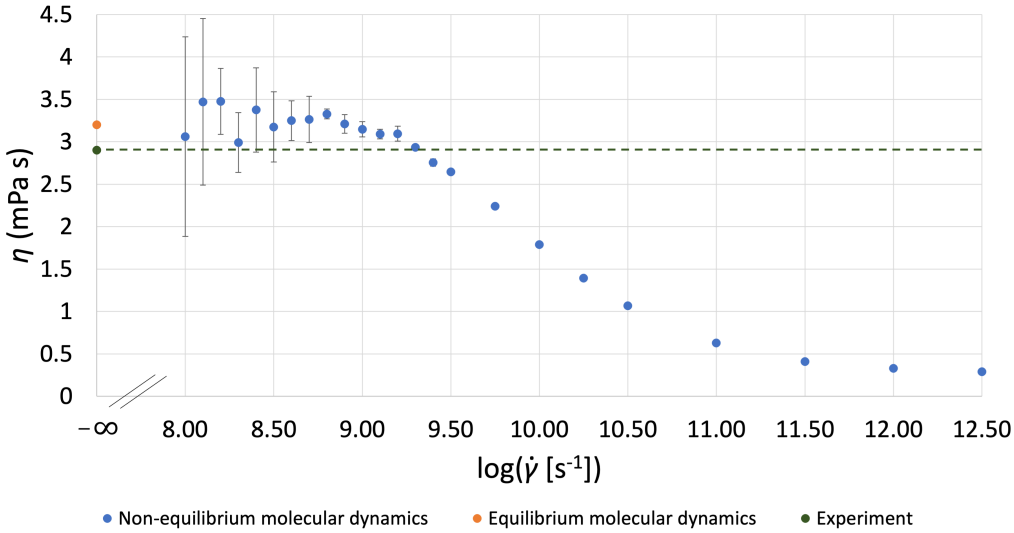

FIGURE 4.6: NEMD simulation of *n*-hexadecane at 300 K (27 °C), 1 atm (0.1 MPa). Each data point is the average value of 5 replicas (40 ns run). Statistical error bars are shown when they are larger than the symbol size.

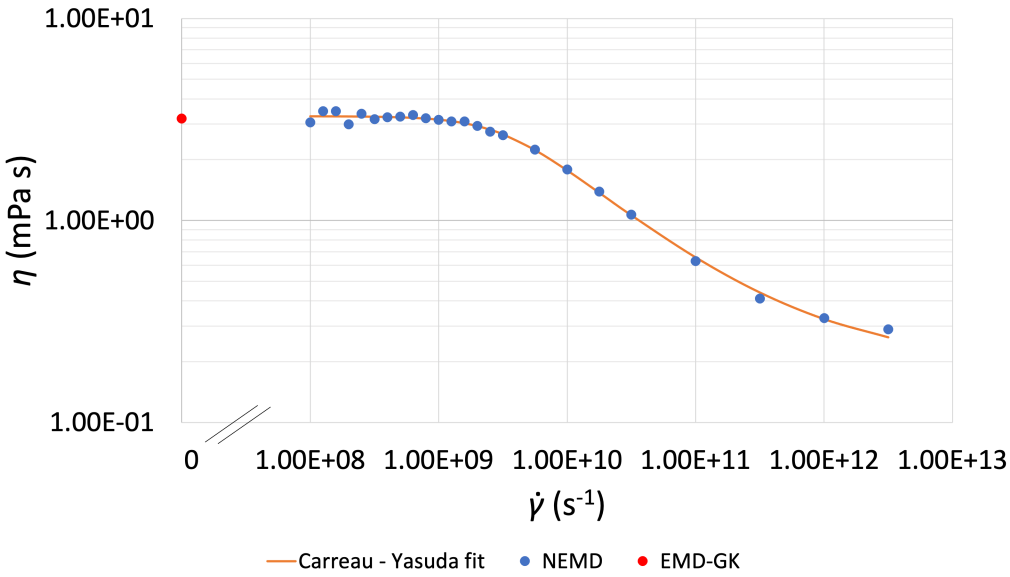

FIGURE 4.7: NEMD simulation of *n*-hexadecane's viscosity as a function of shear rate at 300 K (27 °C), 1 atm (0.1 MPa), with a log scale and a Carreau-Yasuda model fit.

Table 4.9: Viscosity results for NEMD simulations of *n*-hexadecane and comparison with EMD and literature [6]. The subscript next to the symbols denotes degrees in Celsius.

Molecule	d_{27} **(g/ml)**	η_{27} **NEMD CY fit (mPa s)**	η_{27} **EMD (mPa s)**	η_{27} **exp. (mPa s)**
n-hexadecane	0.77 ± 0.005	3.3	3.2 ± 0.03	2.9

4.5 Summary

In this Chapter we studied the use of non-equilibrium molecular dynamics (NEMD) for calculating shear viscosity of several lubricants, including *n*-hexadecane and 9,10-dimethyloctadecane at different temperatures, pressures and shear rates. It was demonstrated that NEMD simulations successfully capture zero shear viscosity (after extrapolation to zero shear rate), which was validated against experimental values. As a result, NEMD is suggested to be the method of choice in these operational conditions. We conclude that NEMD can be used to obtain atomic-level insights of lubricant interactions, while providing a reliable approach for computing viscosity, especially in cases where experimental measurement can be difficult.

For the case of 9,10-dimethyloctadecane, we found that the L-OPLS-AA force field, which is specifically designed for long-chain hydrocarbons, achieves markedly better agreement with experimental viscosity values than GAFF2-AA, as the L-OPLS-AA force field overestimated viscosity by only 2% at a pressure of 0.8 GPa (40 °C case) while GAFF2-AA was over by a dramatic 114%. Running simulations either for longer time periods, or multiple repeats, allowed us to obtain results with a lower standard deviation of viscosity, which was more noticeable at lower shear rates ($\dot{\gamma} < 10^7$ s^{-1}) and pressures ($P < 0.5$ GPa) with NEMD simulations.

Additionally, we found that in their region of applicability, the values of the reciprocal asymptotic isoviscous pressure coefficient for both EMD-GK and NEMD methods were

in reasonable agreement with experiment when the L-OPLS-AA force field was used. By choosing this force field, we expect that the methods used in this study can be applied to similar lubricants at various temperatures and pressures.

Chapter 5

Realistic model: shear viscosity with confined non-equilibrium molecular dynamics

5.1 Introduction

In this Chapter we will make use of the equations shown in section 2.3.2 for calculating viscosity at various operational conditions, by varying pressure, the applied shear rate and the film thickness of the confined lubricant. This method calculates shear viscosity by its definition and is more intuitive to understand. This time, the simulation box is periodic in the x and y-dimension and non-periodic in the z-dimension. We present the advantages and discuss the limitations of this method, while comparing with NEMD results. We provide the computational method that was used in order to acquire shear viscosity and we present in high detail the process for properly thermostating the walls (iron oxide) during shearing, so that excess heat that is generated during the shearing stage is removed and we maintain the desired temperature.

5.2 Hematite structure

Crystal polymorphs are defined as substances that are chemically identical but exist in more than one crystal form. To date, eight crystalline polymorphs of Fe_2O_3 (also known

as iron(III) oxide or ferric oxide) have been described, all of which have significantly different structural and magnetic properties [107, 108]. Those are: (i) α-Fe_2O_3; (ii) β-Fe_2O_3; (iii) γ-Fe_2O_3; (iv) ε-Fe_2O_3; (v) ζ-Fe_2O_3; (vi) η-Fe_2O_3; (vii) θ-Fe_2O_3; and (viii) ι-Fe_2O_3.

From the above polymorphs, hematite (α-Fe_2O_3) is the most stable and common form of iron oxide under ambient conditions, and its (001) surface is the most stable according to DFT calculations [109]. In addition, iron oxide is known to form in tribological systems of steel under extreme pressures. For this reason it is chosen as a surface for our system. Figure 5.1 shows the hexagonal unit cell of α-Fe_2O_3.

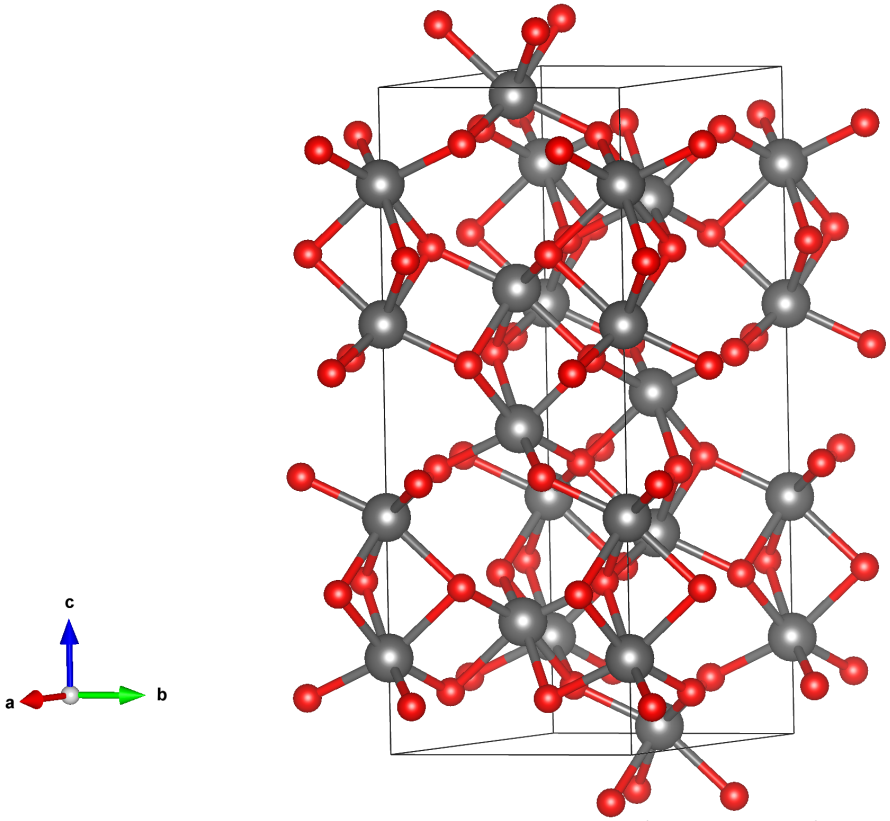

FIGURE 5.1: Unit cell of hematite α-Fe_2O_3, a = b = 5.029 Å, c = 13.73 Å, $\alpha = \beta = 90$ °, $\gamma = 120$ ° [110, 111]. Rendered with *VESTA 3* [112]. Iron atoms are coloured with silver and oxygen atoms with red.

5.3 Model set-up for confinement within hematite and calculation of viscosity

The following approach was chosen in order to set up our systems for calculating viscosity. A number of simulation parameters was varied, including pressure, applied shear rate, and film thickness. The pressure values were chosen to be in the range of the applied pressure in bulk NEMD simulations that were described in Chapter 4. These were 0.1 GPa, 0.5 GPa and 1.0 GPa. The applied shear rate was chosen so that our simulations capture the Newtonian and non-Newtonian (shear thinning) region. The values were $10^{7.5}$ and $10^{8.5}$ s^{-1}, respectively. Finally, the film thicknesses were chosen to be in a wide range of values to investigate more in-depth its effect on viscosity. To achieve that, by keeping constant the number of iron oxide molecules at the top and bottom part of the simulation domain (2,700 molecules in total), three different number of 9,10-dimethyloctadecane molecules were inserted. The number was varied to include a very thin layer of molecules (case of 100 inserted molecules - system 1), a medium-sized layer (case of 200 inserted molecules - system 2) and a layer that was meant to be approaching the bulk size that was used in NEMD simulations in Chapter 4 (case of 450 inserted molecules - system 3). For example, Figure 5.2 shows the initial simulation domain, prior to the equilibration and compression stage, for the medium-sized case of system 2. Table 5.1 summarises the simulations performed.

Two separate studies were performed. In the first case study, interactions between the fluid molecules were represented with L-OPLS-AA [39], while forces between the iron oxide and fluid atoms were governed by Lennard-Jones and electrostatic interactions. The Fe and O parameters used were those developed by Savio *et al.* [113] and Berro *et al.* [114] to study the behaviour of alkane films confined between α-Fe_2O_3 surfaces. The α-Fe_2O_3 slabs were restrained in their crystal structure using harmonic bonds with a spring constant of 130 kcal/mol [114].

For the second case study, the force field parameters for C, H, O and Fe atoms were represented with ReaxFF [115, 116], which were also used in a recent work [117] for studying the thermal decomposition of phosphate esters on ferrous surfaces. For the theoretical framework of L-OPLS-AA and ReaxFF see 1.1.3. The motivation for studying the performance of a reactive force field included our goal to investigate how a reactive force field will perform for calculating viscosity, as to our best of knowledge, such use has not been employed before for the determination of viscosity of confined lubricants at high pressures. Additionally, there is industrial interest of examining possible reactions that might occur under high pressures, between the lubricant and surfaces, so this initial model set-up, can lead to this direction. Although, due to time constrains of the project this has been left out for future research.

The three molecular systems were generated by using an in-house modified version of LAMMPS_builder [110, 111], which is an open-source program that is capable of generating confined systems for molecular dynamics simulations with LAMMPS. Also, this software assigned the force field parameters automatically when generating our systems for L-OPLS-AA. For ReaxFF, the parameters were assigned manually for compatibility with the parameter file that was taken from a previous study [117].

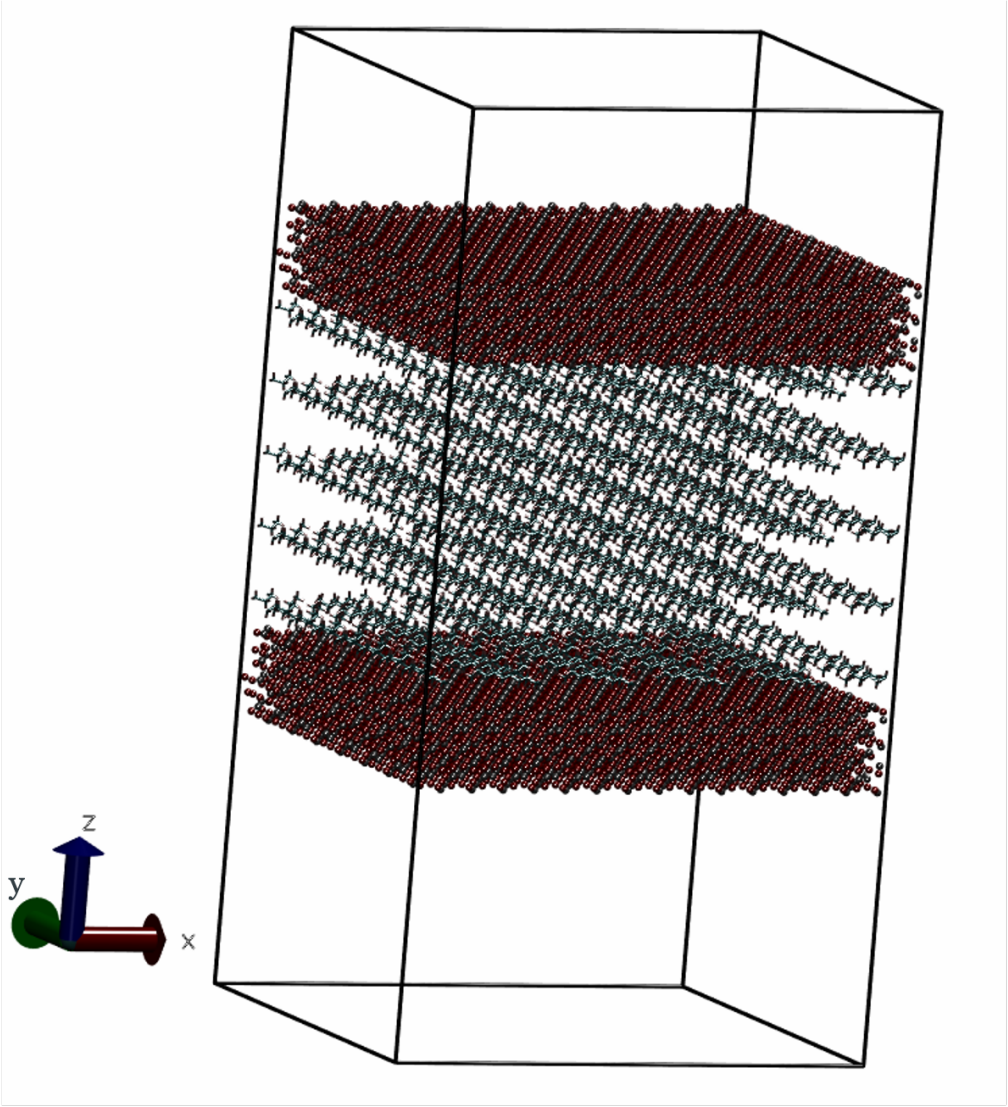

FIGURE 5.2: Initial structure of system 2 (200 lubricant molecules) before compression. The system is periodic in the x and y-dimension and non-periodic in the z-dimension. Carbon atoms are coloured with cyan, hydrogen atoms with grey, oxygen atoms with red and iron atoms with silver. For more information, see Appendix D for an example script of calculating viscosity with confined NEMD.

Table 5.1: Simulations performed for confined NEMD. Note that for each case, three independent trajectories were generated.

Lubricant molecules	**System**	**log shear rate**	**Force field**	P **(GPa)**
100	1	7.50	L-OPLS-AA	0.1
200	2	7.50	L-OPLS-AA	0.1
450	3	7.50	L-OPLS-AA	0.1
100	1	7.50	ReaxFF	0.1
200	2	7.50	ReaxFF	0.1
100	1	7.50	L-OPLS-AA	0.5
200	2	7.50	L-OPLS-AA	0.5
450	3	7.50	L-OPLS-AA	0.5
100	1	7.50	ReaxFF	0.5
200	2	7.50	ReaxFF	0.5
100	1	7.50	L-OPLS-AA	1.0
200	2	7.50	L-OPLS-AA	1.0
450	3	7.50	L-OPLS-AA	1.0
100	1	7.50	ReaxFF	1.0
200	2	7.50	ReaxFF	1.0
100	1	8.50	L-OPLS-AA	0.1
200	2	8.50	L-OPLS-AA	0.1
450	3	8.50	L-OPLS-AA	0.1
100	1	8.50	ReaxFF	0.1
200	2	8.50	ReaxFF	0.1
100	1	8.50	L-OPLS-AA	0.5
200	2	8.50	L-OPLS-AA	0.5
450	3	8.50	L-OPLS-AA	0.5
100	1	8.50	ReaxFF	0.5
200	2	8.50	ReaxFF	0.5
100	1	8.50	L-OPLS-AA	1.0
200	2	8.50	L-OPLS-AA	1.0
450	3	8.50	L-OPLS-AA	1.0
100	1	8.50	ReaxFF	1.0
200	2	8.50	ReaxFF	1.0

5.3.1 L-OPLS-AA force field

The whole simulation included three distinct steps. Those were, equilibration (reorientation), compression and the last step of shearing with equilibration and production run.

The simulation started with equilibration and molecular reorientation. This was achieved by an energy relaxation process, followed by a run of 8 ns in the microcanonical (NVE) ensemble that included a Langevin thermostat [48], which was applied to the lubricant atoms, to control temperature at 373 K (100 °C) with a time constant of 0.1 ps. The simulation timestep was set to 1 fs. To allow molecular reorientation of the lubricant, the outermost layer of iron atoms of the upper and lower iron oxide slabs was kept frozen for the whole duration of the simulation. To ensure that this process was in effect, the film thickness was monitored during the simulation, which was found to fluctuate from an average constant value due to some degree of harmonic oscillation of atoms. Then, to improve statistics, three independent trajectories were produced by randomizing the configuration. This was achieved by heating and then cooling the initial configuration through separate cycles. These heat-quench cycles [2] for simulations at 373 K were performed from 373 K to T = 375, 380 and 385 K, respectively, during 1 ns runs in the NVE ensemble, after which the systems were immediately quenched back to 373 K during another 1 ns run in the NVE ensemble.

The second step of the simulation included the application of external pressure (0.1, 0.5 and 1.0 GPa) at the outermost layer of iron atoms of the upper slab in order to compress the systems. This was achieved during 5-8 ns runs where the outermost bottom layer of the lower iron oxide slab was kept frozen for the whole duration of the simulation. The simulation ran for long enough until the film thickness reached a negligible change. Then, the film thickness values during the last 2 ns were used to determine the average film thickness value needed for the next step of shearing.

The third step of the simulation included the shearing stage where a shear rate was ap-

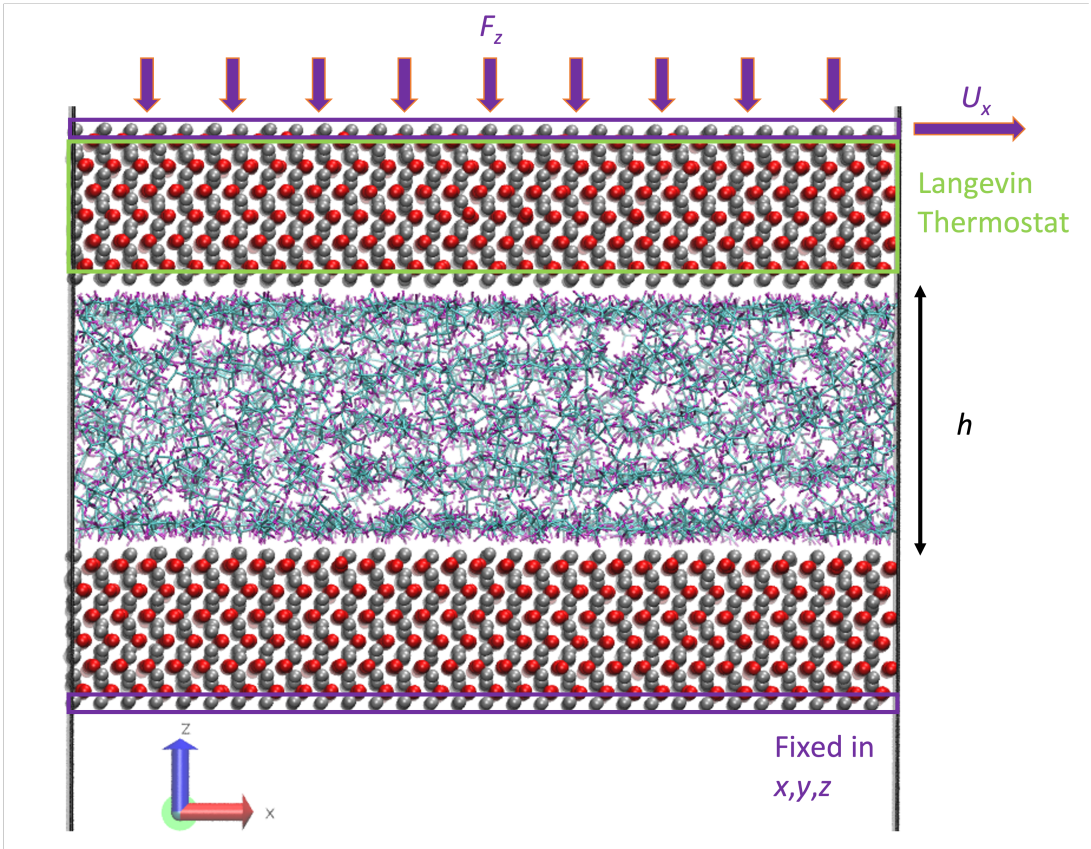

FIGURE 5.3: Illustration of the molecular snapshot of system 2 with L-OPLS-AA at 0.1 GPa and 100 °C. The green box represents the thermostating region during the shearing stage of confined NEMD and the two purple boxes represent the outermost iron layers at the top and bottom part of the simulation box. The upper purple box shows the area where the external force F_z is applied, while the purple box at the bottom represents the fixed area of iron atoms. The film thickness of the fluid is equal to h and U_x is the external constant velocity which results in an applied shear rate. Carbon atoms are coloured with cyan, hydrogen atoms with purple, oxygen atoms with red and iron atoms with silver.

plied at the system by applying an external velocity at the top outermost layer of iron atoms while continuing to apply an external pressure. At this stage, the Langevin thermostat was applied at the inner atomic layers of the upper iron oxide slab, as this is known to be a better and more realistic approach to thermostat regions in shearing systems [118], instead of applying the thermostat to the fluids, which is known to affect their dynamics [119]. Figure 5.3 illustrates the thermostating region during shearing. Again, the outermost bottom layer of the lower iron oxide slab was kept frozen for the whole duration of the simulation.

The system was then sheared for 4 ns to ensure a steady state, followed by a production run of 8-80 ns, depending on the applied conditions until viscosity converged and became time-independent for each shear rate and trajectory. Couette flow was achieved during the simulation as there was a linear velocity profile across the lubricant region.

5.3.2 ReaxFF force field

For ReaxFF, the simulation steps were the same as the L-OPLS-AA, with the only difference being the duration of the simulation, as ReaxFF is more computationally expensive than L-OPLS-AA. For this reason, system 3 (case of 450 inserted molecules) was excluded from simulations. The changes were the following.

The simulation timestep was set to 0.25 fs, which has been also used before for investigating the thermal decomposition of phosphate esters on ferrous surfaces with ReaxFF [117], while the time constant of the Langevin thermostat was set to 0.01 ps. In addition, the chosen timestep value is included in the suggested timestep range of 0.1 - 0.5 fs from literature [120], which is needed in order to produce reliable dynamics and ensure energy conservation.

Another change occurred at the first step of equilibration and molecular reorientation where the heat-quench cycles for simulations at 373 K were performed from 373 K to T = 375, 380 and 385 K, respectively. After a 0.15 ns run in the NVE ensemble, the systems were heated during 0.025 ns and then they were immediately quenched back to 373 K during another 0.025 ns run in the NVE ensemble. This process occurred two times in order to ensure molecular reorientation.

During the compression, step, the same pressures as the L-OPLS-AA case were applied, and the compression lasted for 5.8 – 7.75 ns where the outermost bottom layer of the lower iron oxide slab was kept frozen for the whole duration of the simulation. The simulation ran for long enough until the film thickness reached a negligible change. Table 5.2 shows the time duration of the simulation for each system and pressure using the

ReaxFF force field. Then, the film thickness values during the last 0.5 ns were used to determine the average film thickness value needed for the next step of shearing.

During the shearing step the same shear rates as the L-OPLS-AA case were applied, and the system was sheared for 2 ns to ensure a steady state. Again, the film thickness values during the last 0.5 ns were used to determine the average film thickness value needed for the production step of shearing.

Then, the simulation continued with a production run of 1 ns, during which viscosity was calculated for each shear rate and trajectory. Figure 5.4 illustrates the three steps for calculating viscosity.

Table 5.2: Simulation time for the case of ReaxFF, at a pressure range from 0.1 to 1.0 GPa at 100 °C. For each compression and system, three independent trajectories were used, in order to increase viscosity accuracy.

Lubricant molecules	**System**	**Simulation time (ns)**	***P*** **(GPa)**	**Trajecory**
100	1	7.75	0.1	traj_1
100	1	7.75	0.1	traj_2
100	1	7.75	0.1	traj_3
100	1	7.125	0.5	traj_1
100	1	7.125	0.5	traj_2
100	1	7.125	0.5	traj_3
100	1	7.125	1.0	traj_1
100	1	7.125	1.0	traj_2
100	1	7.125	1.0	traj_3
200	2	6.775	0.1	traj_1
200	2	6.775	0.1	traj_2
200	2	6.775	0.1	traj_3
200	2	6.3	0.5	traj_1
200	2	6.3	0.5	traj_2
200	2	6.3	0.5	traj_3
200	2	5.8	1.0	traj_1
200	2	5.8	1.0	traj_2
200	2	5.8	1.0	traj_3

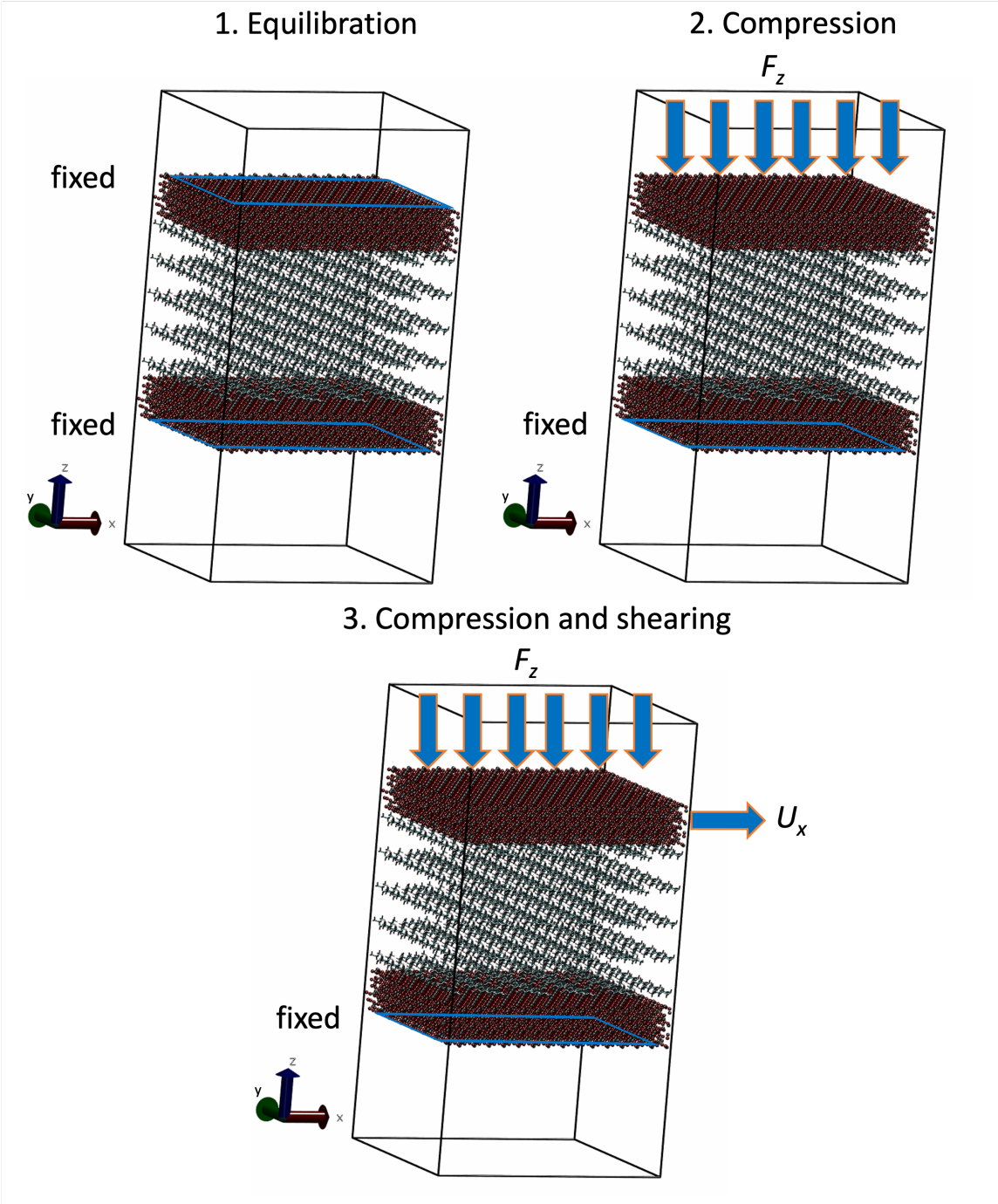

FIGURE 5.4: The three steps for calculating viscosity with confined NEMD. During the first step, both outermost layers at the top and bottom, are kept fixed (blue box), while lubricant molecules start to reorient in different directions. At the second step, the upper constrain is lifted and an external force is applied in order to compress the upper surface. During the third step, when the system is fully compressed and has a stable film thickness, a constant velocity is added U_x at the upper outermost layer of iron atoms in order to induce shearing. Carbon atoms are coloured with cyan, hydrogen atoms with grey, oxygen atoms with red and iron atoms with silver.

5.4 Analysis of results and comparison of confined NEMD with NEMD

Figure 5.5 and 5.6 show a molecular snapshot of the three systems studied after successful compression at a pressure of 0.1 GPa at 100 °C by using the L-OPLS-AA force field. As it can be seen from the illustrations, the atomic arrangement of the iron oxide surface is well-preserved as the their bonds are described by a bonded force field. On the other hand, as can be seen from Figure 5.7, which is the case of ReaxFF at a pressure of 0.1 GPa at 100 °C, the iron oxide atoms have more freedom to move as there are no explicit bonds between atoms. Interestingly, for both force fields, we can see the formation of a monolayer of lubricant molecules near the lubricant-surface interface, which has also been observed in other studies using different systems of surface and lubricants [77, 118].

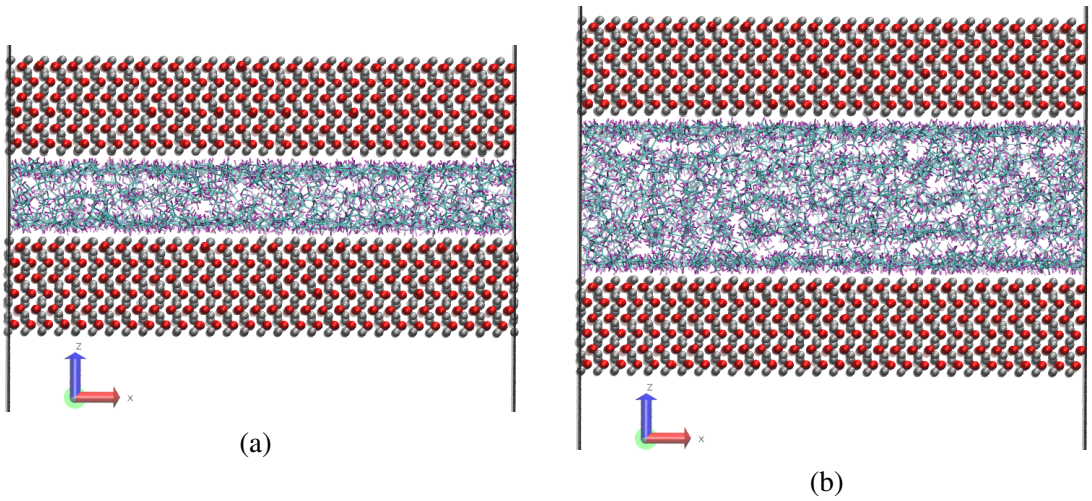

(a) (b)

FIGURE 5.5: (a) Molecular snapshot of system 1 (100 lubricant molecules), with L-OPLS-AA at 0.1 GPa and 100 °C after the compression stage. (b) Molecular snapshot of system 2 (200 lubricant molecules), with L-OPLS-AA at 0.1 GPa and 100 °C after the compression stage. Carbon atoms are coloured with cyan, hydrogen atoms with purple, oxygen atoms with red and iron atoms with silver.

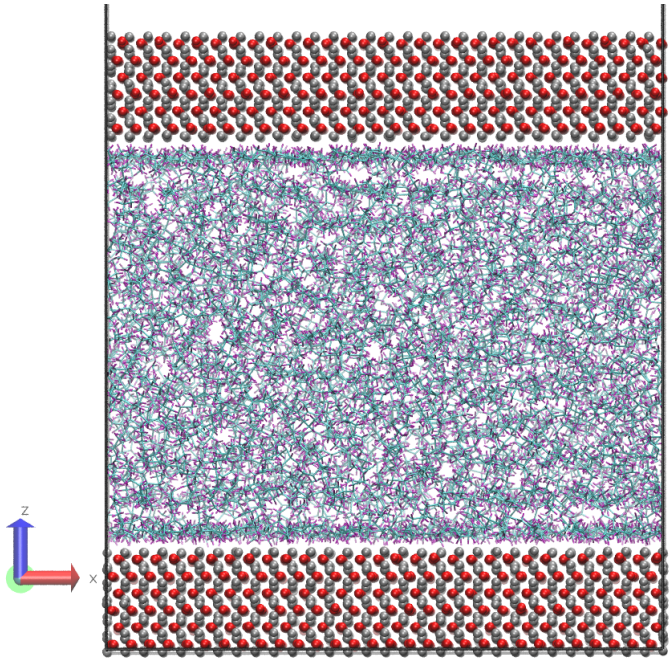

FIGURE 5.6: Molecular snapshot of system 3 (450 lubricant molecules), with L-OPLS-AA at 0.1 GPa and 100 °C after the compression stage. Carbon atoms are coloured with cyan, hydrogen atoms with purple, oxygen atoms with red and iron atoms with silver.

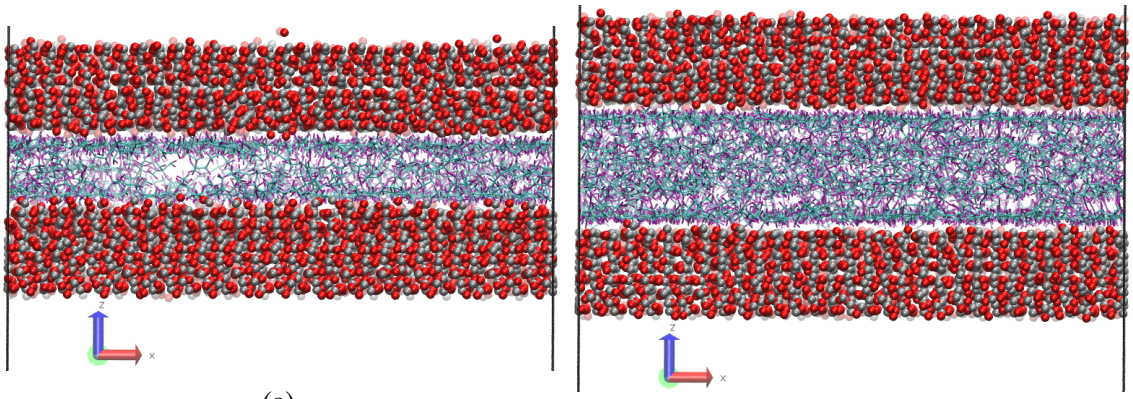

(a) (b)

FIGURE 5.7: (a) Molecular snapshot of system 1 (100 lubricant molecules), with ReaxFF at 0.1 GPa and 100 °C during the shearing stage at a shear rate of $\dot{\gamma} = 10^{7.5}$ s^{-1}. (b) Molecular snapshot of system 2 (200 lubricant molecules), with ReaxFF at 0.1 GPa and 100 °C during the shearing stage at a shear rate of $\dot{\gamma} = 10^{7.5}$ s^{-1}. Carbon atoms are coloured with cyan, hydrogen atoms with purple, oxygen atoms with red and iron atoms with silver.

The structural analysis of the layering of the fluid due to the presence of the hard wall, seen in the confined simulations is presented in the following Figures, quantified as density profiles. The density profiles were acquired by averaging over the last 5000 iterations (1.25 ps for ReaxFF and 5 ps for L-OPLS-AA) during the production run of shearing.

Figure 5.8 and 5.9 show the atomic mass density profile in the z-direction, for system 2 (200 lubricant molecules) at 0.5 GPa and a log $\dot{\gamma}$ of 8.50, by using the ReaxFF and L-OPLS-AA force fields, respectively. The oscillatory atomic mass density profile closer to the surface indicates stronger layering of the lubricant when compared to the centre of the film. These oscillations are similar to those from confined NEMD simulations of squalane [118]. Additionally, by looking at the density profile closer to the surface, stronger layering was observed in ReaxFF than L-OPLS-AA for the same conditions that were tested.

Then, Figure 5.10 shows the atomic mass density profile in the z-direction, for system 3 (450 lubricant molecules) at a range of pressures (0.1 to 1.0 GPa) and a log $\dot{\gamma}$ of 8.50, by using the L-OPLS-AA force field. By comparing these density profiles, the following can be said. Firstly, by increasing the applied pressure, density oscillations become more apparent, and as expected, the overall densities increase as well. Secondly, the increase of pressure, shrinks the total density profile which is equivalent to the volume contraction where the fluid is confined.

By comparing the two systems (2 and 3) for the case of L-OPLS-AA (Figure 5.9 and Figure 5.10b), we see that by increasing the number of lubricant molecules, the density oscillations near the centre of the film decrease.

Finally, the average density of the confined fluid near the centre of the film (region of 0.2 - 0.3, Figure 5.10a) is in excellent agreement with the respective density of the bulk liquid simulations at 0.1 GPa, with both densities being equal to 0.79 g/ml.

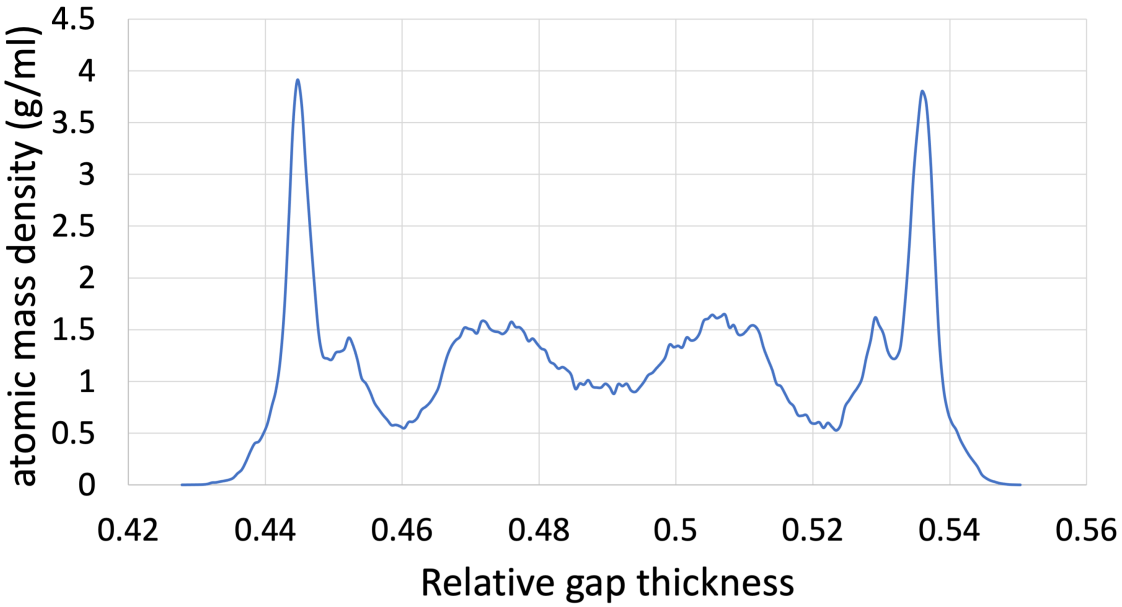

FIGURE 5.8: Atomic mass density profile of system 2 (200 lubricant molecules) with ReaxFF at 100 °C, a log $\dot{\gamma}$ of 8.50 and a pressure of 0.5 GPa.

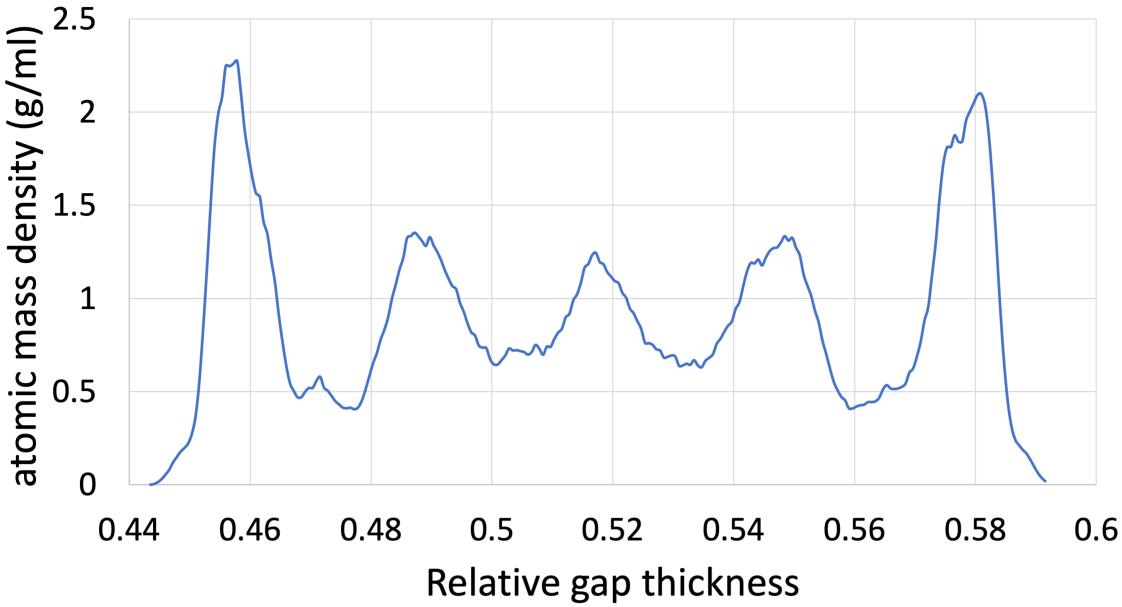

FIGURE 5.9: Atomic mass density profile of system 2 (200 lubricant molecules) with L-OPLS-AA at 100 °C, a log $\dot{\gamma}$ of 8.50 and a pressure of 0.5 GPa.

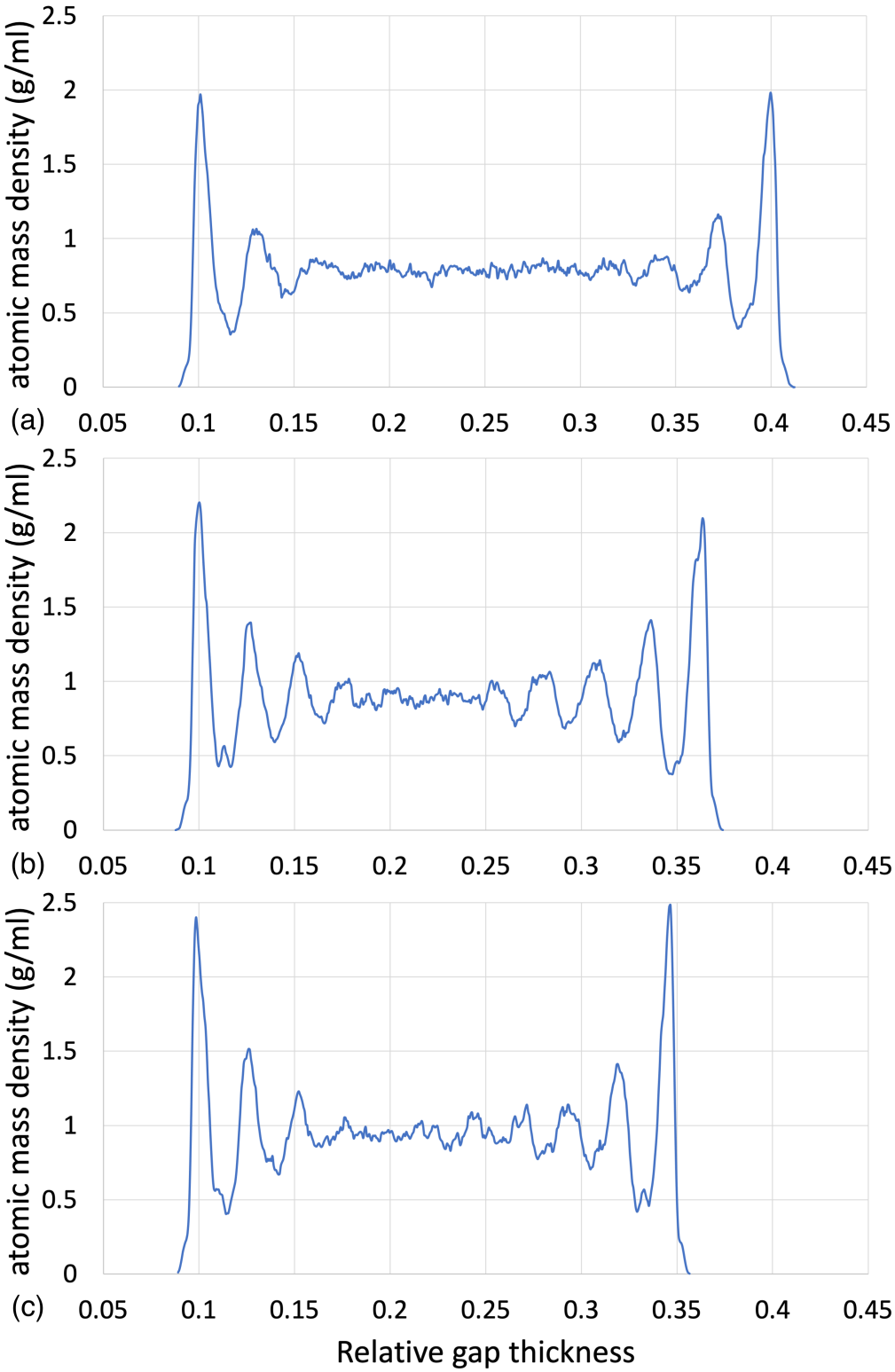

FIGURE 5.10: Atomic mass density profile of system 3 (450 lubricant molecules) with L-OPLS-AA at 100 °C, a log $\dot{\gamma}$ of 8.50 and a pressure range of (a) 0.1 GPa, (b) 0.5 GPa and (c) 1.0 GPa.

Table 5.3: Average film thickness L-OPLS-AA (last 2 ns) and ReaxFF (last 0.5 ns) simulations.

Lubricant molecules	**System**	**Film thickness (Å)**	**Force field**	***P*** **(GPa)**
100	1	13.70 $\pm$ 0.08	L-OPLS-AA	0.1
200	2	25.40 $\pm$ 0.12	L-OPLS-AA	0.1
450	3	55.93 $\pm$ 0.22	L-OPLS-AA	0.1
100	1	12.45 $\pm$ 0.04	ReaxFF	0.1
200	2	19.59 $\pm$ 0.06	ReaxFF	0.1
100	1	12.27 $\pm$ 0.04	L-OPLS-AA	0.5
200	2	22.75 $\pm$ 0.06	L-OPLS-AA	0.5
450	3	49.54 $\pm$ 0.09	L-OPLS-AA	0.5
100	1	11.06 $\pm$ 0.03	ReaxFF	0.5
200	2	17.91 $\pm$ 0.03	ReaxFF	0.5
100	1	11.44 $\pm$ 0.04	L-OPLS-AA	1.0
200	2	21.50 $\pm$ 0.05	L-OPLS-AA	1.0
450	3	46.43 $\pm$ 0.07	L-OPLS-AA	1.0
100	1	10.12 $\pm$ 0.02	ReaxFF	1.0
200	2	17.35 $\pm$ 0.03	ReaxFF	1.0

Then, Table 5.3 shows the different average film thicknesses with their respective standard deviation for the various systems studied for a single independent trajectory (three in total). The following observations can be derived from the table.

Firstly, it can be seen that by increasing the number of confined lubricant molecules within the two iron oxide surfaces the standard deviation of the average film thickness increases. This can be explained as a consequence of the increase of repulsion forces arising from the lubricant. This effect, creates an increased oscillation of the separation of the two surfaces.

Secondly, it can be seen that by applying higher pressure loads at the upper outermost layer of the iron oxide slab, for a given system that has the same number of lubricant molecules and regardless of the force field used, the standard deviation of the average film thickness decreases. This can be explained by the fact that the increase of pressure leads to

less freedom of movement for the lubricant molecules, while overcoming repulsion forces between the lubricant and the walls.

Thirdly, compared to L-OPLS-AA, ReaxFF simulations resulted in a thinner film for the same systems and conditions. This can be explained by the fact that ReaxFF is a reactive force field and lubricant atoms can come closer into contact with the surface in contrast to L-OPLS-AA, where repulsion forces wouldn't allow atoms to come too close (see Figure 5.5b and 5.7b). It appears that this difference is more evident at higher pressures (Table 5.3).

Figure 5.11, 5.12 and 5.13 show the compression stage during the time evolution of the simulation when using the L-OPLS-AA force field for the three different systems (1, 2 and 3).

As can be seen from the graphs, the time required to reach a fully compressed state, that is when the film thickness oscillates around a constant average value and its standard deviation becomes minimum, increases by the system's size. This can be explained by the increase of repulsion forces arising from the lubricant. The time required to fully compress the system cannot be known *a priori*, and as a result it is suggested to run simulations long enough, while monitoring the average film thickness.

Additionally, for a given system size, it can be seen that the applied pressure influences the time required for achieving a fully stable and compressed system, this can be seen more clearly in Figure 5.13, where more than 3 ns of simulation time are needed for the lowest pressure of 0.1 GPa to reach equilibrium, while for the highest pressure of 1.0 GPa less than 1 ns is required.

On the other hand, Figure 5.14 and 5.15 show the compression stage during the time evolution of the simulation when using the ReaxFF force field for the two different systems (1 and 2). It was found that the ReaxFF force field was slower than the L-OPLS-AA force field in both terms of time required for reaching equilibrium during compression and overall time performance (approximately 44 times slower than L-OPLS-AA).

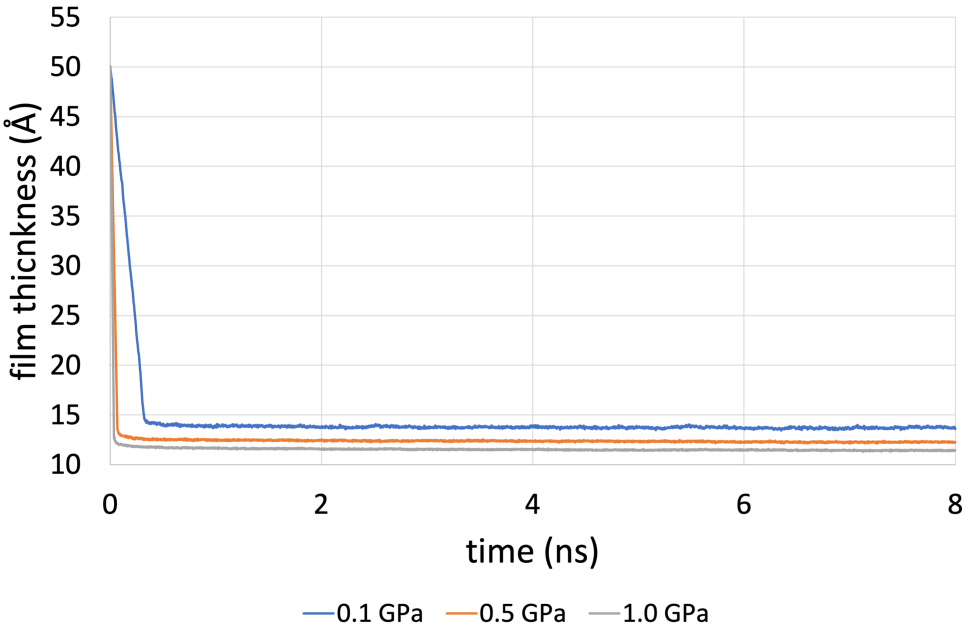

FIGURE 5.11: Film thickness of system 1 (100 lubricant molecules), with L-OPLS-AA at 100 °C during the compression stage of 8 ns. For all three pressures, there was a rapid compression and the film thickness oscillated around a constant value.

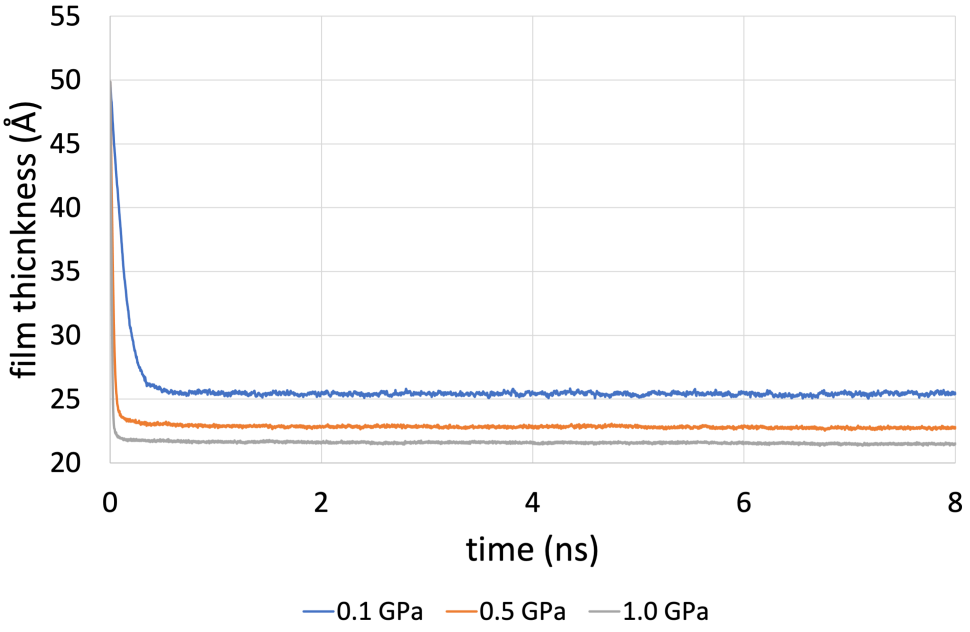

FIGURE 5.12: Film thickness of system 2 (200 lubricant molecules), with L-OPLS-AA at 100 °C during the compression stage of 8 ns. For all three pressures, there was a rapid compression and the film thickness oscillated around a constant value.

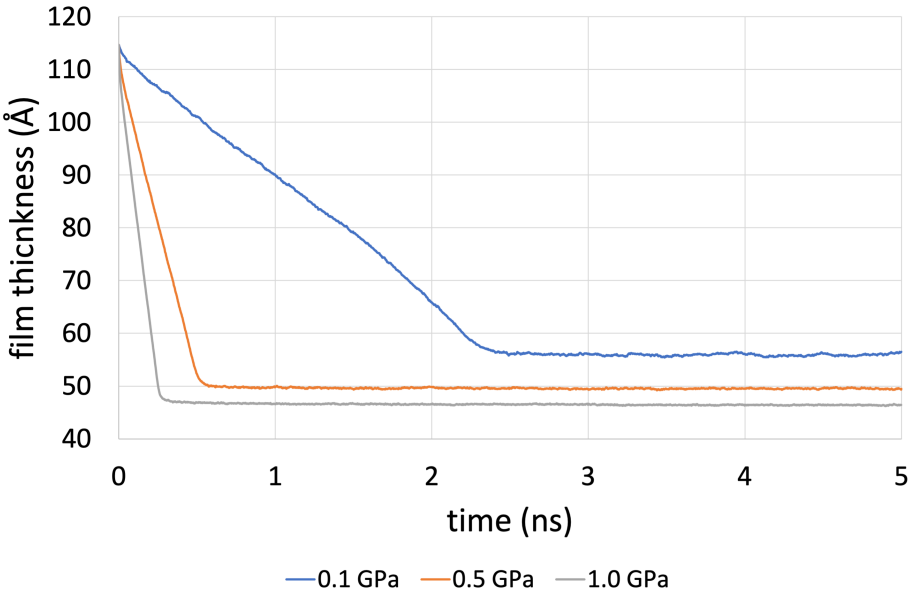

FIGURE 5.13: Film thickness of system 3 (450 lubricant molecules), with L-OPLS-AA at 100 °C during the compression stage of 5 ns. For this case, compression is slower compared to system 1 and 2, as there are more confined lubricant molecules between the iron oxide slabs. This results to increased repulsion forces arising from the lubricant.

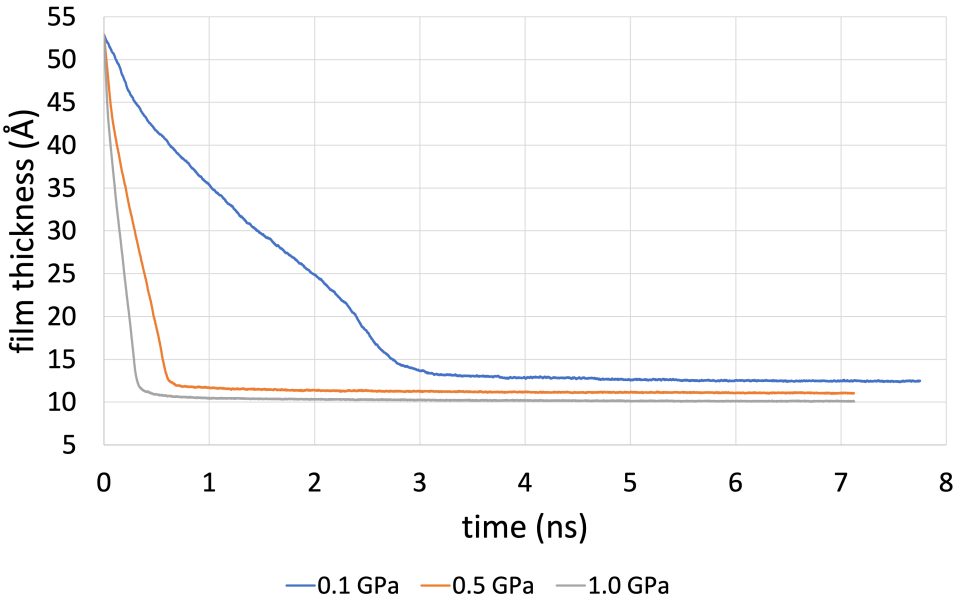

FIGURE 5.14: Film thickness of system 1 (100 lubricant molecules), with ReaxFF at 100 °C during the compression stage. As we decrease pressure, the simulation needs to run for longer so that the system reaches a fully-compressed state.

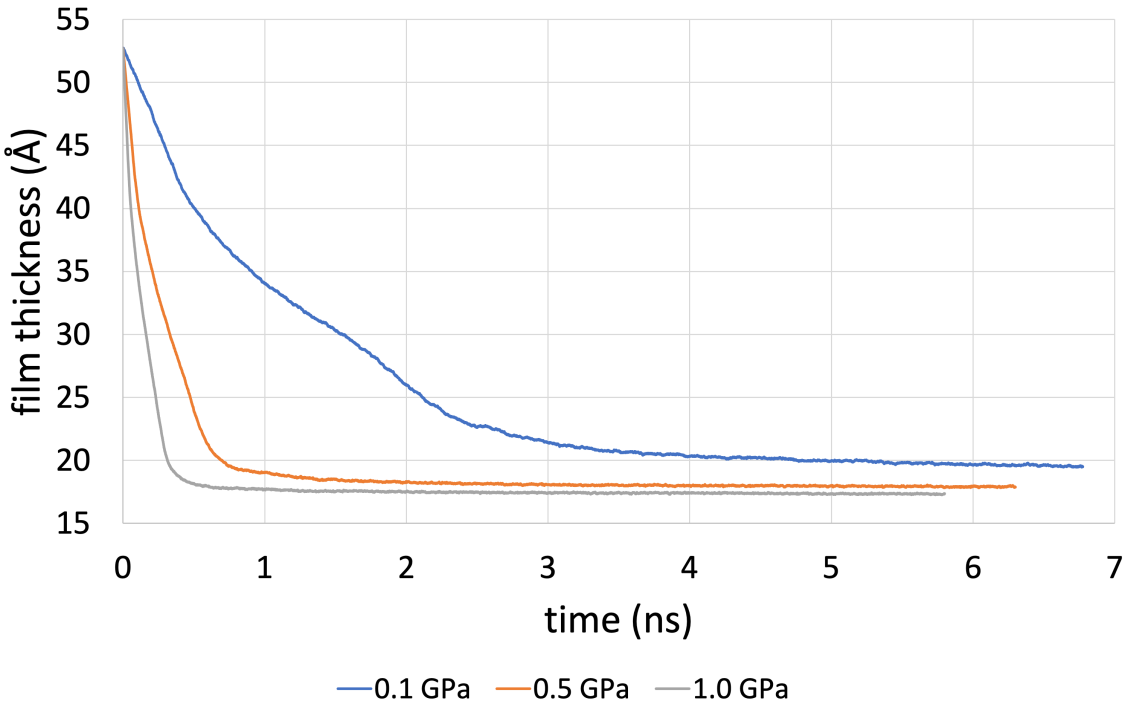

FIGURE 5.15: Film thickness of system 2 (200 lubricant molecules), with ReaxFF at 100 °C during the compression stage. Again, as we decrease pressure, the simulation needs to run for longer so that the system reaches a fully-compressed state.

Referring to the calculation of viscosity for the confined systems, Table 5.4 and Table 5.5 show the viscosity results obtained from molecular simulation with the L-OPLS-AA and ReaxFF force field at 100 °C, respectively. From these two tables, the following observations can be derived.

When we take into consideration the effect on viscosity by varying the number of confined lubricant molecules within the surfaces, it can be seen that in both force field cases, when applying the same pressure and shear rate, viscosity decreases when then number of lubricant molecules increases. This makes sense physically, as there is an easier movement of the fluid when there are more molecules, which results in a thicker film with a lower value of viscosity. On the other hand, when the film is too thin, for example in system 1 (100 molecules), the surfaces affect more the freedom of movement than in the cases of thicker films, thus resulting in a higher viscosity.

Table 5.4: Viscosity results of 9,10-dimethyloctadecane at 100 °C using L-OPLS-AA and comparison with bulk simulations. Note that the deviation is in respect to the bulk value at the same operational conditions of temperature, pressure and shear rate.

Lubricant molecules	**System**	**log shear rate**	***P*** **(GPa)**	**Viscosity (mPa s)**	**Deviation %**	**Viscosity (bulk sim.) (mPa s)**
100	1	7.50	0.1	27.8	300	6.94
100	1	7.50	0.5	664	425	126
100	1	7.50	1.0	1.95×10^3	48	1.32×10^3
100	1	8.50	0.1	15.0	132	6.47
100	1	8.50	0.5	117	50	78.1
100	1	8.50	1.0	236	-13	272
200	2	7.50	0.1	22.3	221	6.94
200	2	7.50	0.5	431	241	126
200	2	7.50	1.0	1.56×10^3	19	1.32×10^3
200	2	8.50	0.1	11.4	76	6.47
200	2	8.50	0.5	103	33	78.1
200	2	8.50	1.0	223	-18	272
450	3	7.50	0.1	6.50	-6	6.94
450	3	7.50	0.5	178	41	126
450	3	7.50	1.0	1.31×10^3	-0.4	1.32×10^3
450	3	8.50	0.1	6.21	-4	6.47
450	3	8.50	0.5	85.9	10	78.1
450	3	8.50	1.0	230	-16	272

Secondly, the change in the applied shear rate resulted in almost all cases, in shear thinning, which means a significant decrease in viscosity when an increased shear rate is applied. The only exception was the case of system 3 (L-OPLS-AA), where at a pressure of 0.1 GPa, the viscosity values for both applied shear rates were very close, as for this case, simulations were very close to the Newtonian regime, where viscosity does not depend on the applied shear rate, and has a constant value.

Referring to the pressure effect on viscosity, as expected, for each system at a specific shear rate, the viscosity increased when a higher pressure was applied externally. Then, compared to the use of bulk NEMD simulations (system 4), presented in Chapter 4, it was

found that as we increase the number of lubricant molecules we approach bulk behaviour of viscosity, as can be seen in Table 5.4, which compares simulations with the bulk systems using the L-OPLS-AA force field. This very interesting behaviour is discussed in more detail in the following paragraphs. The ReaxFF force field overestimated viscosity compared to the L-OPLS-AA force field but we observe the same change in viscosity behaviour qualitatively. The deviation between the two force fields is more apparent in lower pressures. For example, at $P = 0.5$ GPa and $\dot{\gamma} = 10^{8.5}$ s^{-1} (system 2) ReaxFF overestimated viscosity by 224% compared to L-OPLS-AA, while at $P = 1.0$ GPa and $\dot{\gamma} = 10^{8.5}$ s^{-1} (system 2) ReaxFF overestimated viscosity by 172%.

Table 5.5: Viscosity results of 9,10-dimethyloctadecane at 100 °C using ReaxFF at a pressure range of 0.1 to 1.0 GPa and a $\log(\dot{\gamma}[s^{-1}])$ range of 7.5 to 8.5.

Lubricant molecules	**System**	**log shear rate**	***P* (GPa)**	**Viscosity (mPa s)**
100	1	7.50	0.1	903
100	1	7.50	0.5	1.96×10^3
100	1	7.50	1.0	3.24×10^3
100	1	8.50	0.1	294
100	1	8.50	0.5	540
100	1	8.50	1.0	764
200	2	7.50	0.1	454
200	2	7.50	0.5	1.11×10^3
200	2	7.50	1.0	1.90×10^3
200	2	8.50	0.1	181
200	2	8.50	0.5	335
200	2	8.50	1.0	607

The time-averaged viscosity during the shearing stage of the production run for the various systems (1, 2 and 3) can be seen in Figure 5.16, 5.17 and 5.18 for the case of L-OPLS-AA, and in Figure 5.19 and 5.20 for the case of ReaxFF.

As can be seen from the graphs, for the case of L-OPLS-AA, simulations ran for long enough until the average viscosity value became time-independent. For the cases that

required to run for longer, convergence was monitored by comparing the viscosity averages obtained by the subsequent runs of 16 ns and the resulting standard deviation of viscosity during these runs, that eventually became insignificant in respect to the time-averaged viscosity.

The overall trend was that simulations at a shear rate of $10^{7.5}$ s^{-1} (blue, red and purple lines, respectively) required more simulation time than those at a shear rate of $10^{8.5}$ s^{-1} (orange, yellow and green lines, respectively), in order to reach a converged value of viscosity. This is due to the fact that at lower shear rates, the equilibrium fluctuations become comparable with the non-equilibrium response, which results in a lower signal-to-noise ratio, and as a result, we need to increase the sampling interval of viscosity, which in the end is the whole duration of the simulation. All simulations converged successfully. By increasing pressure, viscosity had a huge variation covering values of three orders of magnitude.

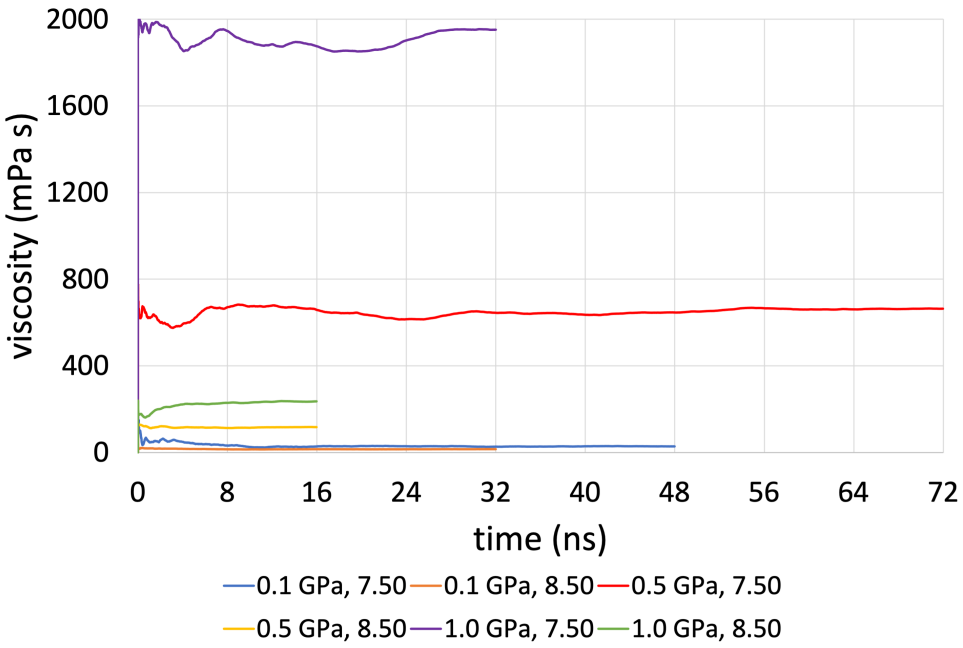

FIGURE 5.16: Average viscosity of system 1 (100 lubricant molecules), with L-OPLS-AA at a pressure range from 0.1 to 1.0 GPa at 100 °C and at a shear rate range of $10^{7.5}$ - $10^{8.5}$ s^{-1}.

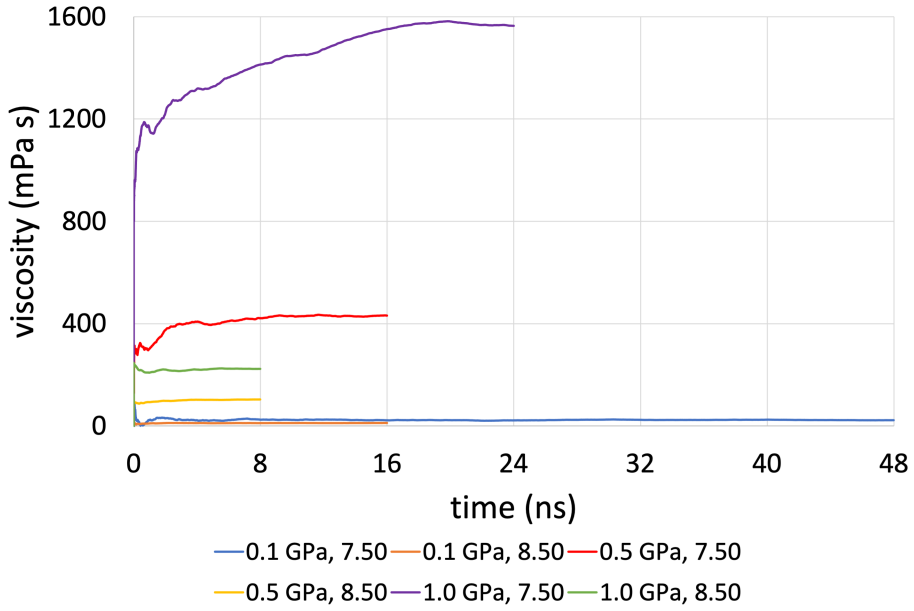

FIGURE 5.17: Average viscosity of system 2 (200 lubricant molecules), with L-OPLS-AA at a pressure range from 0.1 to 1.0 GPa at 100 °C and at a shear rate range of $10^{7.5}$ - $10^{8.5}$ s^{-1}.

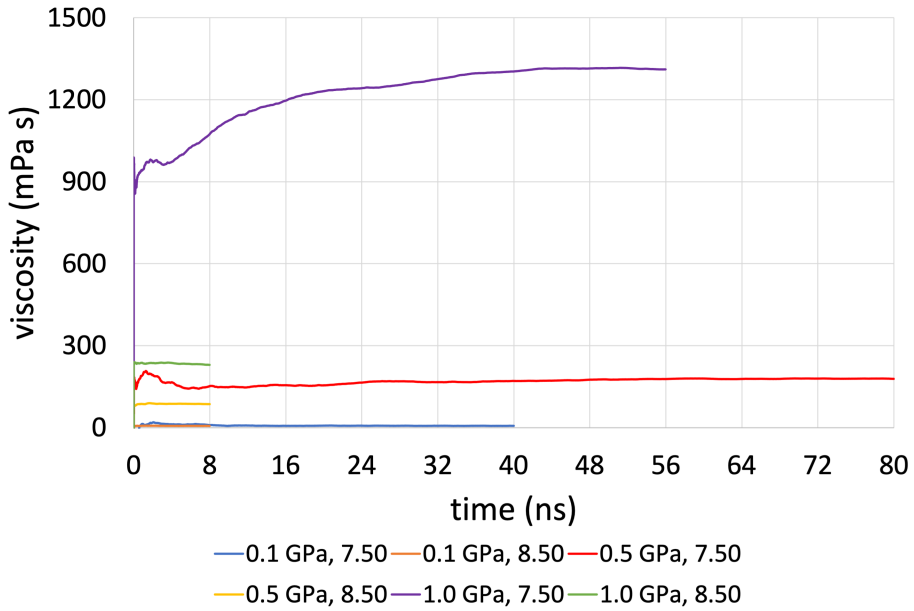

FIGURE 5.18: Average viscosity of system 3 (450 lubricant molecules), with L-OPLS-AA at a pressure range from 0.1 to 1.0 GPa at 100 °C and at a shear rate range of $10^{7.5}$ - $10^{8.5}$ s^{-1}.

For the case of ReaxFF, again, simulations at shear rates of $10^{8.5}$ s^{-1} converged faster and resulted in a more stable result than the case of $10^{7.5}$ s^{-1}, where simulations had more fluctuations. As can be seen in Figure 5.19 and 5.20 simulations ran for 1 ns due to the very computationally expensive ReaxFF and for saving computational resources.

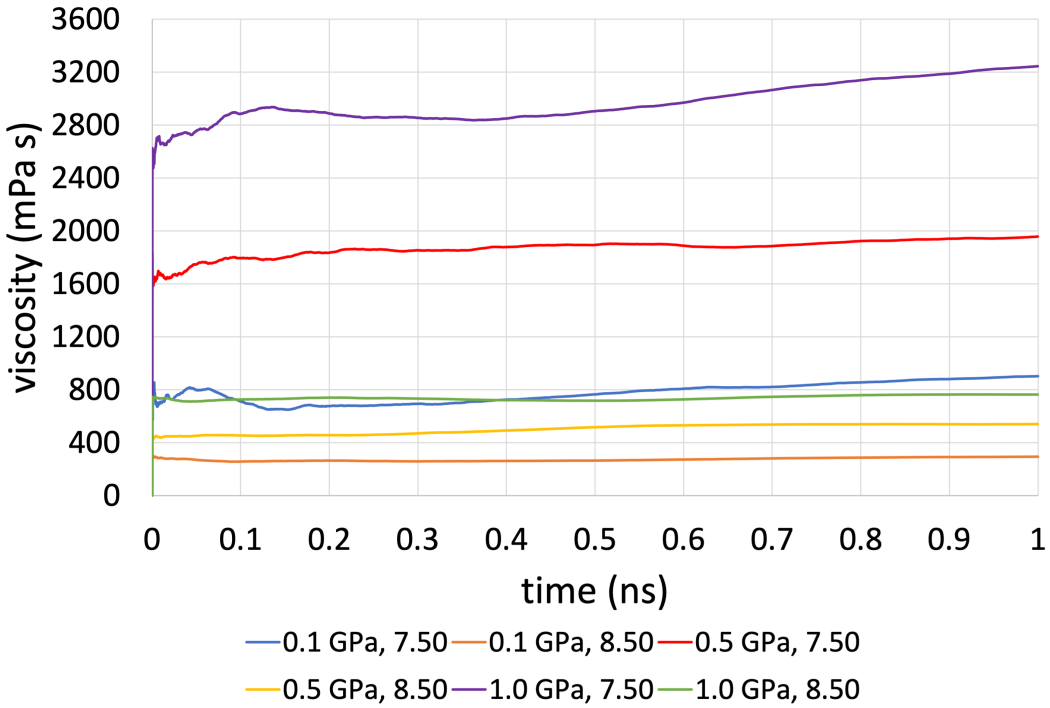

FIGURE 5.19: Average viscosity of system 1 (100 lubricant molecules), with ReaxFF at a pressure range from 0.1 to 1.0 GPa at 100 °C and at a shear rate range of $10^{7.5}$ - $10^{8.5}$ s^{-1}.

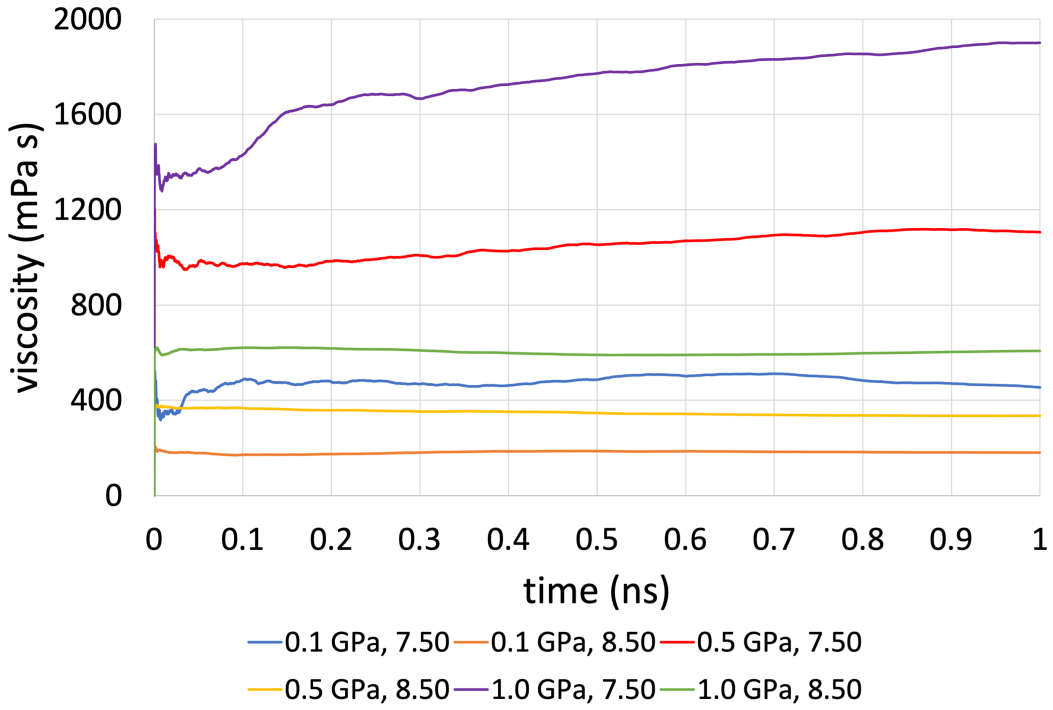

FIGURE 5.20: Average viscosity of system 2 (200 lubricant molecules), with ReaxFF at a pressure range from 0.1 to 1.0 GPa at 100 °C and at a shear rate range of $10^{7.5}$ - $10^{8.5}$ s^{-1}.

The following Figures (5.21 - 5.26) show the very interesting behaviour of viscosity as a function of the number of lubricant molecules confined within the iron oxide surfaces, which are compared against the bulk NEMD simulations (system 4).

It is very clear from the graphs, that the overall trend of viscosity, as we reach a film thickness close to the bulk simulation, is that we approach the bulk values of viscosity. This means that if the number of lubricant molecules is sufficient, confined NEMD can also give reliable viscosity results that are close to the bulk viscosity values. In addition, we conclude that an additional parameter that can affect the viscosity of a liquid is its film thickness (for thin films) but this is not always the case. We also have to take into consideration that in tribological interfaces, the film thickness is relatively thicker (800 to 1,500 Å) [118] which means that the surface effect might not be present in reality.

The only exception was the case of the highest pressure of 1.0 GPa at high shear rate of $10^{8.5}$ s^{-1}, where all systems gave very similar results, which leads us to the conclusion

that system size effects are not present at the high pressure - high shear rate regimes.

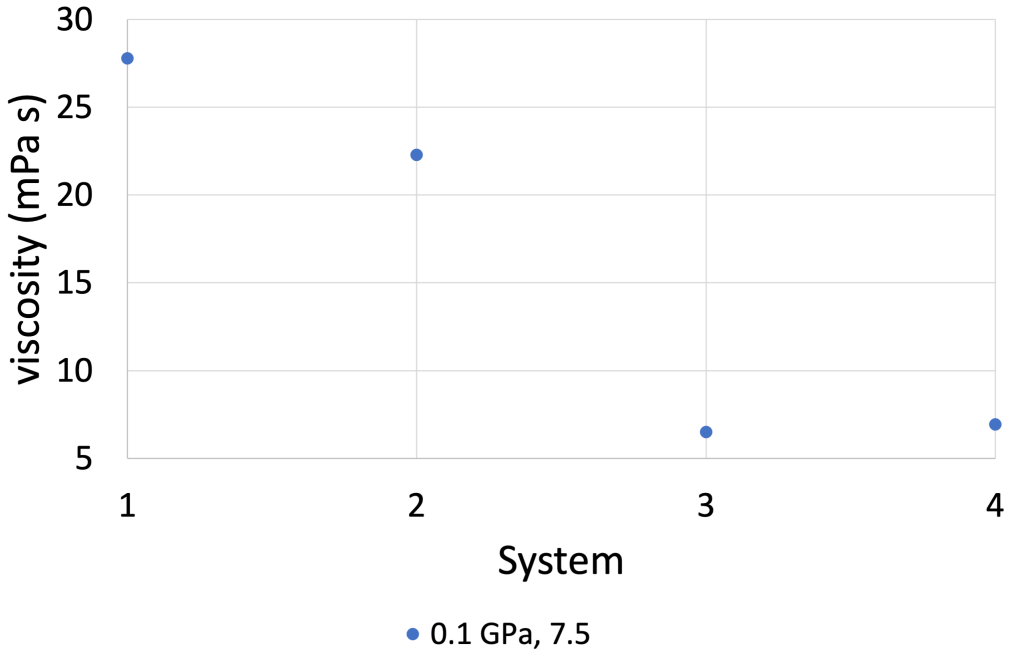

FIGURE 5.21: Viscosity results comparison between confined NEMD simulations (system 1, 2 and 3) and bulk NEMD simulations (system 4) at $P = 0.1$ GPa and $\log(\dot{\gamma}[\mathrm{s}^{-1}]) = 7.5$, by using the L-OPLS-AA force field. As we increase the number of confined lubricant molecules we approach bulk behaviour of viscosity. System 1, 2 and 3 contain 100, 200 and 450 lubricant molecules, respectively.

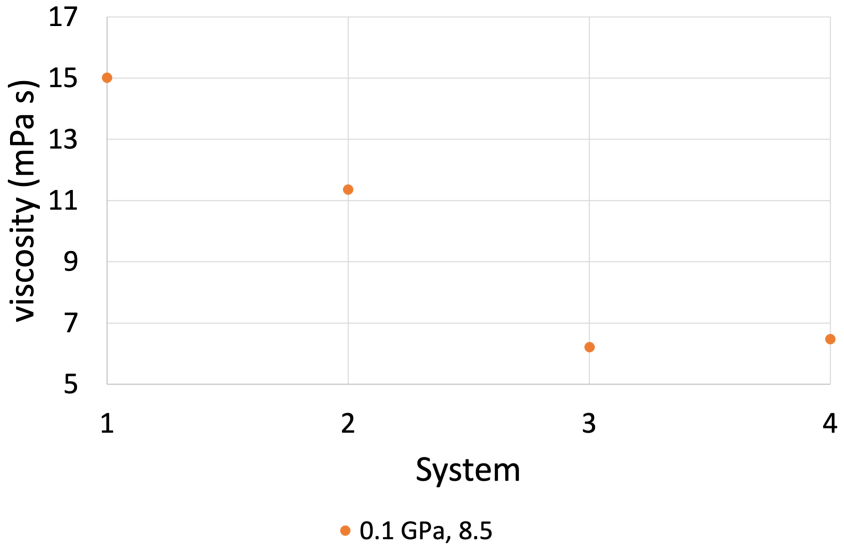

FIGURE 5.22: Viscosity results comparison between confined NEMD simulations (system 1, 2 and 3) and bulk NEMD simulations (system 4) at $P = 0.1$ GPa and $\log(\dot{\gamma}[\mathrm{s}^{-1}]) = 8.5$, by using the L-OPLS-AA force field. As we increase the number of confined lubricant molecules we approach bulk behaviour of viscosity. System 1, 2 and 3 contain 100, 200 and 450 lubricant molecules, respectively.

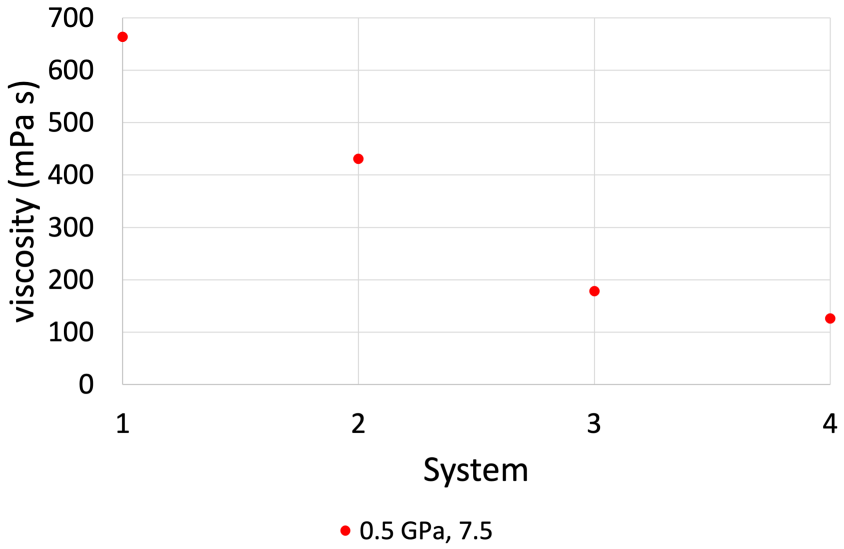

FIGURE 5.23: Viscosity results comparison between confined NEMD simulations (system 1, 2 and 3) and bulk NEMD simulations (system 4) at $P = 0.5$ GPa and $\log(\dot{\gamma}[\mathrm{s}^{-1}]) = 7.5$, by using the L-OPLS-AA force field. As we increase the number of confined lubricant molecules we approach bulk behaviour of viscosity. System 1, 2 and 3 contain 100, 200 and 450 lubricant molecules, respectively.

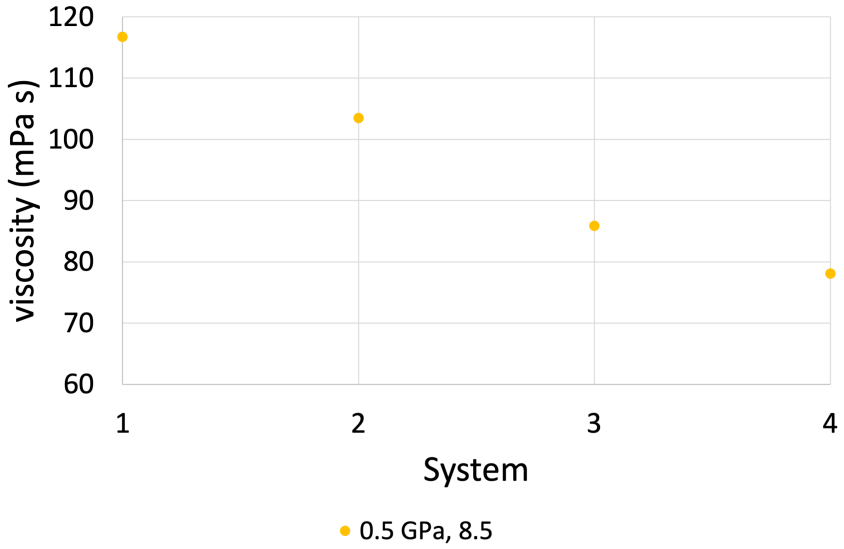

FIGURE 5.24: Viscosity results comparison between confined NEMD simulations (system 1, 2 and 3) and bulk NEMD simulations (system 4) at $P = 0.5$ GPa and $\log(\dot{\gamma}[\mathrm{s}^{-1}]) = 8.5$, by using the L-OPLS-AA force field. As we increase the number of confined lubricant molecules we approach bulk behaviour of viscosity. System 1, 2 and 3 contain 100, 200 and 450 lubricant molecules, respectively.

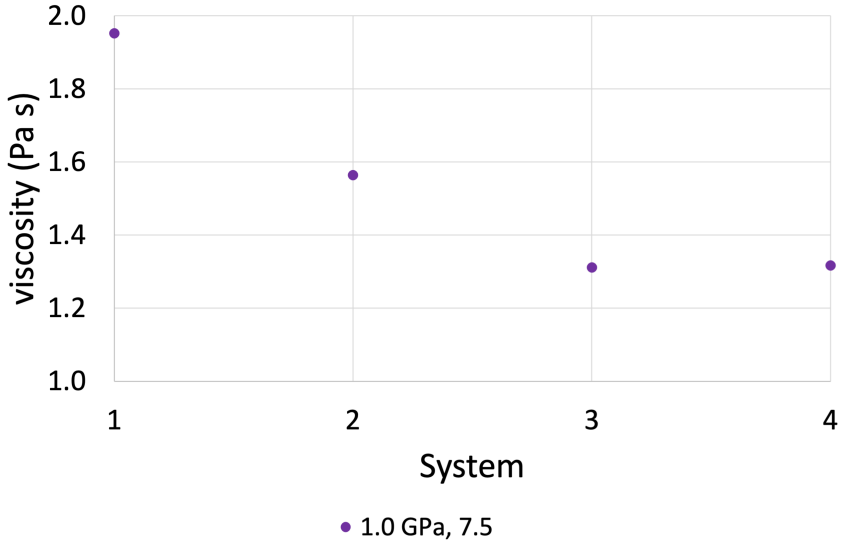

FIGURE 5.25: Viscosity results comparison between confined NEMD simulations (system 1, 2 and 3) and bulk NEMD simulations (system 4) at $P = 1.0$ GPa and $\log(\dot{\gamma}[\mathrm{s}^{-1}]) = 7.5$, by using the L-OPLS-AA force field. As we increase the number of confined lubricant molecules we approach bulk behaviour of viscosity. System 1, 2 and 3 contain 100, 200 and 450 lubricant molecules, respectively.

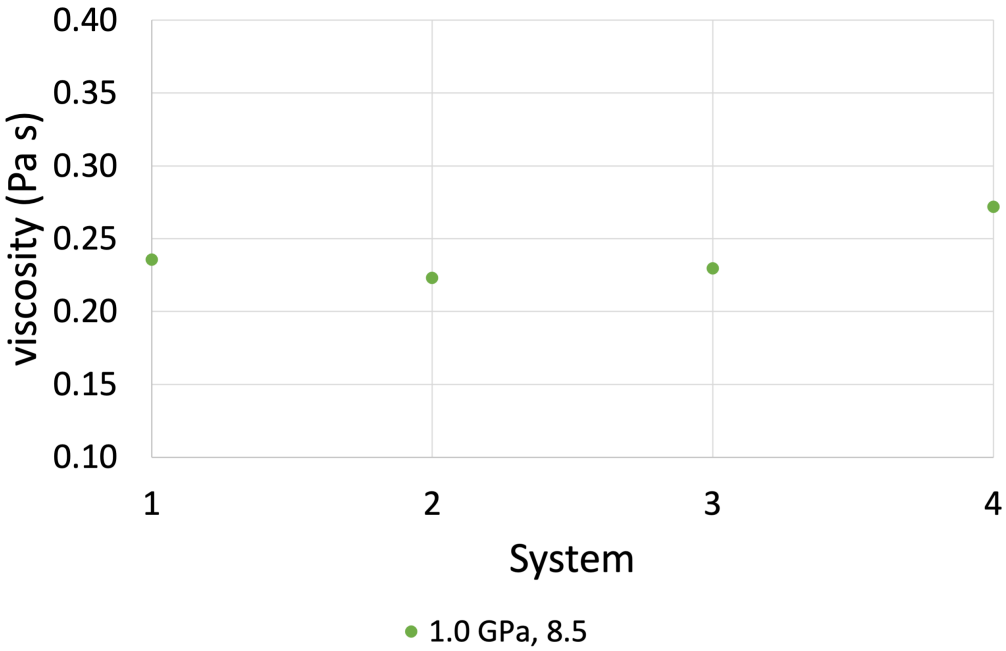

FIGURE 5.26: Viscosity results comparison between confined NEMD simulations (system 1, 2 and 3) and bulk NEMD simulations (system 4) at $P = 1.0$ GPa and $\log(\dot{\gamma}[\mathrm{s}^{-1}]) = 8.5$, by using the L-OPLS-AA force field. At this high pressure - high shear rate regime we notice that all confined systems have similar viscosity behaviour with the bulk liquid. System 1, 2 and 3 contain 100, 200 and 450 lubricant molecules, respectively.

Figure 5.27 shows the change in viscosity when using the ReaxFF force field, for system 1 and 2. Again we observe the same behaviour with L-OPLS-AA force field qualitatively, as viscosity decreased when the number of lubricant molecules increased. From the above, we conclude that the L-OPLS-AA force field is very reliable and should be used in confined NEMD simulations, while ReaxFF is not reliable for calculating viscosity, although it could be used for studying possible chemical reactions at high pressure - temperature regimes.

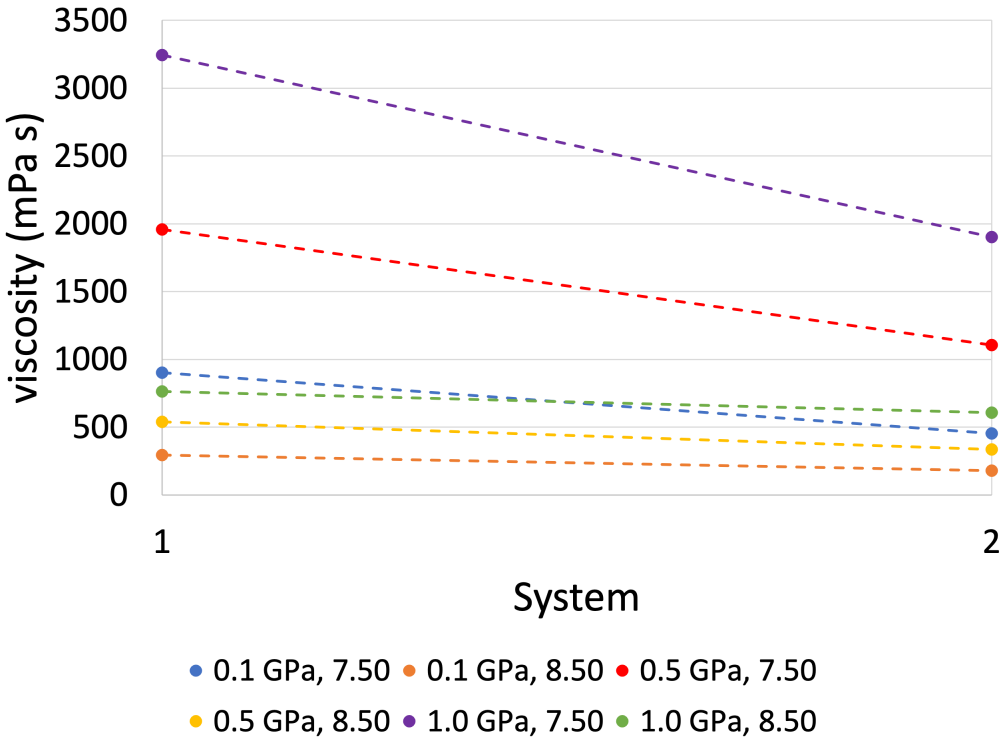

FIGURE 5.27: Viscosity results comparison of systems 1 and 2 at a pressure range of 0.1 to 1.0 GPa and a $\log(\dot{\gamma}[\mathrm{s}^{-1}])$ range of 7.5 to 8.5, by using the ReaxFF force field. System 1 and 2 contain 100 and 200 lubricant molecules, respectively.

Figure 5.28 shows the velocity profile of a confined NEMD simulation with L-OPLS-AA for system 3, at a chosen shear rate of $10^{8.5}$ s^{-1} and at a pressure of 1.0 GPa. The simulation box (across z) is divided into equally spaced regions. Then, the velocity vector component (x-dimension) of atoms that exist in each region at a particular timestep is averaged, and then averaged again over different time intervals every 5 ps, to improve statistics during the last 4 ns of the production run. The resulting velocity profile is linear, as described in simple Couette flow. To maintain the same shear rate in simulations at different pressures, the applied velocity at the top edge of the simulation box has to be adjusted accordingly, so as to take into account the change of the film thickness arising from each applied pressure.

Similarly, Figure 5.29 shows the velocity profile of a confined NEMD simulation with

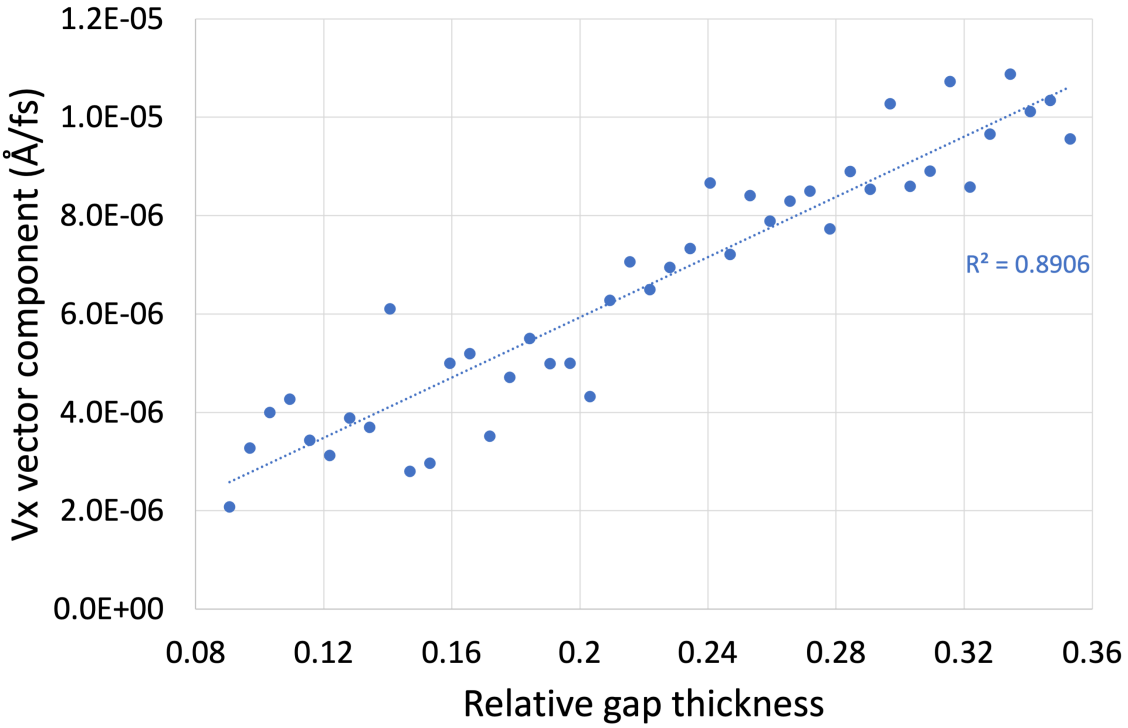

FIGURE 5.28: Velocity profile example of 9,10-dimethyloctadecane (450 molecules) at 100 °C, during confined NEMD with L-OPLS-AA at a chosen shear rate of $10^{8.5}$ s^{-1} and at a pressure of 1.0 GPa.

ReaxFF for system 2, at a chosen shear rate of $10^{8.5}$ s^{-1} and at a pressure of 0.1 GPa. The simulation box (across z) is divided into equally spaced regions. Then, the velocity vector component (x-dimension) of atoms that exist in each region at a particular timestep is averaged, and then averaged again over different time intervals every 1.25 ps, to improve statistics during the 1 ns production run.

The use of the L-OPLS-AA force field resulted in a more linear velocity profile than ReaxFF. This difference can be attributed to the sampling rate of the velocities, which was over a wider interval in the L-OPLS-AA case as it was for 4 ns compared to 1 ns for ReaxFF.

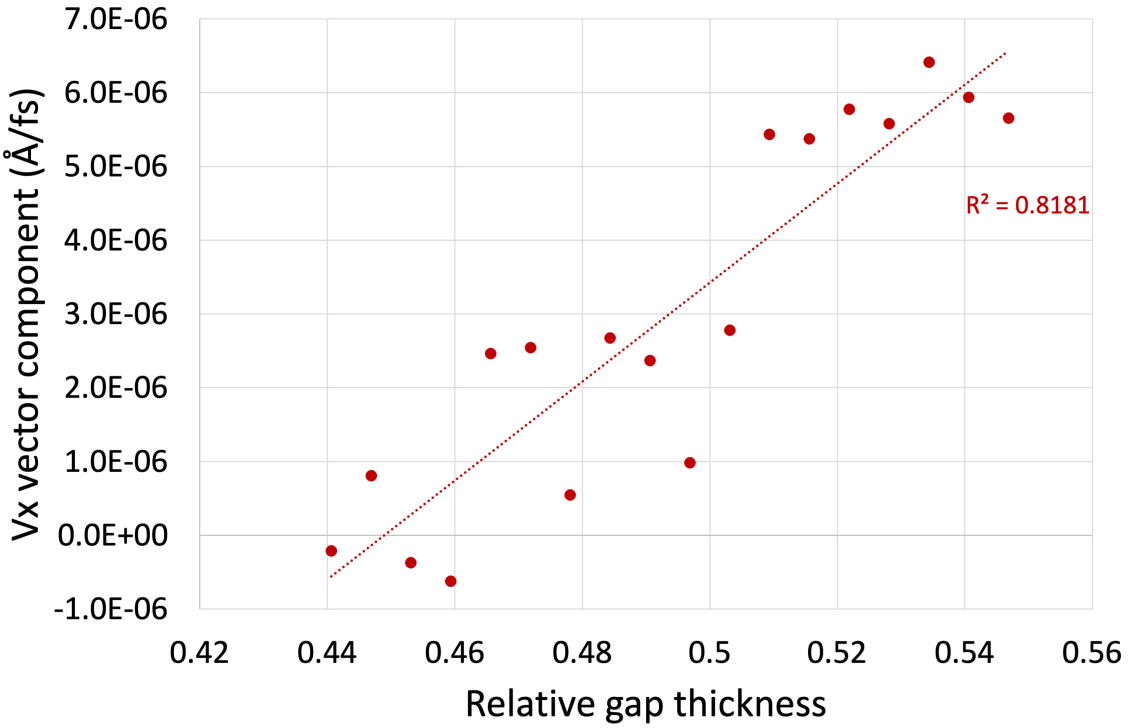

FIGURE 5.29: Velocity profile example of 9,10-dimethyloctadecane (200 molecules) at 100 °C, during confined NEMD with ReaxFF at a chosen shear rate of $10^{8.5}$ s^{-1} and at a pressure of 0.1 GPa.

5.5 Summary

In this Chapter we studied the use of confined non-equilibrium molecular dynamics for calculating shear viscosity at various pressures, shear rates and film thicknesses of the confined lubricant, which in our case was the 9,10-dimethyloctadecane, main component of PAO-2 base oil. For the explicitly defined wall surfaces, we used two iron oxide slabs.

It was demonstrated that confined NEMD simulations yield very interesting findings, as it was shown that the film thickness affects viscosity and as we increase the number of lubricant molecules, we approach the viscosity value of the bulk fluid, that was obtained with NEMD. In particular, viscosity values were in good agreement between the two methods (NEMD and confined NEMD), when there were enough lubricant molecules confined within the walls. In essence, we showed that by adding more lubricant molecules between

the walls, the wall effect on viscosity becomes more and more insignificant, achieving bulk behaviour of viscosity. The only exception that was observed was in the high pressure (1.0 GPa) - high shear rate ($10^{8.5}$ s^{-1}) regime, where the different film thicknesses had no influence on viscosity. This leads us to the conclusion that system size effects are not present in the high pressure - high shear rate regimes.

It was also found that the ReaxFF force field overestimates viscosity when compared to the L-OPLS-AA force field but the same change in viscosity behaviour is observed qualitatively. Therefore, we recommend that the L-OPLS-AA force field should be used in confined NEMD simulations for calculating viscosity of organic lubricants. The deviation between the two force fields was more apparent at lower pressures. For example, at $P =$ 0.5 GPa and $\dot{\gamma} = 10^{8.5}$ s^{-1} (system 2 - 200 lubricant molecules) ReaxFF overestimated viscosity by 224% compared to L-OPLS-AA, while at $P = 1.0$ GPa and $\dot{\gamma} = 10^{8.5}$ s^{-1} (system 2 - 200 lubricant molecules) ReaxFF overestimated viscosity by 172%.

Chapter 6

Conclusions

6.1 Summary

Molecular dynamics (MD) simulations can be used to compute macroscopic properties of industrial lubricant components from their behaviour at the molecular level. In this thesis, we have performed a critical evaluation of the use of MD to compute viscosity of widely used lubricants such as 9,10-dimethyloctadecane, main component of PAO-2 base oil. For this molecule, we have used and compared the three main techniques for such calculations: the Green-Kubo theory of fluctuations from equilibrium MD (EMD), the direct computation of viscosity from shear during non-equilibrium MD (NEMD) and the use of confined NEMD, where the fluid is confined within explicitly defined wall surfaces (iron oxide, in our case). Our simulations were performed at four different temperatures (40, 70, 100 and 150 °C) and a range of pressures from 0.1 MPa (ambient pressure) up to 1.0 GPa.

We found that EMD simulations, which represent zero shear conditions, were accurate at predicting viscosity values up to 0.3 GPa at 40 °C. But at higher pressures, where the viscosity increases by three orders of magnitude, EMD became unreliable. This matches observations of other authors [62] that EMD simulations are known to have a limited regime of applicability and should be used for liquids that have relatively low viscosity. High relaxation times, due to high pressures and viscosities, hinder the decay of the ACF

and thus, EMD simulations cannot capture viscosity accurately. This means that the upper limit of the integral of the ACF should be chosen to be long enough to ensure convergence of the viscosity by exceeding the rotational relaxation time of the molecule.

On the other hand, NEMD simulations at high pressures successfully captured zero shear viscosity, which was validated against experimental values. As a result, NEMD is suggested to be the method of choice in these operational conditions. We conclude that NEMD can be used to obtain atomic-level insights of lubricant interactions, while providing a reliable approach for computing viscosity, especially in cases where experimental measurement can be difficult.

Additionally, the use of confined NEMD simulations yielded very interesting findings, as it was shown that the film thickness affects viscosity and as we increase the number of lubricant molecules, we approach the viscosity value of the bulk fluid. The only exception was in the high pressure (1.0 GPa) - high shear rate ($10^{8.5}$ s^{-1}) regime, where the different film thicknesses had no influence on viscosity. This leads us to the conclusion that system size effects are not present in the high pressure - high shear rate regimes, which are also non-Newtonian regions.

The choice of force field was also investigated in our study by using three widely-used force fields. The first two, are similar from a functional point of view but have different parameterisation: these were the L-OPLS-AA and the GAFF2-AA force fields. The third one was the ReaxFF force field which employs a bond-order formalism in conjunction with polarisable charge descriptions to describe both reactive and non-reactive interactions between atoms.

We found that the L-OPLS-AA force field, which is specifically designed for long-chain hydrocarbons, achieves markedly better agreement with experimental viscosity values than GAFF2-AA, as the L-OPLS-AA force field overestimated viscosity by only 2% at a pressure of 0.8 GPa (40 °C case) while GAFF2-AA was over by a dramatic 114%. It was also found that the ReaxFF force field overestimates viscosity when compared to the L-

OPLS-AA force field but the same change in viscosity behaviour is observed qualitatively. Therefore, we recommend that the L-OPLS-AA force field should be used in confined NEMD simulations for calculating viscosity of organic lubricants. The deviation between the two force fields was more apparent at lower pressures. For example, at $P = 0.5$ GPa and $\dot{\gamma} = 10^{8.5}$ s^{-1} (system 2 - 200 lubricant molecules) ReaxFF overestimated viscosity by 224% compared to L-OPLS-AA, while at $P = 1.0$ GPa and $\dot{\gamma} = 10^{8.5}$ s^{-1} (system 2 - 200 lubricant molecules) ReaxFF overestimated viscosity by 172%. Despite the overestimation of viscosity, as a reactive force field, ReaxFF could be useful to study chemical reactions that occur at high pressures. Then, running simulations either for longer time periods, or multiple repeats, allowed us to obtain results with a lower standard deviation of viscosity, which was more noticeable at lower shear rates ($\dot{\gamma} < 10^{7}$ s^{-1}) and pressures ($P < 0.5$ GPa) with NEMD simulations. We also found that in their region of applicability, the values of the reciprocal asymptotic isoviscous pressure coefficient for both EMD-GK and NEMD methods were in reasonable agreement with experiment when the L-OPLS-AA force field was used. By choosing this force field, we expect that the methods used in this study can be applied to similar lubricants at various temperatures and pressures.

We hope that this thesis will serve as a benchmark for future simulations of viscosity of lubricants with applications in industry. Our work is applicable in providing practical demonstrations of state-of-the-art simulation of viscosity at high or low values in the Newtonian regime and away from it as well. This is particularly useful for industrial applications as simulations could reduce the operational cost as results could be obtained faster through the use of automation and supercomputers, while limiting the use of chemicals for a more sustainable future. Then, confined NEMD simulations could be used as a digital twin of tribological systems, where simulations can aid in the calculation of viscosity, which could be otherwise difficult to monitor inside the bearing interface.

Part of our work has been published in the Tribology Transactions journal, having received four citations at the time of submission of this thesis.

6.2 Future work

Future extension of this work could aim towards the addition of inorganic complexes as additives, such as MoDTP (molybdenum dithiophosphate) and ZDDP (zinc dialkyldithiophosphate). This system, which includes a lubricant, a surface and an additive, could be combined in order to study single additive deposit and redissolution on steel or iron oxide surface, followed by competing additive deposit and redissolution. However, the arising issue in this case is the development of appropriate force field parameters for the system. A solution to this issue could be the use of an accelerated semiempirical tight-binding method, namely GFN2-xTB [121], for investigating the interaction of these inorganic complexes with the surface. This method, which can be used to treat interactions for almost the whole periodic table of elements, is coupled with metadynamics by introducing a biasing root-mean-square deviation potential to the total tight-binding energy.

The current implementation of this method uses the root-mean-square-deviation in Cartesian space as a collective variable, which has been shown [121] to result in efficient exploration of wide regions of the conformational potential energy surface and rare events that might take place. Considering that choosing a set of appropriate collective variables is far from trivial, it is suggested to begin with this choice as a collective variable, at least for a start. Future considerations of alternative collective variables could be the atomic distance between the surface and the center of the inorganic complex (Zn or Mo), but simulations would be needed in order to prove this.

This computational tool might prove to be useful for this research, in order to study possible reactions between surfaces and additives, that might occur in the high temperature and pressure regime. In particular, by comparing the reconstructed potential energy surface of two systems, each containing one of the previously mentioned additives (MoDTP and ZDDP), conclusions could be made on which additive has stronger adhesion on the surface and this could be an initial indication of which additive would overtake the other

in competing additive deposit and redissolution.

To summarise, the use of GFN2-xTB metadynamics simulations, which are based on tight-binding quantum chemical calculations, can aid in the enhanced sampling of the configurational space and have capabilities to explore the chemical reaction space.

Additionally, the workflow scripts that were developed in this work could be used to study more complicated mixtures of liquids in order to show how the different ratios of molecules inside the lubricant affect viscosity.

All of the above could give an insight into the tribological behaviour of steel interactions with lubricants at the nanoscale level, helping to enhance bearing performance, adding value to the product, that has more endurance and reduced friction, while resulting in less CO_2 production by the automotive engine.

Appendix A

Scientific software and parallel programming

A.1 MolView platform

MolView [82] is an intuitive, open source web-application that can generate molecules by accessing online structural databases. MolView is mainly intended as a web-based data visualization platform. MolView can be used to search through different scientific databases including compound databases, protein databases and spectral databases, and view records from these databases as interactive visualizations using WebGL and HTML5 technologies. This web application is built on top of the JavaScript libraries and online services. The Virtual Model Kit has been a source of inspiration for the birth of this project [82]. The website for accessing and using MolView is:
https://molview.org

A.2 Packmol program

Packmol [81] creates an initial point for molecular dynamics simulations by packing molecules in defined regions of space. The packing guarantees that short range repulsive interactions do not disrupt the simulations. The great variety of types of spatial constraints that can be attributed to the molecules, or atoms within the molecules, makes it easy to

create ordered systems, such as lamellar, spherical or tubular lipid layers.

The user must provide only the coordinates of one molecule of each type, the number of molecules of each type and the spatial constraints that each type of molecule must satisfy. The package is compatible with input files of PDB, TINKER, XYZ and MOLDY formats [81]. Packmol can read simple file coordinates in order to fill simulation boxes of specified size with molecules that have randomised arrangement. The program is written in Fortran and can be downloaded from this link:
http://leandro.iqm.unicamp.br/m3g/packmol/download.shtml

A.3 Moltemplate program

Moltemplate [80] is a general cross-platform text-based molecule builder for LAMMPS. Moltemplate was intended for building custom coarse-grained molecular models, but it can be used to prepare realistic all-atom simulations as well.

It supports the ATB molecule database, as well as a wide variety of existing force fields and models including: OPLS, AMBER (GAFF, GAFF2), DREIDING, COMPASS, LOPLS (2015), EFF, TraPPE (1998), MOLC, mW, ELBA (water, oxDNA2). However it can be used to build molecules using any of the force fields (and atom styles) available in LAMMPS, including new force fields created by modifying the LAMMPS source code. (Note: Careful selection of atom types is necessary. Moltemplate does not support atom typing, and is not suitable for all-atom protein simulations.) Molecules can be copied, combined, and linked together as building-blocks to define new molecules (hierarchically). Once built, individual molecules and subunits can be customised (atoms, bonds, and subunits can be moved and deleted) [80]. Moltemplate is written in Python and can be downloaded from this link:
https://www.moltemplate.org/download.html

A.4 LAMMPS program

LAMMPS [79] is a classical molecular dynamics open source C++ code, which includes potentials for a variety of molecular systems. Its capabilities include parallel calculations and accelerated performance on CPUs, calculations of thermodynamic and system properties, and a variety of other implemented algorithms. A lot of molecular dynamics papers have used LAMMPS for their simulations. As the code is open source, modifications and extensions are easy to occur. In order to run a calculation, the user must provide a script which includes the simulation details. The first part is the definition of force field parameters and system interactions. Then, the second part is initialisation of the system, which has to be in a specific format so that LAMMPS can read the data. For example, atoms, bonds, angles and dihedral types need to be clear, otherwise the calculation fails. A very important fact is that the input script can be the result of a previous simulation, which means that LAMMPS has simulation restart capabilities and simulations can run for long enough. The third part specifies the run section, such as simulation ensembles, energy minimisation, timesteps, calculation of properties, and so on. The final part usually consists of writing data in log files that can be used in subsequent simulations, or calculating properties of interest. LAMMPS can be downloaded from this link:
https://www.lammps.org/download.html

A.5 The message-passing paradigm for parallel calculations

The Message-passing interface (MPI) [122] is a portable standard designed by a group of researchers from academia and industry to function on a wide variety of parallel computing architectures. The standard defines the syntax and semantics of a core of library routines useful to a wide range of users writing portable message-passing programs in C, C++, and Fortran. There are several well-tested and efficient implementations of MPI, many of which are open-source or in the public domain. These fostered the development

of a parallel software industry, and encouraged the development of portable and large-scale parallel applications. The concept of memory distribution can be seen in Figure A.1.

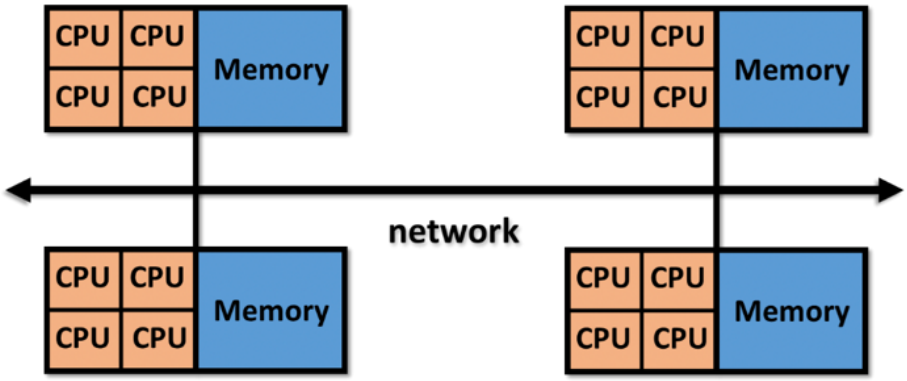

FIGURE A.1: MPI concept. Data are moved from the address space of one process to that of another process through cooperative operations.

MPI is a communication protocol for parallel programming. Both point-to-point and collective communication are supported. MPI is a message-passing application programming interface, together with protocol and semantic specifications that indicate how its features must behave in any implementation. MPI remains the dominant model used in high-performance computing today. Distributed memory supercomputers such as computer clusters usually run such programs. The advantages of MPI over older message passing libraries are portability and speed.

Appendix B

C code autocorrelation script for EMD-GK and NEMD viscosity averaging

```
// Autocorrelation script for EMD-GK

#include"stdio.h"
#include"stdlib.h"

#define  MAX_LEN  80

int main()
{
    FILE *fp1;
    int i,j,k,N,init; // indices
    int s,p,d,t_max,k_max;
    char string[MAX_LEN + 1];

    static float press[36000001][4]; // pressure values i index = t_max + 1 TO VARY
    static float c_xy[60000], c_xz[60000], c_yz[60000]; // correlation terms = p TO VARY
    static float SUM_xy[60000], SUM_xz[60000], SUM_yz[60000]; // sum terms TO VARY

    double scale;
    float visc_xy, visc_xz, visc_yz, total_visc, sum1, sum2, sum3, result;

    s = 5; // TO VARY
    p = 60000; // TO VARY
    d = s*p;
```

```
t_max = 3600000; // TO VARY

k_max = t_max/d;

scale = 1.58586069893965e-10; // DEPENDS ON SYSTEM'S SIZE

printf("s = %d p = %d d = %d t_max = %d k_max = %d scale = %.14lf \n", s,p,d,t_max,k_max,scale);

fflush(stdout);

// READING

printf("Reading pressure data... \n");

fflush(stdout);

fp1 = fopen("pxyz.data","r");

//Discard the first 2 lines

for(i=0; i<=10; i++)

    fscanf(fp1,"%s", &string[i]);

printf("string = %s\n", string);

fflush(stdout);

//

// Now read the pressure values

for(i=0; i<=t_max; i++)

    for(j=0; j<4; j++)

        fscanf(fp1,"%f", &press[i][j]);

fclose(fp1);

printf("Finished reading data. \n");

fflush(stdout);

// CALCULATION

// INITIALISE SECTION

init = 0;

for (N=0; N<=p-1; N++)

{

    SUM_xy[N] = 0.0;

    SUM_xz[N] = 0.0;

    SUM_yz[N] = 0.0;

}
```

```
//

for(k=1; k<=k_max; k++)
{
    // INITIALISE
    printf("k = %d \n", k);
    fflush(stdout);
    for(i=0; i<=p; i++)
    {
        c_xy[i] = 0.0;
        c_xz[i] = 0.0;
        c_yz[i] = 0.0;
    }

    // INNER CALCULATION of AUTOCORRELATION
    for (N=0; N<=p-1; N++)
    {
        for (j=init*((k-1)*p-N+1); j<=k*p-N; j++)
        {
            SUM_xy[N] = SUM_xy[N] + press[j*s][1]*press[j*s+N*s][1];
            SUM_xz[N] = SUM_xz[N] + press[j*s][2]*press[j*s+N*s][2];
            SUM_yz[N] = SUM_yz[N] + press[j*s][3]*press[j*s+N*s][3];
        }

        c_xy[N] = (1/( (double)k*p-(N-1) ))*SUM_xy[N];
        c_xz[N] = (1/( (double)k*p-(N-1) ))*SUM_xz[N];
        c_yz[N] = (1/( (double)k*p-(N-1) ))*SUM_yz[N];
    }

    // INTEGRATION
    sum1 = 0.0;
    sum2 = 0.0;
    sum3 = 0.0;
    for (N=1; N<=p-2; N++)
    {
        sum1 = sum1 + c_xy[N];
        sum2 = sum2 + c_xz[N];
        sum3 = sum3 + c_yz[N];
    }
```

```
        visc_xy = (0.5*c_xy[0]+0.5*c_xy[p-1]+sum1)*((double)s)*scale;
        visc_xz = (0.5*c_xz[0]+0.5*c_xz[p-1]+sum2)*((double)s)*scale;
        visc_yz = (0.5*c_yz[0]+0.5*c_yz[p-1]+sum3)*((double)s)*scale;

        printf("v_xy = %f \n", visc_xy);
        printf("v_xz = %f \n", visc_xz);
        printf("v_yx = %f \n", visc_yz);
        fflush(stdout);

        total_visc = (visc_xy + visc_xz + visc_yz)/3;
        printf("Total Viscosity = %.10f \n", total_visc);
        fflush(stdout);

        init=1; // CAUTION!
    }
    //
    return 0;
}

// Viscosity averaging script for NEMD

#include"stdio.h"
#include"stdlib.h"

#define  MAX_LEN  80

int main()
{
    FILE *fp1;
    int i,j,k,N,init; // indices
    int s,p,d,t_max,k_max,starting_val;
    char string[MAX_LEN + 1];

    static float press[5000001][2]; // pressure values i index = t_max + 1 TO VARY

    double scale, sum;
    double visc_xy, visc_xz, visc_yz, total_visc, sum1, sum2, sum3, result;

    starting_val = 0; // starting pressurre value
    t_max = 5000000; // TO VARY
    scale = 1.01325e-7; // atm to mPa
```

```
    printf("starting pressure value = %d t_max = %d scale = %.14lf \n", starting_val,t_max,scale);

    // READING
    printf("Reading pressure data... \n");
    fp1 = fopen("visc.data","r");
    //Discard the first 2 lines
    for(i=0; i<=8; i++)
        fscanf(fp1,"%s", &string[i]);
    printf("string = %s\n", string);
    //

    // Now read the pressure values
    for(i=0; i<=t_max; i++)
        for(j=0; j<2; j++)
            fscanf(fp1,"%f", &press[i][j]);

    fclose(fp1);
    printf("Finished reading data. \n\n");

    // CALCULATION

    printf("Calculating... \n");

    // CALCULATE SUM
    sum = 0.0;

    for (j=starting_val; j<=t_max; j++)
    {
        sum = sum + press[j][1];
    }
    visc_xy = (1/(((double)t_max+1)))*sum*scale; // care u have 5000001 values!
    printf("viscosity (xy) in mPa s = %.10f \n", visc_xy);
    //
    return 0;
}
```

Appendix C

Packmol and moltemplate files, glycerol example

C.1 Packmol files

glycerol.xyz:

```
14
  Glycerol
C1          0.24329       -0.69184       -1.26932
C2         -0.24083        0.02394        0.00000
C3          0.24329       -0.69184        1.26932
O1         -0.25529       -0.03049       -2.39890
H1          0.08452       -0.53307       -3.18431
O2          0.17264        1.36804        0.00000
H2          1.16593        1.37890        0.00000
O3         -0.25529       -0.03049        2.39890
H3          0.08452       -0.53307        3.18431
H4         -0.12954       -1.74076       -1.25906
H5          1.35643       -0.69119       -1.29432
H6         -1.35299        0.00688        0.00000
```

```
H7          1.35643       -0.69119        1.29432
H8         -0.12954       -1.74076        1.25906
```

glycerol.inp:

```
#
# glycerol
#

# All the atoms from different molecules will be separated at least 2.0
# Angstroms at the solution.

tolerance 2.0

# The file type of input and output files is XYZ

filetype xyz

# The name of the output file

output system.xyz

# 800 glycerol molecules will be put in a box
# defined by the minimum coordinates x, y and z = 0. 0. 0. and maximum
# coordinates 65. 65. 65. That is, they will be put in a cube of side
# 65. (the keyword "inside cube 0. 0. 0. 65.") could be used as well.

structure glycerol.xyz
```

```
  number 800
  inside box 0. 0. 0. 65. 65. 65.
end structure
```

C.2 Moltemplate files

glycerol.lt:

```
import "oplsaa.lt"

# The "oplsaa.lt" file contains force-field definitions and masses for the
# atoms in your system.  See oplsaa_lt_generator/README.TXT for details.

# Note:
# Atom type @atom:99 corresponds to "Alcohol CH3OH & RCH2OH CH2 carbon"
# Atom type @atom:100 corresponds to "Alcohol R2CHOH CH carbon"
# Atom type @atom:113 corresponds to "Triol -OH O"
# Atom type @atom:114 corresponds to "Triol -OH H"
# Atom type @atom:118 corresponds to "Diol & Triol H-COH"

Glycerol inherits OPLSAA {

  # We just need a list of atom types and bonds.
  #
  # We don't have to specify the charge in because we are
  # using the OPLSAA force-field, which assigns this by atom-type.
  #
  # We also don't have to specify the coordinates, because
  # we are using PACKMOL to generate them for you.

  write('Data Atoms') {
    $atom:C1  $mol @atom:99  0.00   0.00   0.00  0.00 # "Alcohol CH3OH & RCH2OH CH2 carbon"
    $atom:C2  $mol @atom:100  0.00   0.00   0.00  0.00 # "Alcohol R2CHOH CH carbon"
    $atom:C3  $mol @atom:99  0.00   0.00   0.00  0.00 # "Alcohol CH3OH & RCH2OH CH2 carbon"
    $atom:O1  $mol @atom:113  0.00   0.00   0.00  0.00 # "Triol -OH O"
    $atom:H1  $mol @atom:114  0.00   0.00   0.00  0.00 # "Triol -OH H"
    $atom:O2  $mol @atom:113  0.00   0.00   0.00  0.00 # "Triol -OH O"
```

```
    $atom:H2  $mol @atom:114  0.00   0.00   0.00  0.00 # "Triol -OH H"
    $atom:O3  $mol @atom:113  0.00   0.00   0.00  0.00 # "Triol -OH O"
    $atom:H3  $mol @atom:114  0.00   0.00   0.00  0.00 # "Triol -OH H"
    $atom:H4  $mol @atom:118  0.00   0.00   0.00  0.00 # "Diol & Triol H-COH"
    $atom:H5  $mol @atom:118  0.00   0.00   0.00  0.00 # "Diol & Triol H-COH"
    $atom:H6  $mol @atom:118  0.00   0.00   0.00  0.00 # "Diol & Triol H-COH"
    $atom:H7  $mol @atom:118  0.00   0.00   0.00  0.00 # "Diol & Triol H-COH"
    $atom:H8  $mol @atom:118  0.00   0.00   0.00  0.00 # "Diol & Triol H-COH"
  }

  write('Data Bond List') {
    $bond:C12  $atom:C1 $atom:C2
    $bond:C23  $atom:C2 $atom:C3

    $bond:C1H4 $atom:C1 $atom:H4
    $bond:C1H5 $atom:C1 $atom:H5
    $bond:C1O1 $atom:C1 $atom:O1
    $bond:O1H1 $atom:O1 $atom:H1

    $bond:C2H6 $atom:C2 $atom:H6
    $bond:C2O2 $atom:C2 $atom:O2
    $bond:O2H2 $atom:O2 $atom:H2

    $bond:C3H7 $atom:C3 $atom:H7
    $bond:C3H8 $atom:C3 $atom:H8
    $bond:C3O3 $atom:C3 $atom:O3
    $bond:O3H3 $atom:O3 $atom:H3
  }

} # Glycerol
```

system.lt:

```
import "glycerol.lt"  # <- defines the "Glycerol" molecule type.



# Periodic boundary conditions:
```

```
write_once("Data Boundary") {
   0.0  65.00  xlo xhi
   0.0  65.00  ylo yhi
   0.0  65.00  zlo zhi
}



# Create 800 glycerols
# List them in the same order they appear in the PACKMOL .inp file(s).

glycerols  = new Glycerol[800]
```

Appendix D

LAMMPS input script for density, EMD-GK, NEMD and confined NEMD viscosity calculation

Density at 27 °C *n*-hexadecane:

```
#----initialization Section --------------------

include         system.in.init

# ------------------------------ Atom Definition Section -------------------

read_data       system.data

# ------------------------------ Settings Section --------------------------

include         system.in.settings
include         system.in.charges

# ------------------------------ Run Section -------------------------------

dump dumpeq1 all custom 50 traj_eq1_min.lammpstrj id mol type x y z ix iy iz
thermo          50

# -- Equilibration: part 1: initial relaxation --

minimize 1.0e-5 1.0e-7 100000 400000
```

```
undump          dumpeq1

write_data   system_after_eq1_min.data

# -- Equilibration part 2: Equilibrating the density (NPT) --

dump dumpeq2 all custom 200 traj_eq2_npt.lammpstrj id mol type x y z ix iy iz
fix fxnpt all npt temp 300.0 300.0 100.0 iso 1.0 1.0 1000.0 drag 2.0

thermo  10000

timestep        1.0
thermo_style custom step pe ke etotal temp press density
run             10000000
undump dumpeq2

write_data   system_after_eq2_npt.data

# -- Equilibration part 3: density (NPT) --

dump dumpeq3 all custom 40000 traj_eq3_npt.lammpstrj id mol type x y z ix iy iz

thermo          10000
run             10000000

undump dumpeq3
write_data   system_after_eq3_npt.data

# -- Equilibration final part: reorienting the molecules (NVT) --
unfix fxnpt

dump dumpeq4 all custom 2000 traj_eq4_reorient.lammpstrj id mol type x y z ix iy iz

fix fxnvt all nvt temp 300.0 300.0 100.0

run             2000000
undump dumpeq4
```

```
write_data   system_after_eq4_reorient.data

unfix fxnvt
```

Zero shear Viscosity EMD-GK at 27 °C *n*-hexadecane:

```
# ------------------------------ Initialization Section --------------------

include         system.in.init

# ------------------------------ Atom Definition Section -------------------

read_data       system_after_eq4_reorient.data

# ------------------------------ Settings Section --------------------------

include         system.in.settings
include         system.in.charges

# variables

variable    T equal 300
variable    V equal vol
variable    dt equal 1.0

variable    p equal 100000     # correlation length
variable    s equal 5       # sample interval
variable    d equal $p*$s   # dump interval

variable    kB equal 1.3806504e-23    # [J/K/** Boltzmann
variable    atm2Pa equal 101325.0
variable    A2m equal 1.0e-10
variable    fs2s equal 1.0e-15
variable    convert equal ${atm2Pa}*${atm2Pa}*${fs2s}*${A2m}*${A2m}*${A2m}

timestep     ${dt}
thermo       $d

velocity     all create $T 102486 mom yes rot yes dist gaussian
```

```
fix          NVT all nvt temp $T $T 10 drag 0.2

run          1000000

reset_timestep 0
variable     pxy equal pxy
variable     pxz equal pxz
variable     pyz equal pyz
fix          SS all ave/correlate $s $p $d &
             v_pxy v_pxz v_pyz type auto file S0St.dat ave running
variable     scale equal ${convert}/(${kB}*$T)*$V*$s*${dt}
variable     v11 equal trap(f_SS[3])*${scale}
variable     v22 equal trap(f_SS[4])*${scale}
variable     v33 equal trap(f_SS[5])*${scale}
thermo_style custom step temp press v_pxy v_pxz v_pyz v_v11 v_v22 v_v33


run          40000000


variable     v equal (v_v11+v_v22+v_v33)/3.0
variable     ndens equal count(all)/vol
print        "average viscosity: $v [Pa.s] @ $T K, ${ndens} /A^3"
```

NEMD Viscosity at 27 °C *n*-hexadecane, $log\dot{\gamma} = 9.00$:

```
# sample LAMMPS input script for viscosity of hexa 300K 1atm v1.0 3d
# NEMD via fix deform and fix nvt/sllod

# ------------------------------ Initialization Section --------------------

include         system.in.init

# ------------------------------ Atom Definition Section -------------------

read_data       system_after_eq4_reorient.data
```

```
# ------------------------------ Settings Section --------------------------

include         system.in.settings
include         system.in.charges

# variables

variable    T equal 300
variable    V equal vol
variable    dt equal 1.0
variable    srate equal 0.0000400 # velocity of top edge, might need to be changed

# conversion variables 29 JAN 2019

variable    fs2sminus1 equal 1.0e15 # shear rate in s-1
variable    atmfs2mPas equal 1.01325e-7 # atm + fs to mPa s

# problem setup

change_box all triclinic
kspace_style    pppm 0.0001
velocity        all create $T 97287
thermo          1000
timestep        $dt

# turn on NEMD shear and equilibrate some more

#velocity all scale $T

# shear rate defined relative to perpendicular dimension

variable xyrate equal $srate/ly
variable xyratecorrect equal $xyrate*$fs2sminus1 # 29 JAN addition

fix 1 all nvt/sllod temp $T $T 10
fix 2 all deform 1 xy erate $xyrate remap v
```

```
compute         layers all chunk/atom bin/1d y center 0.05 units reduced
fix 4 all ave/chunk 20 250 5000 layers vx file profile.nemd.3d

compute usual all temp
compute tilt all temp/deform

thermo_style custom step temp c_usual epair etotal press pxy v_xyrate v_srate ly
thermo_modify temp tilt
run 20000000

# data gathering run

variable visc equal -pxy/(v_srate/ly)

fix          TiMe all ave/time 1 1 1 &
             v_visc file visc.data ave one mode scalar

fix vave all ave/time 10 100 1000 v_visc ave running start 20001000

variable vavecorrect equal f_vave*$atmfs2mPas # 29 JAN addition
variable visccorrect equal -pxy/(v_srate/ly)*$atmfs2mPas # 29 JAN addition

thermo_style custom step temp press pxy v_visc f_vave v_xyrate v_srate ly v_visccorrect
v_vavecorrect v_xyratecorrect
thermo_modify temp tilt

run 40000000
```

system.in.init:

```
units real
atom_style full
bond_style hybrid harmonic
angle_style hybrid harmonic
dihedral_style hybrid opls
improper_style hybrid harmonic
pair_style hybrid lj/cut/coul/long 13.0
```

```
pair_modify mix geometric tail yes
kspace_style pppm 0.0001
neigh_modify delay 0 page 300000 one 20000
special_bonds lj/coul 0.0 0.0 0.5
```

system.in.settings: Force field parameters

system.in.charges: Atomic charges

system.data: LAMMPS atomic coordinates

Confined NEMD Viscosity at 100 °C 9,10-dimethyloctadecane, $log\dot{\gamma} = 8.50$:

```
boundary p p f
#-------------- Initialization Section --------------------
include       lopls.in.CreateBonds2
include       lopls.in.init
include       lopls.in.settings
include       lopls.in.charges


kspace_style    pppm 0.0001
kspace_modify slab 3.0
neigh_modify delay 0 page 300000 one 20000
dump           dump1 all atom 500 lopls.dump
thermo_style   custom step lx ly lz  density temp press etotal

thermo        1000
timestep      0.001

include         group.lower # 2 nov 21 extension
include         group.upper

group        boundary union lower upper
group        flow subtract all boundary

#OK
group high-force id 12957    12987    13017    13047    13077   ...
```

```
#OK
group  z-stationary id 6209    6239    6269    6299    6329    ...

############## 9 - OCTOBER 21 film thickness addition

group   up-low id 12959    12989    13019    13049    13079    ...

group   bottom-hi id 6207    6237    6267    6297    6327    ...

###############

############## 20 dec 21 - thermostating confined wall upper (9.8 Angstrem)

group therm-wall subtract upper high-force up-low

###############

fix freeze high-force setforce 0.0 NULL NULL
fix 5 z-stationary setforce 0.0 0.0 0.0

velocity z-stationary set 0.0 0.0 0.0 sum no units box
velocity high-force   set 0.0 0.0 0.0 sum no units box

undump       dump1

fix 40 all nve
fix 2 therm-wall langevin 373.15 373.15 0.1 498094 # 20 dec 21 addition to thermostat
the upper wall and not the fluid as in literature

compute zaveup up-low reduce ave z

compute zavelow bottom-hi reduce ave z

variable filmthick equal c_zaveup-c_zavelow
variable avefilm equal 13.80280448475760000 # 19 dec 21 addition from
post-processing after compression

compute ftemp flow temp
compute fwall therm-wall temp
```

```
# 24,27 dec 21 press compute fluid
compute        peratom flow stress/atom NULL
compute        m all reduce sum c_peratom[1] c_peratom[2] c_peratom[3] c_peratom[5]
variable       pressm equal -(c_m[1]+c_m[2]+c_m[3])/(3*lx*ly*$avefilm)

variable       stressxz equal c_m[4]/(lx*ly*$avefilm)

compute 100 high-force reduce sum fz
variable    for   equal -0.013551487 #3.0490846 * 23.06 = 0.1 GPa ext. pressure

thermo_style   custom step lx ly lz  density temp c_ftemp c_fwall press v_pressm
etotal c_100 v_for c_zaveup c_zavelow v_filmthick

fix kick high-force aveforce NULL NULL v_for

############


# Couette flow

variable   gammadot equal 316227766.0168380
variable   loggama  equal log(v_gammadot)

variable    srate equal $gammadot*$avefilm*1.0e-12 # 19 nov 21 sos units metal u = a/ps
velocity     high-force set $srate NULL NULL sum no units box

compute      thermal flow temp/partial 0 0 1


thermo_modify   temp fwall

compute         tilt flow temp/ramp vx 0 $srate z 0 142.46 units box

thermo          1000
#thermo_style    custom step temp c_tilt epair etotal press pxy pxz
thermo_style    custom step temp c_ftemp c_tilt c_fwall press v_pressm v_stressxz pxz
```

```
density lz v_filmthick v_srate v_loggama v_avefilm
dump            1 all custom 20000 dump.conf-nemd2.3d id type x y z vx


# data gathering run

compute         layers all chunk/atom bin/1d z center 0.00625 units reduced compress yes
fix 400 all ave/chunk 20 250 5000 layers vx ave one file vel_profile.wall2.3d

compute         layers2 flow chunk/atom bin/1d z center 0.000625 units reduced compress
yes
fix           198 flow ave/chunk 20 250 5000 layers2 density/mass ave one file
dens_profile.wall2.3d

variable        visc2 equal (c_m[4]/(lx*ly*$avefilm))/(v_srate/$avefilm) #27 dec new
definition

fix          TiMe2 all ave/time 1 1 1 &
              v_visc2 file visc2.data2 ave one mode scalar

fix             vave2 all ave/time 10 100 1000 v_visc2 ave running start 1000


thermo_style    custom step temp c_ftemp c_tilt c_fwall press v_pressm v_stressxz pxz
density lz  v_filmthick v_srate v_loggama v_visc2 f_vave2

restart      100000 checkpoint

run             4000000


write_data   system_after_shear3.data
```

lopls.in.init:

```
bond_style      hybrid harmonic
angle_style     hybrid harmonic
```

```
dihedral_style  hybrid opls multi/harmonic
improper_style  hybrid harmonic

pair_style hybrid lj/cut/coul/long 13.0
pair_modify mix geometric
kspace_style pppm 0.0001
neigh_modify delay 0 page 300000 one 20000
special_bonds lj/coul 0.0 0.0 0.5
```

lopls.in.settings: Force field parameters

lopls.in.charges: Atomic charges

lopls.in.CreateBonds2:

```
#dummy start needed to create bonds in lammps
units          metal
boundary p p f
atom_style    full
read_data     system_after_shear2.data extra/bond/types 6
pair_style     lj/cut 10.0
pair_coeff     * * 1.0 1.0
bond_style harmonic
bond_coeff     * 1.0 1.0

# Creating groups
group          fe               type      30
group          ox               type      31

#Ceating bonds
create_bonds many fe ox 250 1.900 2.000
create_bonds many fe ox 251 2.000 2.500
create_bonds many ox ox 252 2.800 2.900
create_bonds many ox ox 253 2.700 2.799
create_bonds many ox ox 254 2.600 2.699
create_bonds many fe fe 255 2.900 3.000
```

References

[1] S. T. Cui, P. T. Cummings, and H. D. Cochran. The calculation of viscosity of liquid n-decane and n-hexadecane by the Green-Kubo method. *Mol. Phys.*, 93(1):117–122, 1998.

[2] J. P. Ewen, C. Gattinoni, F. M. Thakkar, N. Morgan, H. A. Spikes, and D. Dini. A Comparison of Classical Force-Fields for Molecular Dynamics Simulations of Lubricants. *Materials*, 9(8):651, 2016.

[3] J. P. Ewen, D. M. Heyes, and D. Dini. Advances in nonequilibrium molecular dynamics simulations of lubricants and additives. *Friction*, 6(4):349–386, 2018.

[4] M. S. Green. Markoff Random Processes and the Statistical Mechanics of Time-Dependent Phenomena. II. Irreversible Processes in Fluids. *J. Chem. Phys.*, 22(3):398–413, 1954.

[5] R. Kubo. Statistical-Mechanical Theory of Irreversible Processes. I. General Theory and Simple Applications to Magnetic and Conduction Problems. *J. Phys. Soc. Jpn.*, 12(6):570–586, 1957.

[6] R. S. Payal, S. Balasubramanian, I. Rudra, K. Tandon, I. Mahlke, D. Doyle, and R. Cracknell. Shear viscosity of linear alkanes through molecular simulations: quantitative tests for n-decane and n-hexadecane. *Mol. Simulat.*, 38(14-15):1234–1241, 2012.

[7] E. M. Kirova and G. E. Norman. Viscosity calculations at molecular dynamics simulations. *J. Phys. Conf. Ser.*, 653:012106, 2015.

[8] W. G. Hoover, D. J. Evans, R. B. Hickman, A. J. C. Ladd, W. T. Ashurst, and B. Moran. Lennard-Jones triple-point bulk and shear viscosities. Green-Kubo theory, Hamiltonian mechanics, and nonequilibrium molecular dynamics. *Phys. Rev. A*, 22(4):1690–1697, 1980.

[9] J.-P. Ryckaert, A. Bellemans, G. Ciccotti, and G. V. Paolini. Evaluation of transport coefficients of simple fluids by molecular dynamics: Comparison of Green-Kubo

and nonequilibrium approaches for shear viscosity. *Phys. Rev. A*, 39(1):259–267, 1989.

[10] U. S. Ramasamy, M. Len, and A. Martini. Correlating Molecular Structure to the Behavior of Linear Styrene-Butadiene Viscosity Modifiers. *Tribol. Lett.*, 65(4):147, 2017.

[11] R. E. Jones and K. K. Mandadapu. Adaptive Green-Kubo estimates of transport coefficients from molecular dynamics based on robust error analysis. *J. Chem. Phys.*, 136(15):154102, 2012.

[12] Y. Zhang, A. Otani, and E. J. Maginn. Reliable Viscosity Calculation from Equilibrium Molecular Dynamics Simulations: A Time Decomposition Method. *J. Chem. Theory Comput.*, 11(8):3537–3546, 2015.

[13] Y. Feng, J. Goree, B. Liu, and E. G. D. Cohen. Green-Kubo relation for viscosity tested using experimental data for a two-dimensional dusty plasma. *Phys. Rev. E*, 84(4):046412, 2011.

[14] C. Wesp, A. El, F. Reining, Z. Xu, I. Bouras, and C. Greiner. Calculation of shear viscosity using Green-Kubo relations within a parton cascade. *Phys. Rev. C*, 84(5):054911, 2011.

[15] H. Matsuoka. Green-Kubo Formulas with Symmetrized Correlation Functions for Quantum Systems in Steady States: The Shear Viscosity of a Fluid in a Steady Shear Flow. *J. Stat. Phys.*, 148(5):933–950, 2012.

[16] J. D. Moore, S. T. Cui, H. D. Cochran, and P. T. Cummings. Rheology of lubricant basestocks: A molecular dynamics study of C_{30} isomers. *J. Chem. Phys.*, 113(19):8833–8840, 2000.

[17] N.-T. Van-Oanh, C. Houriez, and B. Rousseau. Viscosity of the 1-ethyl-3-methylimidazolium bis(trifluoromethylsulfonyl)imide ionic liquid from equilibrium and nonequilibrium molecular dynamics. *Phys. Chem. Chem. Phys.*, 12(4):930–936, 2010.

[18] M. Mouas, J.-G. Gasser, S. Hellal, B. Grosdidier, A. Makradi, and S. Belouettar. Diffusion and viscosity of liquid tin: Green-Kubo relationship-based calculations from molecular dynamics simulations. *J. Chem. Phys.*, 136(9):094501, 2012.

[19] E. M. Kirova and V. V. Pisarev. Study of viscosity of aluminum melt during glass transition by molecular dynamics and Green-Kubo formula. *J. Phys. Conf. Ser.*, 774:012032, 2016.

[20] N. D. Kondratyuk, V. V. Pisarev, and J. P. Ewen. Probing the high-pressure viscosity of hydrocarbon mixtures using molecular dynamics simulations. *J. Chem. Phys.*, 153(15):154502, 2020.

[21] P. Liu, J. Lu, H. Yu, N. Ren, F. E. Lockwood, and Q. J. Wang. Lubricant shear thinning behavior correlated with variation of radius of gyration via molecular dynamics simulations. *J. Chem. Phys.*, 147(8):084904, 2017.

[22] J. P. Ewen, H. Gao, M. H. Müser, and D. Dini. Shear heating, flow, and friction of confined molecular fluids at high pressure. *Phys. Chem. Chem. Phys.*, 21:5813–5823, 2019.

[23] I. J. Prentice, X. Liu, O. A. Nerushev, S. Balakrishnan, C. R. Pulham, and P. J. Camp. Experimental and simulation study of the high-pressure behavior of squalane and poly-α-olefins. *J. Chem. Phys.*, 152(7):074504, 2020.

[24] J. D. Moore, S. T. Cui, P. T. Cummings, and H. D. Cochran. Lubricant characterization by molecular simulation. *AIChE J.*, 43(12):3260–3263, 1997.

[25] Y. Yang, T. A. Pakkanen, and R. L. Rowley. NEMD Simulations of Viscosity and Viscosity Index for Lubricant-Size Model Molecules. *Inter. J. Thermophys.*, 23(6):1441–1454, 2002.

[26] P. Liu, H. Yu, N. Ren, F. E. Lockwood, and Q. J. Wang. Pressure-Viscosity Coefficient of Hydrocarbon Base Oil through Molecular Dynamics Simulations. *Tribol. Lett.*, 60(3):34, 2015.

[27] M. A. Galvani Cunha and M. O. Robbins. Determination of pressure-viscosity relation of 2,2,4-trimethylhexane by all-atom molecular dynamics simulations. *Fluid Phase Equilib.*, 495:28–32, 2019.

[28] V. Jadhao and M. O. Robbins. Probing large viscosities in glass-formers with nonequilibrium simulations. *Proc. Natl. Acad. Sci.*, 114(30):7952–7957, 2017.

[29] V. Jadhao and M. O. Robbins. Rheological Properties of Liquids Under Conditions of Elastohydrodynamic Lubrication. *Tribol. Lett.*, 67(3):66, 2019.

[30] U. S. Ramasamy, S. Bair, and A. Martini. Predicting Pressure-Viscosity Behavior from Ambient Viscosity and Compressibility: Challenges and Opportunities. *Tribol. Lett.*, 57(2):11, 2015.

[31] J. P. Ewen, C. Gattinoni, N. Morgan, H. A. Spikes, and D. Dini. Nonequilibrium Molecular Dynamics Simulations of Organic Friction Modifiers Adsorbed on Iron Oxide Surfaces. *Langmuir*, 32(18):4450–4463, 2016.

[32] R. L. Shubkin. *Alpha Olefin Application Handbook*. 353-373, ed. G. R. Lappin and J. D. Sauer, Marcel Dekker, New York, 1989.

[33] L. R. Rudnick and R. L. Shubkin. *Synthetic Lubricants and High-Performance Functional Fluids*. 3-52, Marcel Dekker, New York, 1999.

[34] R. Benda, J. Bullen, and A. Plomer. Synthetics basics: Polyalphaolefins - base fluids for high-performance lubricants. *J. Synth. Lubr.*, 13(1):41–57, 1996.

[35] S. S. Scheuermann, S. Eibl, and P. Bartl. Detailed characterisation of isomers present in polyalphaolefin dimer and the effect of isomeric distribution on bulk properties. *Lubr. Sci.*, 23(5):221–232, 2011.

[36] *Spectrasyn 2 MSDS No. 322817*. ExxonMobil, TX, 7 July 2020.

[37] C. P. Chui, W. Liu, Y. Xu, and Y. Zhou. Molecular Dynamics Simulation of Iron - A Review. *Spin*, 5(4):1540007, 2015.

[38] W. L. Jorgensen, D. S. Maxwell, and J. Tirado-Rives. Development and Testing of the OPLS All-Atom Force Field on Conformational Energetics and Properties of Organic Liquids. *J. Am. Chem. Soc.*, 118(45):11225–11236, 1996.

[39] S. W. I. Siu, K. Pluhackova, and R. A. Böckmann. Optimization of the OPLS-AA Force Field for Long Hydrocarbons. *J. Chem. Theory Comput.*, 8(4):1459–1470, 2012.

[40] GAFF and GAFF2 are public domain force fields and are part of the AmberTools16 distribution, available for download at http://ambermd.org internet address (accessed September 2020). According to the AMBER development team, the improved version of GAFF, GAFF2 is an ongoing project aimed at "reproducing both the high quality interaction energies and key liquid properties such as density, heat of vaporization and hydration free energy." GAFF2 is expected "to be an even more successful general purpose force field and that GAFF2-based scoring functions will significantly improve the successful rate of virtual screenings".

[41] D. Vassetti, M. Pagliai, and P. Procacci. Assessment of GAFF2 and OPLS-AA General Force Fields in Combination with the Water Models TIP3P, SPCE, and OPC3 for the Solvation Free Energy of Druglike Organic Molecules. *J. Chem. Theory Comput.*, 15(3):1983–1995, 2019.

[42] T. P. Senftle, S. Hong, M. M. Islam, S. B. Kylasa, Y. Zheng, Y. K. Shin, C. Junkermeier, R. Engel-Herbert, M. J. Janik, H. M. Aktulga, T. Verstraelen, A. Grama, and A. C. T. van Duin. The ReaxFF reactive force-field: development, applications and future directions. *npj Comput. Mater.*, 2(1):15011, 2016.

[43] H. M. Aktulga, J. C. Fogarty, S. A. Pandit, and A. Y. Grama. Parallel reactive molecular dynamics: Numerical methods and algorithmic techniques. *Parallel Comput.*, 38(4):245–259, 2012.

[44] A. K. Rappe and W. A. Goddard. Charge equilibration for molecular dynamics simulations. *J. Phys. Chem.*, 95(8):3358–3363, 1991.

[45] A. Nakano. Parallel multilevel preconditioned conjugate-gradient approach to variable-charge molecular dynamics. *Comput. Phys. Commun.*, 104(1):59–69, 1997.

[46] H. C. Andersen. Molecular dynamics simulations at constant pressure and/or temperature. *J. Chem. Phys.*, 72(4):2384–2393, 1980.

[47] H. J. C. Berendsen, J. P. M. Postma, W. F. van Gunsteren, A. DiNola, and J. R. Haak. Molecular dynamics with coupling to an external bath. *J. Chem. Phys.*, 81(8):3684–3690, 1984.

[48] T. Schneider and E. Stoll. Molecular-dynamics study of a three-dimensional one-component model for distortive phase transitions. *Phys. Rev. B*, 17(3):1302–1322, 1978.

[49] G. Bussi, D. Donadio, and M. Parrinello. Canonical sampling through velocity rescaling. *J. Chem. Phys.*, 126(1):014101, 2007.

[50] P. H. Hünenberger. *Thermostat Algorithms for Molecular Dynamics Simulations*. 105-149, Springer, Berlin, Heidelberg, 2005.

[51] E. Braun, J. Gilmer, H. B. Mayes, D. L. Mobley, J. I. Monroe, S. Prasad, and D. M. Zuckerman. Best Practices for Foundations in Molecular Simulations. *Liv. J. Comput. Mol. Sci.*, 1(1):5957, 2018.

[52] T. Morishita. Fluctuation formulas in molecular-dynamics simulations with the weak coupling heat bath. *J. Chem. Phys.*, 113(8):2976–2982, 2000.

[53] J. E. Basconi and M. R. Shirts. Effects of Temperature Control Algorithms on Transport Properties and Kinetics in Molecular Dynamics Simulations. *J. Chem. Theory Comput.*, 9(7):2887–2899, 2013.

[54] G. J. Martyna, M. L. Klein, and M. Tuckerman. Nosé–Hoover chains: The canonical ensemble via continuous dynamics. *J. Chem. Phys.*, 97(4):2635–2643, 1992.

[55] M. Parrinello and A. Rahman. Polymorphic transitions in single crystals: A new molecular dynamics method. *J. Appl. Phys.*, 52(12):7182–7190, 1981.

[56] G. J. Martyna, D. J. Tobias, and M. L. Klein. Constant pressure molecular dynamics algorithms. *J. Chem. Phys.*, 101(5):4177–4189, 1994.

[57] G. J. Martyna, M. E. Tuckerman, D. J. Tobias, and M. L. Klein. Explicit reversible integrators for extended systems dynamics. *Mol. Phys.*, 87(5):1117–1157, 1996.

[58] X. Shen, H. Du, R. H. Mullins, and R. R. Kommalapati. Polyethylenimine Applications in Carbon Dioxide Capture and Separation: From Theoretical Study to Experimental Work. *Energy Technol.*, 5(6):822–833, 2017.

[59] `https://www.investopedia.com/terms/a/autocorrelation.asp`. (accessed 23/May/2022).

[60] `https://nanohub.org/resources/31249/watch?resid=31624`. (accessed 23/May/2022).

[61] H. B. Callen and T. A. Welton. Irreversibility and Generalized Noise. *Phys. Rev.*, 83(1):34–40, 1951.

[62] E. J. Maginn, R. A. Messerly, D. J. Carlson, D. R. Roe, and J. R. Elliott. Best Practices for Computing Transport Properties 1. Self-Diffusivity and Viscosity from Equilibrium Molecular Dynamics. *Liv. J. Comput. Mol. Sci.*, 1(1):6324, 2018.

[63] D. Frenkel and B. Smit. *Understanding Molecular Simulation*. Academic Press, San Diego, 2002.

[64] B. D. Todd and P. J. Daivis. *Nonequilibrium Molecular Dynamics: Theory, Algorithms and Applications*. Cambridge University Press, Cambridge, 2017.

[65] D. J. Evans and G. P. Morriss. Nonlinear-response theory for steady planar Couette flow. *Phys. Rev. A*, 30:1528–1530, 1984.

[66] A. W. Lees and S. F. Edwards. The computer study of transport processes under extreme conditions. *J. Phys. C: Solid State Phys.*, 5(15):1921–1928, 1972.

[67] B. D. Todd and P. J. Daivis. The stability of nonequilibrium molecular dynamics simulations of elongational flows. *J. Chem. Phys.*, 112(1):40–46, 2000.

[68] C. Baig, B. J. Edwards, D. J. Keffer, and H. D. Cochran. A proper approach for nonequilibrium molecular dynamics simulations of planar elongational flow. *J. Chem. Phys.*, 122(11):114103, 2005.

[69] S. Jeong, J. M. Kim, S. Cho, and C. Baig. Effect of short-chain branching on interfacial polymer structure and dynamics under shear flow. *Soft Matter*, 13:8644–8650, 2017.

[70] A. A. Samoletov, C. P. Dettmann, and M. A. J. Chaplain. Thermostats for "Slow" Configurational Modes. *J. Stat. Phys.*, 128(6):1321–1336, 2007.

[71] P. Xu, T. Cagin, and W. A. Goddard. Assessment of phenomenological models for viscosity of liquids based on nonequilibrium atomistic simulations of copper. *J. Chem. Phys.*, 123(10):104506, 2005.

[72] R. E. Powell and H. Eyring. Mechanisms for the Relaxation Theory of Viscosity. *Nature*, 154(3909):427–428, 1944.

[73] B. S. Massey and J. Ward-Smith. *Mechanics of Fluids*. CRC Press, 9th edition, 2012.

[74] J. H. Irving and J. G. Kirkwood. The Statistical Mechanical Theory of Transport Processes. IV. The Equations of Hydrodynamics. *J. Chem. Phys.*, 18(6):817–829, 1950.

[75] B. D. Todd, D. J. Evans, and P. J. Daivis. Pressure tensor for inhomogeneous fluids. *Phys. Rev. E*, 52:1627–1638, 1995.

[76] `https://docs.lammps.org/compute_stress_mop.html`. (accessed 26/5/2022).

[77] A. Martini, Y. Liu, R. Q. Snurr, and Q. J. Wang. Molecular dynamics characterization of thin film viscosity for EHL simulation. *Tribol. Lett.*, 21(3):217–225, 2006.

[78] `https://docs.lammps.org/compute_stress_atom.html`. (accessed 26/5/2022).

[79] S. Plimpton. Fast Parallel Algorithms for Short-Range Molecular Dynamics. *J. Comput. Phys.*, 117(1):1–19, 1995.

[80] A. I. Jewett, Z. Zhuang, and J.-E. Shea. Moltemplate a Coarse-Grained Model Assembly Tool. *Biophys. J.*, 104(2):169a, 2013.

[81] L. Martinez, R. Andrade, E. G. Birgin, and J. M. Martinez. PACKMOL: A package for building initial configurations for molecular dynamics simulations. *J. Comput. Chem.*, 30(13):2157–2164, 2009.

[82] `https://molview.org`. (accessed 22/9/2020).

[83] H. Sun. COMPASS: An ab Initio Force-Field Optimized for Condensed-Phase Applications - Overview with Details on Alkane and Benzene Compounds. *J. Phys. Chem. B*, 102(38):7338–7364, 1998.

[84] R. W. Hockney and J. W. Eastmond. *Computer Simulation Using Particles*. CRC Press, Bristol, PA, USA, 1988.

[85] S. Nosé. A molecular dynamics method for simulations in the canonical ensemble. *Mol. Phys.*, 52(2):255–268, 1984.

[86] W. G. Hoover. Canonical dynamics: Equilibrium phase-space distributions. *Phys. Rev. A*, 31(3):1695–1697, 1985.

[87] C. Barus. Isothermals, isopiestics and isometrics relative to viscosity. *Am. J. Sci.*, 45(266):87–96, 1893.

[88] S. Bair. *Encyclopedia of Tribology: High Pressure Viscometers*, pages 1663–1670. Springer US, Boston, 2013.

[89] S. S. Karunarathne, D. A. Eimer, and L. E. Øi. Evaluation of Systematic Error and Uncertainty of Viscosity Measurements of Mixtures of Monoethanol Amine and Water in Coaxial Cylinder Rheometers. *Int. J. Model. Optim*, 8(5):260–265, 2018.

[90] S. Bair. *High Pressure Rheology for Quantitative Elastohydrodynamics*. Elsevier, Amsterdam, 2nd edition, 2019.

[91] J. H. Dymond and R. Malhotra. The Tait equation: 100 years on. *Int. J. Thermophys.*, 9(6):941–951, 1988.

[92] Y. Nakamura, S. Hiraiwa, F. Suzuki, and M. Matsui. High-Pressure Viscosity Measurements of Polyalphaolefins at Elevated Temperature. *Tribol. Onl.*, 11(2):444–449, 2016.

[93] `http://www.aciscience.org/docs/physical_properties_of_glycerine_and_its_solutions.pdf`. (accessed 15/11/2018).

[94] https://www.news-medical.net/whitepaper/20160429/Evaluation-of-Mixing-Performance-of-Vitl-Co-Mix-Laboratory-Mixer-with-High-Viscosity-Solutions.aspx. (accessed 15/11/2018).

[95] G. Stachowiak and A. Batchelor. *Engineering Tribology*. Elsevier, 3rd edition, 2011.

[96] K. Yasuda, R. C. Armstrong, and R. E. Cohen. Shear flow properties of concentrated solutions of linear and star branched polystyrenes. *Rheol. Acta.*, 20(2):163–178, 1981.

[97] A. Jakalian, B. L. Bush, D. B. Jack, and C. I. Bayly. Fast, efficient generation of high-quality atomic charges. AM1-BCC model: I. Method. *J. Comput. Chem.*, 21(2):132–146, 2000.

[98] H. Spikes and J. Zhang. History, Origins and Prediction of Elastohydrodynamic Friction. *Tribol. Lett.*, 56(1):1–25, 2014.

[99] R. Taylor and B. R. de Kraker. Shear rates in engines and implications for lubricant design. *Proc. Inst. of Mech. Eng. Part J J. Eng. Tribol.*, 231(9):1106–1116, 2017.

[100] S. Bair, C. McCabe, and P. T. Cummings. Comparison of Nonequilibrium Molecular Dynamics with Experimental Measurements in the Nonlinear Shear-Thinning Regime. *Phys. Rev. Lett.*, 88(5):058302, 2002.

[101] N. Voeltzel, P. Vergne, N. Fillot, N. Bouscharain, and L. Joly. Rheology of an Ionic Liquid with Variable Carreau exponent: A Full Picture by Molecular Simulation with Experimental Contribution. *Tribol. Lett.*, 64(2):25, 2016.

[102] S. Bair. Pressure–viscosity response in the inlet zone for quantitative elastohydrodynamics. *Tribol. Int.*, 97:272–277, 2016.

[103] L. I. Kioupis and E. J. Maginn. Impact of Molecular Architecture on the High-Pressure Rheology of Hydrocarbon Fluids. *J. Phys. Chem. B*, 104(32):7774–7783, 2000.

[104] N. D. Kondratyuk and V. V. Pisarev. Calculation of viscosities of branched alkanes from 0.1 to 1000 MPa by molecular dynamics methods using COMPASS force field. *Fluid Phase Equilib*, 498:151–159, 2019.

[105] E. McEwen. The Effect of Variation of Viscosity with Pressure on the Load-Carrying Capacity of the Oil Film between Gear-Teeth. *J. Inst. Pet.*, 38:646–672, 1952.

[106] M. J. P. Comuñas, A. Baylaucq, C. Boned, and J. Fernández. High-pressure measurements of the viscosity and density of two polyethers and two dialkyl carbonates. *Int. J. Thermophys.*, 22(3):749–768, 2001.

[107] L. Machala, J. Tuček, and R. Zbořil. Polymorphous Transformations of Nanometric Iron(III) Oxide: A Review. *Chem. Mater.*, 23(14):3255–3272, 2011.

[108] T. Amrillah, C. A. C. Abdullah, D. P. Sari, Z. Mumtazah, F. P. Adila, and F. Astuti. Crafting a Next-Generation Device Using Iron Oxide Thin Film: A Review. *Cryst. Growth Des.*, 21(12):7326–7352, 2021.

[109] H. Guo and A. S. Barnard. Thermodynamic modelling of nanomorphologies of hematite and goethite. *J. Mater. Chem.*, 21:11566–11577, 2011.

[110] J. Ewen and S. E. Restrepo. LAMMPS_builder, [Online]. Available: 10.5281/zenodo.1043867, 2017.

[111] J. P. Ewen, S. E. Restrepo, N. Morgan, and D. Dini. Nonequilibrium molecular dynamics simulations of stearic acid adsorbed on iron surfaces with nanoscale roughness. *Tribol. Int.*, 107:264–273, 2017.

[112] K. Momma and F. Izumi. *VESTA 3* for three-dimensional visualization of crystal, volumetric and morphology data. *J. Appl. Crystallogr.*, 44(6):1272–1276, 2011.

[113] D. Savio, N. Fillot, P. Vergne, and M. Zaccheddu. A Model for Wall Slip Prediction of Confined n-Alkanes: Effect of Wall-Fluid Interaction Versus Fluid Resistance. *Tribol. Lett.*, 46(1):11–22, 2012.

[114] H. Berro, N. Fillot, and P. Vergne. Molecular dynamics simulation of surface energy and ZDDP effects on friction in nano-scale lubricated contacts. *Tribol. Int.*, 43(10):1811–1822, 2010.

[115] M. Aryanpour, A. C. T. van Duin, and J. D. Kubicki. Development of a Reactive Force Field for Iron-Oxyhydroxide Systems. *J. Phys. Chem. A*, 114(21):6298–6307, 2010.

[116] C. Zou, A. C. T. van Duin, and D. C. Sorescu. Theoretical Investigation of Hydrogen Adsorption and Dissociation on Iron and Iron Carbide Surfaces Using the ReaxFF Reactive Force Field Method. *Top. Catal.*, 55(5):391–401, 2012.

[117] J. P. Ewen, C. A. Latorre, C. Gattinoni, A. Khajeh, J. D. Moore, J. E. Remias, A. Martini, and D. Dini. Substituent Effects on the Thermal Decomposition of Phosphate Esters on Ferrous Surfaces. *J. Phys. Chem. C*, 124(18):9852–9865, 2020.

[118] J. P. Ewen, C. Gattinoni, J. Zhang, D. M. Heyes, H. A. Spikes, and D. Dini. On the effect of confined fluid molecular structure on nonequilibrium phase behaviour and friction. *Phys. Chem. Chem. Phys.*, 19:17883–17894, 2017.

[119] S. Bernardi, B. D. Todd, and D. J. Searles. Thermostating highly confined fluids. *J. Chem. Phys.*, 132(24):244706, 2010.

[120] B. D. Jensen, K. E. Wise, and G. M. Odegard. The effect of time step, thermostat, and strain rate on ReaxFF simulations of mechanical failure in diamond, graphene, and carbon nanotube. *J. Comput. Chem.*, 36(21):1587–1596, 2015.

[121] S. Grimme. Exploration of Chemical Compound, Conformer, and Reaction Space with Meta-Dynamics Simulations Based on Tight-Binding Quantum Chemical Calculations. *J. Chem. Theory Comput.*, 15(5):2847–2862, 2019.

[122] `https://en.wikipedia.org/wiki/Message_Passing_Interface`. (accessed 22/4/2018).